NTNU
Norwegian University of
Science and Technology

Master's thesis

2022

Ma, Yu

Master's thesis

NTNU
Norwegian University of
Science and Technology
Faculty of Engineering
Department of Marine Technology

Ma, Yu

Novel Modeling and Fatigue Analysis for Early-phase Design of a 15-MW FOWT

June 2022

NTNU
Norwegian University of
Science and Technology

NTNU
Norwegian University of
Science and Technology

Novel Modeling and Fatigue Analysis for Early-phase Design of a 15-MW FOWT

Ma, Yu

Marine Technology
Submission date: June 2022
Supervisor: Gao, Zhen
Co-supervisor: Bachynski, Erin

Norwegian University of Science and Technology
Department of Marine Technology

Kunnskap for en bedre verden

DEPARTMENT OF MARINE TECHNOLOGY

MASTER'S THESIS

Novel Modeling and Fatigue Analysis for Early-phase Design of a 15-MW FOWT

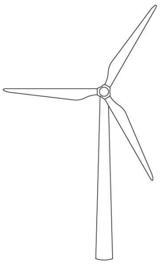

Author:
Ma, Yu

Supervisor:
Gao, Zhen

Co-supervisor:
Bachynski, Erin

June, 2022

NTNU Trondheim
Norwegian University of Science and Technology *Faculty of Engineering*
Department of Marine Technology

PROJECT THESIS IN MARINE TECHNOLOGY
SPRING 2022

for

Stud. Tech. Yu Ma

Novel modeling and fatigue analysis for early-phase design of a 15-MW FOWT

Ny modellering og utmattelsesanalyse for tidlig design av en 15-MW flytende havvindturbiner

Fatigue is an important consideration for offshore wind turbines, which encounter numerous load cycles due to waves, wind, and rotating machinery. Thousands of load cases have to be considered when designing against fatigue constraints, and using time domain aero-hydro-servo-elastic analysis can be expensive. Furthermore, as cost reductions move toward more steel-efficient hull designs, fatigue within the hull becomes increasingly important. This project will consider a specific case study of a FOWT, as decided together with the supervisor. The project work to be performed during Fall 2021 is to be carried out as follows:

1. As needed, extend the literature review into wave and wind statistical description (spectra), floating offshore wind turbine dynamics, fatigue and ultimate strength, environmental lumping methods and simplified models, artificial intelligence applied to fatigue assessment, relevant guidelines and standards, and existing approaches for estimating loads and fatigue damage in the hull.
2. Establish two coupled models in SIMA of the Volturn-US floating wind turbine: one with rigid hull (provided) and one with beams with distributed potential flow. Compare the natural periods and damping, responses in regular waves, and behavior in constant wind to check the compatibility of the models.
3. Establish a metocean design basis for studying the lifetime fatigue damage of the selected structure.
4. Establish a baseline estimate of the lifetime fatigue damage in several components (different locations along the tower, hull, and mooring system) through full long-term analysis.
5. Apply one or more environmental lumping methods to reduce the number of load cases, and compare the estimated fatigue damage to the full long-term analysis.
6. Conclusions and recommendations for further work.

The work scope may prove to be larger than initially anticipated. Subject to approval from the supervisors, topics may be deleted from the list above or reduced in extent.

In the project report, the candidate shall present his personal contribution to the resolution of problems within the scope of the project work

Theories and conclusions should be based on mathematical derivations and/or logic reasoning identifying the various steps in the deduction.

The candidate should utilise the existing possibilities for obtaining relevant literature.

Project report format

The project report should be organised in a rational manner to give a clear exposition of results, assessments, and conclusions. The text should be brief and to the point, with a clear language. Telegraphic language should be avoided.

The report shall contain the following elements: A text defining the scope, preface, list of contents, summary, main body of thesis, conclusions with recommendations for further work, list of symbols and acronyms, references and (optional) appendices. All figures, tables and equations shall be numerated.

The supervisors may require that the candidate, in an early stage of the work, presents a written plan for the completion of the work.

The original contribution of the candidate and material taken from other sources shall be clearly defined. Work from other sources shall be properly referenced using an acknowledged referencing system.

The report shall be submitted in electronic format (.pdf):

- Signed by the candidate
- The text defining the scope shall be included (this document)
- Drawings and/or computer models that are not suited to be part of the report in terms of appendices shall be provided on separate (.zip) files.

Ownership

NTNU has according to the present rules the ownership of the project reports. Any use of the report has to be approved by NTNU (or external partner when this applies). The department has the right to use the report as if the work was carried out by a NTNU employee, if nothing else has been agreed in advance.

Thesis supervisors:

Prof. Zhen Gao, NTNU, zhen.gao@ntnu.no

Prof. Erin Bachynski-Polić, NTNU, erin.bachynski@ntnu.no

Deadline: As decided on the web, some date in June, 2022

Trondheim, January 2022

Zhen Gao Erin Bachynski-Polić Svein Ersdal Andreas Watle

Candidate – date and signature: Yu Ma 11.06.2022
Trondheim

Preface

The master thesis is delivered as the final task of master's degree study in the department of Marine Technology at Norwegian University of Science and technology (NTNU). The thesis is aimed at making progress towards the floater hull analysis and fatigue estimation of ultra-scale FOWTs.

Firstly, I would express my endless gratitude to my supervisor, Professor Zhen Gao from the Department of Marine Technology of NTNU. His expertise in theory and experience in research work can always help me out of confusion. Without the guidance of him, the thorniest challenge cannot be tackled in time. Thanks for his patience and confidence in my work. I am likewise grateful to my co-supervisor, Professor Erin Bachynski-Polić from the Department of Marine Technology of NTNU, who initially provides the topic of master thesis. Her expertise in offshore wind and simulation tools accelerates my learning process. Without her inspiration in programming, my work regarding data processing cannot be finished that smoothly.

Heartfelt thanks should be given to Doctor Shuaishuai Wang who shares his knowledge and experience in scientific work. His emphasize of highlighting the theme corrects my academic writing. With his instruction, most of time is not wasted on meaningless explorations. Immense gratitude should also be expressed to Professor Lin Li from University of Stavanger (UiS). Her early work of metocean probability model provides technical support to the work in my thesis. Her comments about thesis writing contribute to the completeness of my work.

Finally, thanks to the department of Marine Technology of NTNU, where there are tremendous academic resources supporting my learning. The computational resource plays a vital role in my accomplishment of large-amount simulation task.

Yu Ma

Name: Yu Ma e-mail: hugomayu@foxmail.com

Trondheim, 11th June 2022

Abstract

Nowadays, extensive expectation is given to large-scale and even ultra-scale floating offshore wind turbine (FOWT) due to its potential in higher production efficiency. This idea is desired by global market but constrained by multiple technical challenges. One of those challenges is that substructures can be vulnerable to fatigue failure, for which the analytical methods and tools are not consummate enough. With the motivation of extending the application scenario of currently-available tools, a multi-body modeling method is practiced in this thesis.

Relevant input to the multi-body model is strictly controlled, returning very consistent performance compared with that of the initial rigid-floater model. This modeling scheme has the potential of being applied to fatigue analysis of floater hull. A tentative study to the dynamic response on floater hull is conducted. Although there exits the deficiency in section properties, the calculated dynamic load can still provide some insights into further study. The central column and pontoon are subjected to dramatically- oscillatory loads. The design of central column and pontoon should be circumspect to avoid severe fatigue failure. The results also indicate that the response at locations close to central column has similarities, strongly affected by pitch motions, while response of locations at the side is associated with surge motions.

The fully-coupled time domain simulations with 383 selected load cases are proceeded to evaluate the fatigue performance at tower base, since the sectional property of this location is confirmed. It should be noted that the analysis is conservative, since only wave and wind are aligned, coming from 0° direction. In this case, the fore-aft bending behavior is dramatic. Fatigue damage generally increases towards steeper wave and stronger wind. The most probable combinations of Hs and Tp under each wind speed are found to be at average fatigue level at given wind speed. Cases under each wind speed can be lumped into the most probable case at that wind speed. The fatigue prediction using 11 most probable cases out of 383 cases can return over 95% accuracy. If further simplifying the analysis using regression approach, 3 cases can limit the relative error into 5%.

Briefly, the main contribution of this thesis work is to provide insights into numerical modeling of floater hull and regularities of fatigue damage versus environmental variables. Useful information regarding the response of such a ultra-large FOWT is given as a reference for design and optimization.

Sammendrag

I dag stilles det store forventninger til storskala og til ultraskala flytende havvindmøller på grunn av potensialet i høyere produksjonseffektivitet. Denne ideen er ønsket av det globale markedet, men begrenset av flere tekniske utfordringer. En av disse utfordringene er at underkonstruksjoner kan være sårbare for utmattingssvikt, som de analytiske metodene og verktøyene ikke er komplette nok til. Med motivasjonen for å utvide bruksscenarioet til for øyeblikket tilgjengelige verktøy, praktiseres en flerkroppsmodelleringsmetode i denne oppgaven.

Relevant input til flerkroppsmodellen er strengt kontrollert, og gir svært konsistent ytelse sammenlignet med den opprinnelige modellen med stiv flyte. Dette modelleringsskjemaet har potensial til å bli brukt til utmattelsesanalyse av flyterskrog. En tentativ studie av den dynamiske responsen på flyterskrog er utført. Selv om mangelen på seksjonsegenskaper oppstår, kan den beregnede dynamiske lasten fortsatt gi noen innsikt i videre studier. Den sentrale søylen og pongtongen er utsatt for dramatisk oscillerende belastninger. Utformingen av sentralsøylen og pongtongen bør være konservative for å unngå alvorlig tretthetssvikt. Resultatene indikerer også at responsen på steder nær sentralsøylen har likheter, sterkt påvirket av stampebevegelser, mens responsen til steder ved siden er assosiert med bølgebevegelser.

De fullt koplede tidsdomenesimuleringene med 383 utvalgte lasttilfeller fortsetter for å evaluere utmattingsytelsen ved tårnbasen, siden seksjonsegenskapen til denne plasseringen er bekreftet. Det skal bemerkes at analysen er konservativ, siden bare bølge og vind er på linje, og kommer fra 0° retning. I dette tilfellet er bøyeadferden foran og bak spesielt stor. Tretthetsskader øker generelt med brattere bølger og sterkere vind. De mest sannsynlige kombinasjonene av Hs og Tp under hver vindhastighet er funnet å være på gjennomsnittlig utmattelsesnivå ved gitt vindhastighet. Sjøtilstander under hver vindhastighet kan grupperes sammen med andre mest sannsynlige tilfeller ved den vindhastigheten. Tretthetsprediksjonen med 11 mest sannsynlige tilfeller av 383 tilfeller kan gi over 95% nøyaktighet. Hvis analysen forenkles ytterligere ved bruk av regresjonstilnærming, kan 3 tilfeller begrense den relative feilen til 5%.

Kort fortalt er hovedbidraget til dette oppgavearbeidet å gi innsikt i numerisk modellering av flyterskrog og regulariteter av utmattelsesskader versus miljøvariabler. Nyttig informasjon om responsen til en slik ultra-stor FOWT er gitt som referanse for design og optimalisering.

Contents

List of Figures

List of Tables

List of Symbols

The next list describes several symbols that will be later used within the body of the document

ΔS —Stress Range

ΔS_{eq} —Equivalent Stress Range

η —motion amplitude/

ν —Poisson's Ratio

ω —Angular Velocity/Circular Frequency

Φ, ϕ —Velocity Potential/Attack Angular

ρ —Density

σ —Stress

a' —Angular Velocity Induced Factor

A —Added Mass

a —Velocity Induced Factor

ANN —Artificial Neural Network

B —Damping Coefficient

B_Q —Quadratic Damping Coefficient

BEM —Blade Element Method

C —Restoring Stiffness

C_D —Drag Coefficient

C_d —Drag Coefficient

C_L —Lift Coefficient

C_p —Power Coefficient

$Capex$ —Capital expense

CFD —Computational Fluid Dynamics

Cm —Added Mass Coefficient

D —Drag Force/ Fatigue damage

D^* —Fatigue damage multiplied by probability

DOF —Degree of Freedom

E —Young's Modulus

F_{exc} —Excitation Force

FDP —Fatigue Damage Parameter

FE —Finite Element

FLS —Fatigue Limit State

$FOWT$ —Floating Offshore Wind Turbine

FWT —Floating Wind Turbine

G —Shear Modulus

g —Gravity acceleration

GDW —product life cycle

GHG —Green House Gas

Hs —Significant Wave Height

I —Inertia

K —Stress Intensity Factor

L —Lift Force

$LEFM$ —Linear Elastic Fracture Mechanics

M —Bending Moment

N —Life cycles

n —Load cycles/Normal Vector

$NREL$ —National Renewable Energy Laboratory

$Opex$ —Operational expense

OWT —Floating Offshore Wind Turbine

P —Generator Power/Pressure

PLC —product life cycle

Q —Torque

RAO —Response Amplitude Operator

RNA —Rotor Nacelle Assembly

S —Area of cross section

T —Thrust Force

TLP —Tensor Leg Platform

Tp —Spectrum Peak Period

U —Potential Energy

u —Velocity

ULS —Ultimate Limit State

Uw —Mean Wind Speed

W —Work

X —Transfer Function of Excitation

x —Unknown Motion

Chapter 1

Introduction

1.1 Offshore Wind Energy

Sustainability has been the universally discussed topic in the past few decades. The goal of sustainability plus technological development enables modern energy dependence get transformed towards renewable energy. Among various options of renewable energy, wind energy is both economically-viable and technically-mature, and this option becomes desirable in energy industry. The installation and commercial operation of onshore wind farms started in last century and has experienced a rapid growth. The popularity of onshore wind farms has contributed to the global energy transition. However, further improvement of power production from onshore wind is limited by the available land space that can provide continuous and stable wind resources. To surpass this limitation, the focus is expanded to the broad ocean space, where the wind resources are more sufficient and reliable. Benefiting from the accumulated technology and experience in the offshore oil and gas industry, the idea of OWTs (Offshore Wind Turbine) becomes technically feasible [1].

Figure 1.1: Vindeby wind farm in Denmark.

https://www.siemensgamesa.com/en-int/explore/journal/2021/08/vindeby-30-anniversary-offshore

Up to today, offshore wind has played an important role in energy supply in many countries [2]. After the first offshore wind farm (Vindeby in Denmark in Figure 1.1) was built up in 1991, in the past 3 decades, the offshore wind turbine installation experienced a significant growth. Until 2021, there are in total 162 offshore wind farms operating worldwide. The distribution of different wind farms operating in Europe until 2021 is marked in Figure 1.2. Most of them are distributed around the UK and Denmark.

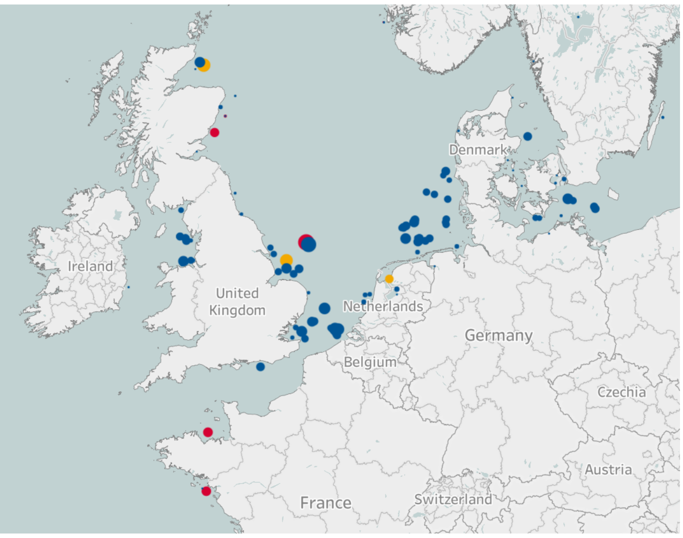

Figure 1.2: Wind farm distribution in Europe.

https://windeurope.org/intelligence-platform/product/european-offshore-wind-farms-map-public

The pressure from the goal of carbon neutrality drives people to look towards more productive offshore wind energy systems which have the capability to ease the urgent need for the wind energy. As the cost of offshore wind (including both Opex and Capex) has decreased to (78-125) \$/MWh by 2020, estimated to decrease to (44-72) \$/MWh by 2050 [3], the proposal of larger wind turbine becomes both economically and technically feasible. The improved price competence makes one of the drive forces to upscale wind turbines in the global energy market.

1.2 Floating Offshore Wind Turbine

The offshore wind structures that came into operation in the early age applied the bottom-fixed type of substructure design, like monopile structure and jacket structure. Conventionally, the bottom-fixed offshore wind structures are installed close to the shore, sited in the shallow water area. The requirement for structure strength is very strict, coming along with the higher cost on steel structure, when the design depth is increased.

Granted, exploitable shallow water sites are minor compared to deep-water areas. Those deep-water areas contain great potential for wind power generation. One of the feasible solutions that works for deep-water area is to apply floating offshore wind turbine (FOWT). The FOWT is moored and stabilized by the mooring lines or tether legs fixed on the sea bottom. The cost-effectiveness of FOWTs was already illustrated by Musial et al. [4]. Since then, floating offshore wind farms have been given with extensive focus. This solution is quite promising for capturing wind energy in the area of deep sea. Such confidence in FOWTs came from the promising results of the first floating wind farm named Hywind Scotland operated from 2017, as shown in Figure 1.3. The total capacity of this wind farm is 30 MW, and the substructures are the spar-buoy design. After that, the confidence in FOWTs has been increasing and more prototypes in different forms are come up with, such as tensor leg platform (TLP) and semi-submerisble platform.

Figure 1.3: Hywind Scotland floating offshore wind farm.

https://www.windpowerengineering.com/worlds-first-floating-wind-farm-delivers-promising-results

The conception of FOWT has already existed for at least 20 years. The related study of Henderson [1] demonstrated the feasibility of applying the floating design in oil industry to the design of offshore wind substructure (including semi-submersible and TLP). Unlike the bottom fixed offshore wind system, FOWTs confront more complex coupling induced by both aerodynamic loads and hydrodynamic loads. Moreover,these environmental loads are coupled with the transmission of mechanical system, dynamic response of mooring lines and the elasticity in the structure. Therefore, the system is a highly-coupled system, which gives large complexity in designing and optimization.

1.3 Design Standard

The design of offshore wind structures should guarantee both functionality and operational safety. When it comes to the aspect of safety, different design standards should be satisfied, including designing criteria related to ultimate limit states (ULS) and fatigue limit states (FLS). The standard related to ULS requires the structure can sustain the extreme loads under the worst environmental condition. The verification is to compare the strength capacity with the extreme load under 100-year environment condition. However, the fatigue life evaluation of the structure is more complex. since all the relevant cyclic load components can contribute to the fatigue damage. With such complexities, fully-coupled time domain simulations are repeated to get a relatively accurate estimation of the load response at different locations. The load response time series can be used to produce the time series of stress on the cross section. Based on the time series of stress on the cross section, the equivalent stress range can be obtained through counting the load cycles. It is the input of the referred SN curve provided in DNVGL-RP-C203 [5] to estimate the fatigue damage. A safe design should satisfy that the estimated life expectancy is longer than the designed life expectancy.

As the concept of large-scale FOWTs (10 MW) and even ultra-scale FOWTs (15 MW) are put forward, the fatigue issue can be intractable, since the load magnitude is also upscaled. The substructures are subjected to dramatic dynamic loads, exposed to high risk of fatigue failure. Efficient analytical methods and tools are needed in the entire product life cycle (PLC). For example, in the production design stage, very thorough numerical simulations and repeated experiments are exactly practiced to guarantee the future operational safety. In the early design phase, a simplified method of fatigue analysis is marked as applicable which is given to help determine a prototype and support the lateral optimization work.

1.4 Review of Relevant Work

In the early design phase of FOWTs, a simplified method should be time-efficient, convincing and easy-to-operate. If the time domain simulations are used for fatigue analysis, the goal of a simplified method is to estimate fatigue damage at different locations with fewer simulations. Regarding this goal, there are two main challenges. The first challenge is to exploit the potential of today's numerical simulation tool, making it possible to return response at any locations of FOWTs. The second challenge is to develop a proper method to reduce simulation workload for fatigue analysis. Some studies related to these two challenges are reviewed in this section.

1.4.1 Relevant Work in Dynamic Analysis to Floater Hull

Conventionally, in the time domain simulations of offshore wind system, the tower, blades and mooring lines are described as elastic beams, which enables the calculation of sectional response. The hull of floater is regarded as a rigid body. This scheme is able to simplify the modeling procedure since the kinetic description of the floater can be limited to a movable point. However, the inner response of floater is unable to be captured. Several studies have explored the calculation of response on the hull of floaters. Kvittem and Moan [6] studied the fatigue of a semi-submersible platform. The fatigue damage was calculated through modifying the braces into beam elements. Morison formulation is used to describe the hydrodynamics of those slender beams. Svendsen [7] studied the internal load of a TLP platform supporting a 5 MW wind turbine, with potential flow theory being implemented in multi-body hydrodynamics. Hegseth [8] used the same method as Svendsen [7] to study the dynamic response of a semi-submersible platform. Brevik [9] applied the method used by Svendsen [7], comparing with the result using Morison model. In his work, the spar platform is divided into many sections to study the stress RAOs of both 10 MW and 15 MW FOWTs. The method applied by Svendsen [7], Hegseth [8] and Brevik [9] simplified the modeling in state-of-the-art code namely SIMO/RIFLEX. The method still needs to be improved, since the bias in rotational added mass and damping is a little obvious for the semi-submersible case. Differently, Luan et al. [10] adopted a method which strictly controlled the input to SIMO/RIFLEX code where the entire semi-submersible floater was divided into 28 sub-bodies. This method is more accurate but complicated comared with other methods. Furthermore, Liu and Takeshi [11] implemented this idea in another code named AQWA, with one-third of the pontoons and braces of a semi-submersible being modified into elastic connections to analyze the fatigue damage, giving that the horizontal loads contributed most to the fatigue of pontoons. Based on the works mentioned above, the technique used by Luan et al. [10] is refered and one-third of the objective UMaine VorturnUS-S floater is modified into sub-bodies. Some cross sections are defined to examine the loading behavior that occurs to the central column, pontoon and side column.

1.4.2 Relevant Work in Reduction of Simulation Cases

When it comes to the simplification of fatigue analysis by reducing cases, there have been different studies working on this issue. Most of them made progress for the bottom-fixed offshore wind system. For the simplification of fatigue study of bottom fixed floating wind system, many studies focused on the simplification of environmental condition set. The sampling strategy of lumping environmental condition was explored by those studies. Passion and Branner [12] applied a wave lumping method for condensation of the wave climates. This method did not take the coupling between the lumped wave climate and the wind climate into consideration. The different strategies of wave lumping were compared and a new method was come up with, which presented better performance. Passon [13] has also developed a new wind-wave correlation method, based on the damage contour lines, compared with existing methods. The method of Passon returned quite accurate hydrodynamic fatigue damage at all selected locations, but there was a high requirement for the quality of wind-wave correlation established. Zwick and Muskulus [14] explored two methods, piece-wise linear approximation and multi linear regression to train the data from different jacket platform with varying wind speed and lumped sea state. This method could provide good accuracy but required additional time for training the model. Velarde and Bachynski [15] applied a parameter named fatigue damage parameter (FDP) to associate the environmental parameters with the fatigue damage of a monopile substructure. After that, the most representative sea states were selected based on the long-term distributions of wind and wave to reduce calculation effort. This approach gave 90% accuracy with 30% of total number of conditions.

Häfele et al. [16] studied two jacket platforms and applied a sampling strategy that the full set was divided into subsets based on the probability. This methods had the potential to reduce the computational effort but produced large error when the subset was too small. Instead of focusing on environmental conditions alone, Stieng and Mukulus [17] focused on the damage of each load case and applied the severity-based sampling method, getting 30 load cases out of 3647 produced less than 2% error. Most of these studies also indicated that the wave load contributed most to the fatigue damage of the substructure.

When it comes to the fatigue analysis of FOWTs, due to the non-linearity in the system, there is higher complexity in the relationship between stress response and environmental loads. The existing studies of reducing simulations does not apply the methods mentioned above. More complicated strategies like aritificial neural networks (ANN) are exploited in the study of fatigue of FOWTs. Stewart [18] explored four different strategies to simplify the fartigue analysis of a spar-buoy and a semi-submersible floating wind system. Among these strategies, the bin reduction and probability-based sampling can produce quite accurate results with fewer simulations, however, the results of response surface method lacks of fidelity. Müller et al. [19] combined response surface method with stochastic techniques. The statistical characteristics of environmental parameters were taken through Latin Hypercube Sampling (LHS), while the simulation results were put into ANN model to establish the response surface. However, the convergence requires at least around 100 samples and there was uncertainties in the ANN results. Also, Müller and Cheng [20] applied sobol sequence based on Monte Carlo sampling procedures to select representative load cases for sampling. The convergence results indicates 200 samples can give 90% confidence of the damage estimation. Kim et al. [21] developed a frequency domain approach considering wind and wave loads. The stress transfer function was developed utilizing ANN model. This method regarded the wind and wave loads as independent from each other, and the superposition principle was used. The effectiveness of reducing computational effort was optimistic, but the accuracy needed improvement through adjusting the ANN model. The ANN model can be a powerful tool to perform the regression study to the data set, but it requires additional training time with existing data.

The methods discussed above have different complexity. From the perspective of the author, the preferable method should be as simple and time-saving as possible. Some complicated sampling technique and ANN focus on the data itself. However, a general solution should be developed from the mechanism behind interactions between the structure and environment. The correlation between fatigue damage and environmental variables as well as related mechanism are important for reasoning the fatigue result. Therefore, if there is relationship between environment and fatigue damage, a lumping method is preferable to simplify the fatigue analysis from the perspective of the author of this thesis.

1.5 Thesis Scope & Outline

As described in the background, the topic of this thesis is put forward due to the interest in the further implementation of ultra-scale concept model. The safe operation of FOWTs in this scale can be gravely threatened by the risk of fatigue failure at substructures. To make the analysis in early-phase design efficient and reliable. Improvement in modeling and analysis is state-of-the-art. Driven by the motivation of pushing the offshore wind industry into a high-power era, the thesis works on the improvement of numerical modeling. The fatigue regularity of an ultra-scale FOWT is also explored to provide designers some insights to the fatigue problem.

With the background and motivation that are introduced, the following chapters focus on relevant theory, modeling details and results from fatigue analysis.

In chapter 2, the basic theories and methods are introduced, including the theories applied in the integrated time domain analysis, principally regarding hydrodynamics and aerodynamics. Also the theory and methods of fatigue study is presented.

In chapter 3, the information about the selected FOWT model is introduced and environment conditions of selected working site is described. The model information and environmental conditions are the inputs to the simulation tasks for coupled analysis.

In chapter 4, numerical modeling process of the selected FOWT is documented. SIMO/RIFLEX in SIMA is the main numerical tool used for fully-coupled time domain simulations. The model implemented in this chapter contains flexible blades, mooring lines, tower and a rigid floater. This chapter includes some testing results of the time domain simulations and the model is verfied through comparison with results in IEA report [22].

In chapter 5, an improvement towards a more advanced modeling scheme is discussed, which enables the capture of dynamic responses on the floater itself. The newly-built flexible-floater model is compared with the rigid-floater model for keeping kinetic and dynamic consistency. The cross-sectional response at column and pontoon are presented as reference for design and optimization.

In chapter 6, large number of simulations are proceeded for fatigue analysis. regularities from simulations are summarized. The data from simulations are processed to find out a simplified manner for estimating fatigue damage.

In chapter 7, the findings from simulation results are summarized and recommendations for future work are listed.

Chapter 2

Theoretical Background

2.1 Time Domain Simulations

When it comes to the hydrodynamic analysis of the offshore structures, the frequency domain approach has been universally applied in the offshore oil and gas industry. With the knowledge and tools for floating structure analysis, the preliminary analysis of FOWT applied the linearized frequency domain approach to examine the feasibility of the design. This method works efficiently based on linear potential flow theory to obtain the RAO as well as eigenfrequencies [23, 24]. However, the frequency domain analysis cannot implement the strong non-linear dynamic characteristics [25, 26, 27]. Furthermore, the transient events including system control and wind turbine fault can not be modeled in the frequency domain approach [26]. To implement the aero-hydro-servo-elastic features and emulate those transient events, a fully-coupled time domain simulation approach was recommended. The corresponding simulation tools have also been developed and examined by the market [28] to fulfill the fully-coupled time domain simulations. One of the commonly-used tool is the open-sourced tool named OpenFast containing Aerodyn and Hydrodyn modules developed by NREL. It has abundant interface with other tools for further analysis, as stated in FAST user's guide [29]. The other mature tool is the SIMO/RIFLEX code provided by Sintef Ocean [30, 31]. With development, the aerodynamic module is integrated with the SIMO/RIFLEX in SIMA. The SIMO/RIFLEX can also couple with WAMIT to account for the distributed hydrodynamic load. This set of codes is the tool utilized for the work of this thesis.

When it comes to the fully-coupled time domain simulations repeated into many iterations for the full assessment of fatigue issue, various variables related to wind, wave and current are needed to be considered [19].

- For the wind itself, the variables include wind speed, wind direction, turbulence intensity, wind shear, wind spectrum and coherence structure.

- For the wave itself, the wave height, period, wave direction and wave spectrum should be considered.

- For the current, there is the consideration of current speed, direction and vertical profile.

Most of the studies only took the wind and wave into account, if focusing on the fatigue of tower and hull body. The reason for this can be that the current contributes to the mean load on the body, while the load cycle matters for the fatigue problem. Also, the simulation bin sizes and time length can affect the accuracy of the results. Several studies investigated this issue. Kvittem et al. [32] studied the difference between the fatigue estimate of 6 realisations of 1-h time length and that of 10 3-h realisations. Kvittem and Moan [6] emulated 10 realisations of 197 3-h environmental conditions and pointed out that 1-hour simulations only returns 4% RMS error compared to 3-hour simulations. It turns out that suitable bin sizes can be 2 m/s for wind, 1 s for wave periods and 1 m for wave heights. This setting can be used for producing quite convincing fatigue damage estimation. The further discussion about details of time-domain simulations is in Section 4.

2.2 Aerodynamic Loads

The aerodynamic loads acted on the wind turbine has significant contribution to the global dynamic response. The integration of lift and drag force at the airfoil cross sections gives the thrust force and torque. The thrust spurs the surge and pitch motions of the structure. The torque provides the force driving the turbine to spin. It causes slight roll motions, since there is a torque being transferred from generator to the floater while the turbine is spinning. The frequency of the rotation of wind turbine is also important for the design. The noted frequencies mainly include the rotation frequency of the rotor and the blade passing frequency, namely 1p and 3p frequencies. The two frequencies are important when performing the spectrum analysis, checking if there is resonance between bending behavior of the structure components and the rotation of the wind turbine. For the analysis of aerodynamic load on the wind turbine, the BEM and GDW are the ideal methods compromising both accuracy and computational efficiency, compared with 1-dimensional momentum method and conventional CFD method. The BEM approach is based on the momentum theory and theory of airfoil. In the Section 2.2.1, the one-dimensional momentum theory and Betz limit are introduced. The basics of airfoil are introduced in Section 2.2.3 and the BEM approach is described in Section 2.2.4.

2.2.1 One-dimensional Momentum Theory and Betz Limit

The thrust and power of an ideal wind turbine can be determined with the one-dimensional actuator disk rotor model. This model assumes the flow to be homogeneous, incompressible and steady-state. The conservation of momentum can be expressed as

$$T = v_0(\rho A_0 v_0) - v_1(\rho A_1 v_1) \tag{2.2.1}$$

The frictional force is neglected and the Bernoulli equation is applied on either side of the rotor.

$$\begin{aligned} P_0 + \frac{1}{2}\rho v_0^2 &= P_A + \frac{1}{2}\rho v_A^2 \\ P_B + \frac{1}{2}\rho v_B^2 &= P_1 + \frac{1}{2}\rho v_1^2 \end{aligned} \tag{2.2.2}$$

Here, it is assumed that the flow is continuous the velocity on the left should be equal to the velocity on the right, denoted $v_A = v_B$. The pressure far from the disk should also be equal, $P_1 = P_0$. The pressure drop can be obtained by the difference of the two equations in Equation 2.2.2. The thrust force is equal to the pressure drop integrated in the rotor disk area.

$$T = \int_A (P_A - P_B)dA = \frac{1}{2}\rho A(v_0^2 - v_1^2) \tag{2.2.3}$$

The thrust force can also be expressed as the momentum in unit time when the flow passes the rotor disk. $\dot{m}$ is the net mass of the flow.

$$\begin{aligned} T &= \dot{m}(V_0 - V_1) \\ \dot{m} &= \rho A v_A = \rho A v_B \end{aligned} \tag{2.2.4}$$

With the equation Equation 2.2.3 and Equation 2.2.4, the $v_A = \frac{1}{2}(v_0 + v_1)$. The axial induction factor is defined as follow.

$$\begin{aligned} a &= \frac{v_0 - v_A}{v_0} \\ v_A &= v_0(1 - a) \\ V_1 &= v_0(1 - 2a) \end{aligned} \tag{2.2.5}$$

The power captured by the rotor is equal to the change in kinetic energy. With this relationship, an expression with the axial induction factor a is written as Equation 2.2.6.

$$P = \frac{1}{2}\rho A v_A(v_0^2 - v_1^2) = \frac{1}{2}\rho v_0^3 4a(1 - a^2) \tag{2.2.6}$$

The maximum power production can be obtained when the $\frac{dP}{da} = 0$, of which the solution is $a = \frac{1}{3}$. The power coefficient can be defined as $C_p = \frac{P}{\frac{1}{2}\rho v_0^3 A}$. It can be expressed with axial induction factor a only.

$$C_p = 4a(1 - a)^2 \tag{2.2.7}$$

The solution of the maximum power production gives the maximum power coefficient. This is called the Betz limit. The $C_{Pmax} = \frac{16}{27}$.

2.2.2 Wake Rotation

In practice, the torque exerted by the blades causes the flow to rotate (opposite the direction of the rotor). Since the turbine gives kinetic energy to the wake, a rotating turbine cannot achieve the hypothetical Betz limit. But when the tip speed ratio is improved, the power coefficient will be very close to the Betz limit. The angular velocity imparted to the free stream is defined as ω and the angular velocity of the rotor as Ω. The angular induction factor can be defined as $a' = \frac{\omega}{2\Omega}$. The equation of pressure jump considering the wake rotation can be written as

$$P_B - P_A = \rho(\Omega + \frac{1}{2}\omega)\omega^2 \tag{2.2.8}$$

Based on the conservation of momentum, the thrust and torque can be written into

$$\begin{aligned} dT &= 4a(1-a)\frac{1}{2}\rho v_0^2 2\pi r dr \\ dQ &= 4a'(1-a)\frac{1}{2}\rho v_0 \Omega r^2 2\pi r dr \end{aligned} \tag{2.2.9}$$

2.2.3 Basics of Airfoil

Before introducing the BEM method, the basics of airfoil should be introduced. The general working principle of the airfoil cross section is illustrated by the Figure 2.1.

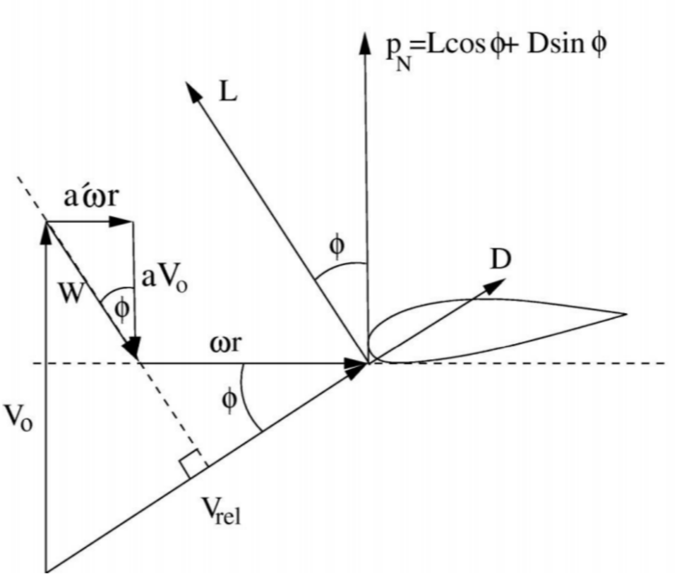

Figure 2.1: Velocity triangle of blade cross section [33].

When the air passes the airfoil, the pressure difference between the upper surface and lower surface produces the lift force, while the pressure loss generates the drag force. The lift force and drag force coefficients can be written as

$$\begin{aligned} C_L &= \frac{L/l}{\frac{1}{2}\rho U^2 c} \\ C_D &= \frac{D/l}{\frac{1}{2}\rho U^2 c} \end{aligned} \tag{2.2.10}$$

In the equations the L and D are lift and drag force respectively, while the c is the camber length. When summing up the normal and tangential components of lift and drag forces, the thrust and torque of unit length of wind turbine can be written into

$$\begin{aligned} dT &= B(L\,\cos\phi + D\,\sin\phi)dr \\ dQ &= B(L\,\sin\phi - D\,\cos\phi)dr \end{aligned} \tag{2.2.11}$$

In these equations, B is the number of blades and the dT and dQ are the thrust and torque of unit radius respectively.

2.2.4 Blade Element Method (BEM)

The BEM method is a iteration method based on the momentum theory and airfoil theory. The normal and tangential induction factors is approximated with values to calculate the flow angle according to the Equation 2.2.12. With the Equation 2.2.10 and Equation 2.2.11, the angle of attack and the lift and drag coefficients can be obtained. Then, the induction factors can be updated using the relation in Equation 2.2.9.

$$\begin{aligned} a &= \frac{1}{\frac{4\sin^2\phi}{n} + 1} \\ a' &= \frac{1}{\frac{4\sin\phi\cos\phi}{t} + 1} \end{aligned} \tag{2.2.12}$$

If the solution has converged, the process ends. If not, the flow angle has to be recalculated with the updated induction factors and the process mentioned above should be repeated. The equations of the BEM method described so far demands some necessary corrections. The Prandtl correction corrects for flow around the blade tip, which may result in the tip of the blade producing less aerodynamic force. The Glauert Correction corrected the induction factors greater than 0.5, since the wind velocity in the far wake would be negative.

There is also the dynamic wake effect that should be considered. The reaction of the induced velocities to the change of wind speed is slow due to the shedding and downstream convection of vorticity. Dynamic wake effects are most apparent for heavily loaded rotors, of which the induction factors are large. In a BEM code, this effect can be modeled by the Stig Øye dynamic inflow model, which acts as a filter for induced velocities [34]. The dynamic stall is another issue needed to be considered. Due to the dynamic incoming wind, there are sudden attachment and re-attachment of flow, and the angle of attack is actually always changing. There is a time lag for the aerodynamic load to react to the change of attack angle. The consequence of such a time lag is that the transient loads can be large, as the airfoil might still experience a high lift coefficient after a sudden increase in wind speed. The aerodynamic module used in SIMA is based on the BEM method. It is used for the calculation of wind load in this thesis.

2.3 Hydrodynamic Loads

When it comes to the calculation of hydrodynamic loads, the potential flow theory and Morison equation are commonly used. They are applied for different conditions due to that the dominant force component varies with the geometry characteristics like the size, as illustrated in Figure 2.2.

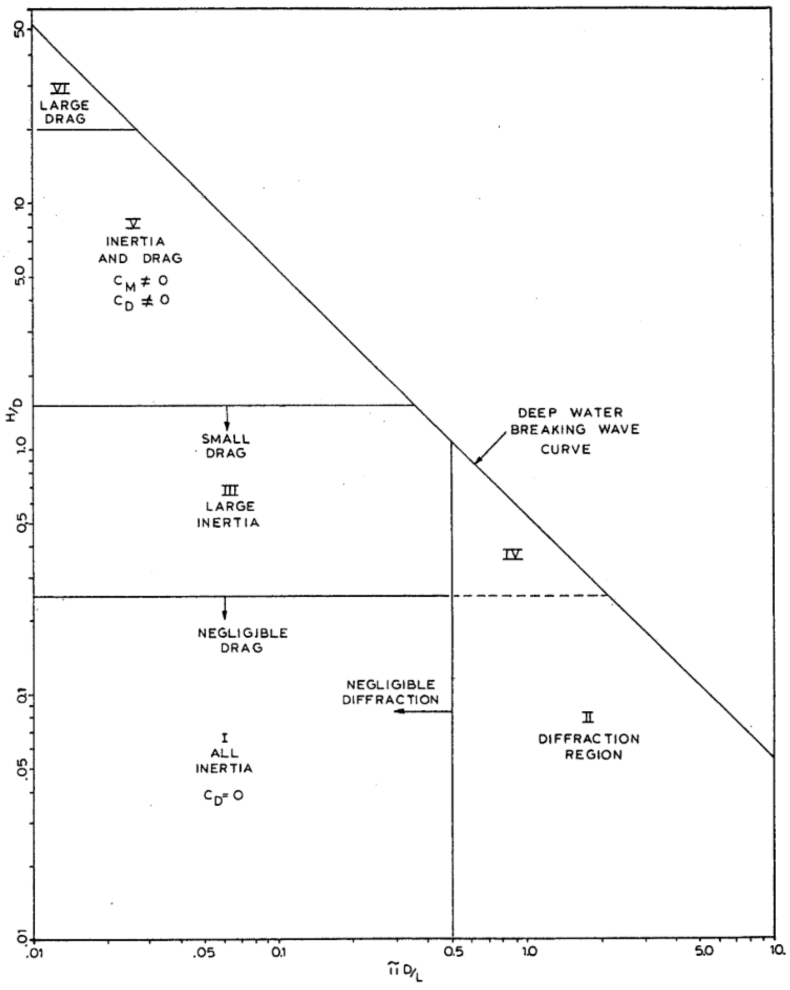

Figure 2.2: Regions of applying formula of wave loads [35].

In Figure 2.2, the effect of drag force increases along the y axis as the wave height is increased, while the effect of diffraction increases along the x axis as the wave length is decreased. The size of the components of semi-submersible floaters is located in the region 4, where the diffraction is important and drag effect is non-negligible. Linear potential flow theory considering drag effect is befitting this scenario. When it comes to the mooring lines, the drag effect is significant and the diffraction effect is negligible due to the small diameter of cross section. Morison equation is appropriate for hydrodynamics of mooring lines. In this section, the hydrodynamic analysis based on potential flow theory is expounded and Morison equation is briefly introduced.

2.3.1 Linear Potential Flow Theory

The hydrodynamic problem of a semi-submersible floater can be resolved through combining linear potential flow theory and dynamic rigid body motion equations. Linear potential flow theory is sufficient to describe the flow behavior in this scenario. The motion of the floater can be described through establishing the equation of rigid body motions, while the coefficients are computed based on potential flow theory. To calculate the hydrodynamic coefficients using potential flow theory, the problem can be the superposition of two parallel sub-problems (diffraction problem and radiation problem) [36].

- When considering the diffraction problem, the body is assumed to be restrained from oscillation. It interacts with the incident waves. The incident wave imposes forces and moments to the body, which consist of the Froude-Krylov and diffraction forces.
- In the radiation problem, there is no incident wave inflicted to the body. The body is forced to oscillate in its six degrees of freedom. The loads are due to the interaction between the water and body when the body is oscillating, which gives the added mass, damping and restoring force components. The added mass and damping forces are associated with the dynamic pressure due to the body motions. The hydrodynamic restoring force is caused by the variation of the hydro-static pressure. These forces with unit acceleration, velocity and displacement make the hydrodynamic coefficients on the left side of the dynamic equilibrium.

The total time-dependent velocity potential can be written as the linear combination of the velocity potentials of diffraction and radiation problems. The capital letter Φ is marked as the time-dependent velocity potential.

$$\Phi_{total} = \Phi_{diffraction} + \Phi_{radiation} \tag{2.3.1}$$

For the diffraction problem, the load imposed on the wet body can be splited into two parts. Imagining there is no existent object to interfere the flow, the flow just generate force with the velocity potential of Φ_0. The load caused by the incident wave itself is called Froude-kriloff load. Also, the existence of the body changes the moving direction of the flow, generating waves. The generated wave introduces additional load. This phenomenon is exactly called diffraction, giving the velocity potential Φ_D, and corresponding load is named diffraction load. The velocity potential can be written as the sum of ϕ_0 and ϕ_D.

$$\Phi_{diffraction} = \underbrace{\Phi_0}_{incident} + \underbrace{\Phi_D}_{diffraction} \tag{2.3.2}$$

Then the wave excitation load can be written as

$$F_{exc,k} = -\int_{S_{OB}} \rho \frac{\partial \Phi_0}{\partial t} n_k dS - \int_{S_{OB}} \rho \frac{\partial \Phi_D}{\partial t} n_k dS, \ {\scriptstyle k=1,2,3,4,5,6} \tag{2.3.3}$$

Here, the k numbers the direction of the force or moments. The transfer function of excitation force is defined as the excitation force introduced by unit wave height, which is used in the numerical simulations. The wave spectrum is predefined and the excitation load is calculated through multiplying wave height with the transfer functions.

$$X_k = \frac{F_{exc,k}}{\zeta_a}, \ {\scriptstyle k=1,2,3,4,5,6} \tag{2.3.4}$$

For the radiation problem, as mentioned, the load is caused by the wave generated by the oscillation of the body. The velocity potential can be written as

$$\Phi_R = \mathcal{R}\left\{\sum_{j=1}^{6} \dot{\eta}_j \phi_j\right\}, \ {\scriptstyle j=1,2,3,4,5,6} \tag{2.3.5}$$

Here, j denotes the degree of freedom of motions. η means the oscillatory motions in six degree of freedom.

$$\eta_j(t) = \mathcal{R}\left\{\eta_{ja}\, e^{i\omega t}\right\}, \ {\scriptstyle j=1,2,3,4,5,6} \tag{2.3.6}$$

With the velocity potential, the radiation force can be derived as Equation 2.3.7. S_{OB} means the surface area of wetted body. As mentioned, the hydrodynamic restoring force is caused by the variation of the buoyancy. It is associated with the hydrostatic pressure. The added mass and damping forces are connected with the dynamic pressure due to the body motions. The radiation force can be written as the sum of added mass and damping force.

$$F_{rad,k} = -\int_{S_{OB}} \rho \frac{\partial \Phi_R}{\partial t} n_k dS = \sum_{j=1}^{6} -\{A_{kj}\ddot{\eta}_j + B_{kj}\dot{\eta}_j\}, \ {\scriptstyle k,j=1,2,3,4,5,6} \tag{2.3.7}$$

2.3.2 Descritized Added Mass, Damping Coefficients and Transfer Functions of Excitation

The hydrodynamic added mass, damping and excitation force of each panel can be obtained through integrating the pressures from radiation and diffraction potentials. The Wamit output OPTN.5P file gives the pressure components for computing the hydrodynamic coefficients. The linear dynamic pressure can be written as the time derivative of the velocity potential according to Bernoulli's equation.

$$P = -\rho \frac{\partial \Phi}{\partial t} \tag{2.3.8}$$

the time-dependent velocity potential can be written into the space-dependent velovity potential multiplied by a harmonic time-dependent term

$$\Phi_D(x, y, z, t) = \mathcal{R}\left\{\phi_D(x, y, z)e^{iwt}\right\} \tag{2.3.9}$$

The time-dependent diffraction pressure can be written as

$$P_D = -i\,\omega\,\rho\,\Phi_D(x, y, z, t) \tag{2.3.10}$$

Then, the space-dependent diffraction pressure can be written as

$$p_D = -i\,\omega\,\rho\,\phi_D(x, y, z) \tag{2.3.11}$$

The excitation force term is found by integration of velocity potential of diffraction over the wetted body surface.

$$X_j = -i\omega\rho \iint_{S_B} n_i\,\phi_D\,dS = \iint_{S_B} n_i\,p_D\,dS, \;\; {\scriptstyle j=1,2,3,4,5,6} \tag{2.3.12}$$

The radiation velocity potential is defined as

$$\Phi_R = \mathcal{R}\left\{i\omega \sum_{j=1}^{6} \eta_j\,\phi_j,\right\} \quad j = 1, 2, 3, 4, 5, 6 \tag{2.3.13}$$

The space-dependent radiation pressure due to unit motion can be written as

$$p_{Rj} = \omega^2\,\rho\,\eta_{aj}\,\phi_j, \;\; {\scriptstyle j=1,2,3,4,5,6} \tag{2.3.14}$$

The added mass and damping coefficients can be obtained through integrating the radiation velocity potential. It can be finally written as the expression with the dynamic pressure caused by unit motion.

$$A_{k,j} - \frac{i}{\omega} B_{k,j} = \rho \iint_{S_B} n_k\,\phi_j = \frac{1}{\omega^2} \iint_{S_B} n_k\,\frac{p_{Rj}}{\eta_{aj}}\,dS, \;\; {\scriptstyle j,\,k=1,2,3,4,5,6} \tag{2.3.15}$$

In Wamit, the lower-order panel method is used, which assumes the velocity potential on each panel is constant. Then, the hydrodynamic coefficients can be calculated in a simplified manner. The pressure on the panel can be written as the multiplication of the panel area and averaged pressure. The dS in the formula is the area of panel, of which the value equals to 1. When it comes to the added mass, damping coefficients and transfer function of excitation force on individual panels, Equation 2.3.16 is used to get the distributed transfer functions of excitation force, added mass and damping coefficients, applied in the computer program Wamit [37].

$$\begin{aligned} X_{j,pnl} &= n_k \, p_D \, dS \\ A_{k,j,pnl} - \frac{i}{\omega} B_{k,j,pnl} &= \frac{1}{\omega^2} n_k \, \frac{p_j}{\eta_{aj}} \, dS \end{aligned} \tag{2.3.16}$$

2.3.3 Hydrodynamics of Flexible Multi-body Model

The hydrodynamic added mass and damping coefficients as well as excitation force transfer function of each section predefined are obtained through integrating over each panel on the surface of the wet body. The output from Wamit code includes:

- Added mass matrix [6 x 6]
- Damping matrix [6 x 6]
- Transfer function of excitation force vector [6 x 1]

There are 60 wave periods defined and 11 wave directions of incident waves, the algorithm is to loop over the 60 periods to get the added mass and damping of each wave period, and get the excitation force transfer function of each wave period under each wave direction. Therefore the target matrix or vector size for each section are as follows

- Added mass matrix [60 x 6 x 6]
- Damping matrix [60 x 6 x 6]
- Transfer function of excitation force vector [60 x 11 x 6 x 1]

The hydrodynamic terms for a given section is the summation of that on each panel within the section. If there is N panels on the given section, the sectional added mass, damping and excitation force can be written as

$$\begin{aligned}A_{sec} &= \sum_{n=1}^{N} A_{pnl,n} \\ B_{sec} &= \sum_{n=1}^{N} B_{pnl,n} \\ X_{sec} &= \sum_{n=1}^{N} X_{pnl,n}\end{aligned} \tag{2.3.17}$$

2.3.4 Hydro-static & Gravitational Loads on Flexible Multi-body Model

The hydro-static loads acted on the body contributes to the motion of the platform and calculation of internal forces. The restoring coefficients and gravity distribution should be given reasonably, which can accurately describe both motion and mechanical behavior of the platform. The restoring force and moment due to water pressure and buoyancy movement can be calculated with the formula given in Wamit theory manual [38] as listed in Equation 2.3.18. Among these two equations, $\vec{\eta} = [\eta_1, \eta_2, \eta_3, \eta_4, \eta_5, \eta_6]^T$ is the vector of 6-DOF motions, of which the former three terms represent the translational motion and the other three represent rotational motions. This can also be written as $\vec{\eta} = [\vec{\zeta}, \vec{\theta}]^T$. $\vec{x} = [x, y, z]^T$ and $\vec{n} = [n_x, n_y, n_z]^T$ are the vector of location under global coordinate and normal vector respectively. Equation 2.3.18 given with unit translational and rotational motion can compute the C matrix, which is $[6 \times 6]$.

$$\begin{aligned}F_{res} =& -\rho g \int\int_{S_B} (\vec{\theta} \times \vec{n}) z dS \\ & -\rho \int\int_{S_B} \vec{n} g(\eta_3 + \eta_4 y - \eta_5 x) dS \\ M_{res} =& -\rho g \int\int_{S_B} (\vec{x} \times \vec{n})(\eta_3 + \eta_4 y - \eta_5 x) dS \\ & -\rho g \int\int_{S_B} (\vec{\zeta} \times \vec{n}) z dS \\ & -\rho g \int\int_{S_B} [\vec{\theta} \times (\vec{x} \times \vec{n})] z dS\end{aligned} \tag{2.3.18}$$

In addition, the moment introduced by the movement of gravity when there is an angle of inclination contributes to pitch and roll motions. This moment can be written as

$$\begin{aligned}M_{grav}^{(4)} &= mgz_g\theta_1 \\ M_{grav}^{(5)} &= mgz_g\theta_2\end{aligned} \tag{2.3.19}$$

The stiffness matrix introduced by hydro-static loads and gravity can be written as

$$K = \begin{bmatrix} 0 & & & & & \\ & 0 & & & & \\ & & C_{33} & C_{34} & C_{35} & \\ & & C_{43} & C_{44} - mgz_g & C_{45} & \\ & & C_{53} & C_{33} & C_{55} - mgz_g & \\ & & & & & 0 \end{bmatrix} \tag{2.3.20}$$

The K matrix of each panel on the wet surface can be calculated using the formula mentioned above and integrated over each section predefined. This can produce the sectional stiffness needed for describing the motions of the entire platform.

$$K_{sec} = \sum_{n=1}^{N} K_{pnl,n} \tag{2.3.21}$$

2.3.5 Morison Equation

For slender system like the mooring lines, the Morison formula is sufficient to account for the hydrodynamic load effect. The Morison formula is written as

$$F = \underbrace{\rho C_m V \dot{u}}_{Inertia} + \underbrace{\frac{1}{2} \rho C_d A u |u|}_{Drag}, \tag{2.3.22}$$

The Morison's equation is a semi-empirical formula for the in-line force. There are two empirical hydrodynamic coefficients, the C_m is the coefficient of added mass and the C_d is the drag coefficient. The first force component is the inertia (mass) term, which coincides with the excitation force based on potential-flow long-wave approximation (when $C_m = 2$). This means the validity is restrained to large wave length compared to the diameter. The valid range is given as $\lambda/D > 5$. The drag force is the in-line viscous force. It is connected with the pressure loss due to the boundary layer and the flow separation and with the frictional stresses along the body. The C_m and C_d are associated with Re, KC numbers and roughness [39]. For calculation convenience, the C_m and C_d are usually assumed to be constant.

2.4 Rigid Body Motion & Retardation Function

If the floater of FOWT is regarded as a point, the motion of the floater can be described by the equilibrium of rigid-body motion. The equilibrium can be written as

$$(M + A)x^{''} + Bx^{'} + Cx = F_{exc} \tag{2.4.1}$$

In the equilibrium, M is the mass of object, A is the added mass, B is the damping coefficient and C is restoring stiffness. The x represents the unknown displacement, excited by the excitation force marked as F_{exc}. Since the motion or the excitation is associated with the wave elevation, which can be written into the form with $e^{i\omega t+\epsilon}$. If differentiating two sides of Equation 2.4.1, the frequency-domain formulation for a linear system can be written as Equation 2.4.2. What should be noticed is that here the restoring term is given with C matrix which is expressed by hydro-static pressure, since the program has introduced the gravity effect. If the gravity effect is not additionally considered, the C matrix here should be replace by K matrix given in Equation 2.3.20.

$$-\omega^2(M + A(\omega))x(\omega) + i\omega B(\omega)x(\omega) + Cx(\omega) = F_{exc}(\omega) \tag{2.4.2}$$

Since time domain simulation is the approach used for analysis, the frequency-domain hydrodynamic coefficients should be transferred to time domain. Applying the Inverse Fourier Transform, the Equation 2.4.2 can be written into

$$-\omega^2(M + A_\infty)x(t) + \int_{-\infty}^{\infty}(i\omega a(\omega) + b(\omega))i\omega x(\omega)e^{i\omega t}d\omega + Cx(t) = f_{exc}(t) \tag{2.4.3}$$

The second term with an integration is the convolution term. This term reflects that the radiation force has a memory effect. In the time domain simulation, this can be described by the retardation function, the retardation function can be defined as

$$k(\tau) = \frac{1}{2\pi}\int_{-\infty}^{\infty}(i\omega a(\omega) + b(\omega))e^{i\omega\tau}d\omega \tag{2.4.4}$$

The equation of motions can be written into

$$(M + A_\infty)\ddot{x}(t) + \int_{-\infty}^{\infty}k(t-\tau)\dot{x}(\tau)d\tau + Cx(t) = f_{exc}(t) \tag{2.4.5}$$

The second term is the convolution of the retardation function and velocity. The retardation function is what is used in the SIMO program to transform the frequency-domian input to time-domain input. it is used for estimating the radiation forces on the body in time domain analysis.

2.5 Beam Formulation

In the fully-coupled analysis of FOWTs, the rigid bodies are modeled as points connected by beam elements, for example, the hub is connected to the floater by the tower. The assumption for the mechanics of beams is Euler-Bernoulli beam theory which assumes the material to be linear-elastic. The Euler-Bernoulli beam is shown in Figure 2.3.

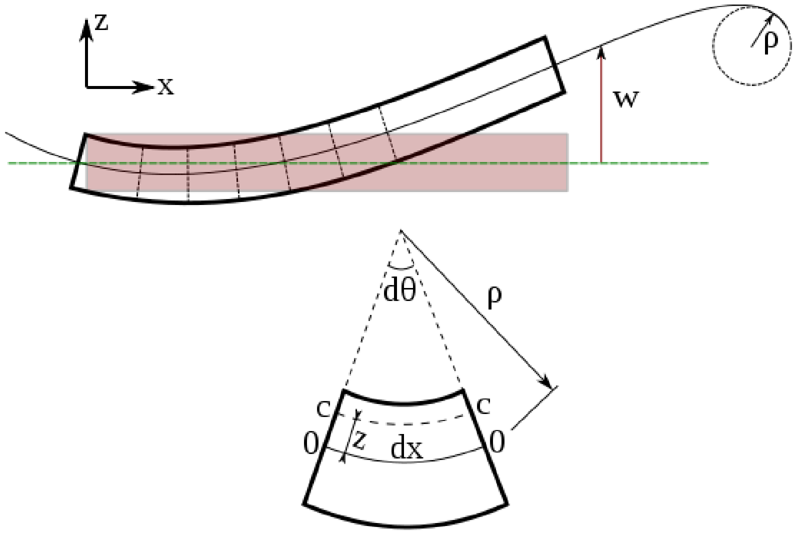

Figure 2.3: Euler-Bernoulli beam illustration.

https://commons.wikimedia.org/wiki/File:Euler-Bernoulli$_{b}eam_{t}heory.png$

The relationship between external distributed load and deflection of the beam can be written as

$$\frac{d^2}{dx^2}(EI\frac{d^2w}{dx^2}) = q(x) \tag{2.5.1}$$

In Equation 2.5.1, q is the external load, E is the Young's module, I is the inertia of cross section, and w is the curvature. Based on D'Alembert's principle, the inertia force can be regarded as a correction to the external load. This helps associate the equilibrium with the structural mass. The equilibrium can be rewritten into

$$\frac{d^2}{dx^2}(EI\frac{d^2w}{dx^2}) + \rho A(x)\frac{d^2w}{dt^2} = q(x,t) \tag{2.5.2}$$

The equation can be solved only if the EI and ρA are constant. Using a letter μ to replace ρA, this equation can be further written into

$$EI\frac{d^4w}{dx^4} + \mu\frac{d^2w}{dt^2} = q(x,t) \tag{2.5.3}$$

This is the dynamic equilibrium of the vibration of a beam after receiving impulse. The solution of the partial differential equation (PDE) is the oscillation time series. The $\frac{d^2w}{dx^2}$ can be solved using Raleigh-Ritz method, which assumes the solution as a sum of assumed functions, or it can be solved through Finite Element (FE) method.

The solution can be used for the calculation of cross-sectional bending moment and shear force as follows.

$$\begin{aligned} M &= -EI\frac{d^2w}{dx^2} \\ Q &= -\frac{d}{dx}(EI\frac{d^2w}{dx^2}) \end{aligned} \tag{2.5.4}$$

2.6 Fatigue Damage Analysis

The fatigue failures of the components of structures result from the cycled loading history. Usually for engineering structures, the loading history is random. To build up a reference standard to predict fatigue damage or fatigue life, the crack formation can be divided into two stage, the crack initiation stage and crack growth stage. The Paris law is used to describe the crack growth above a certain threshold.

$$\frac{da}{dN} = C\Delta K^m \tag{2.6.1}$$

Here, The $\frac{da}{dN}$ is the crack growth rate, C and m are constant values. The ΔK is the range of stress intensity factor. This is defined based on linear elastic fracture mechanics (LEFM). It is expressed as

$$\Delta K = \Delta S\,\sqrt{\pi a}\,F \tag{2.6.2}$$

F is the parameter accounts for the geometry shape. The Equation 2.6.2 gives the relationship between crack growth rate and local stress intensity around the crack tip. Then the fatigue life can be obtained by intergrating the dN.

$$N = \int_{a_i}^{a_f} \frac{da}{da/dn} = \int_{a_i}^{a_f} \frac{da}{C(\Delta S\sqrt{\pi}F)^m a^{m/2}} = \frac{{a_f}^{1-m/2} - {a_i}^{1-m/2}}{C(\Delta S\sqrt{\pi}F)^m (1\text{–}m/2)} \tag{2.6.3}$$

2.6.1 SN Curve

Adapting Equation 2.6.3 into logarithmic form, the SN curve formula can be expressed as

$$\begin{gathered} logN + mlog\Delta S = logA \\ A = C(\sqrt{\pi}F)^m\,(1\text{–}m/2) \end{gathered} \tag{2.6.4}$$

The empirical SN curve given in DNVGL-RP-C203 [40] refers to plate thickness of 25mm. There is a need of recalculating the equivalent stress range when the given thickness is larger.

$$\Delta S = \Delta S_{\text{ref}} \left(\frac{t_{\text{ref}}}{t}\right)^k \tag{2.6.5}$$

The SN-curve given in DNVGL-RP-C203 [40] is shown in Figure 2.4, the turning points around 10^{-7} have taken the low cycles into consideration.

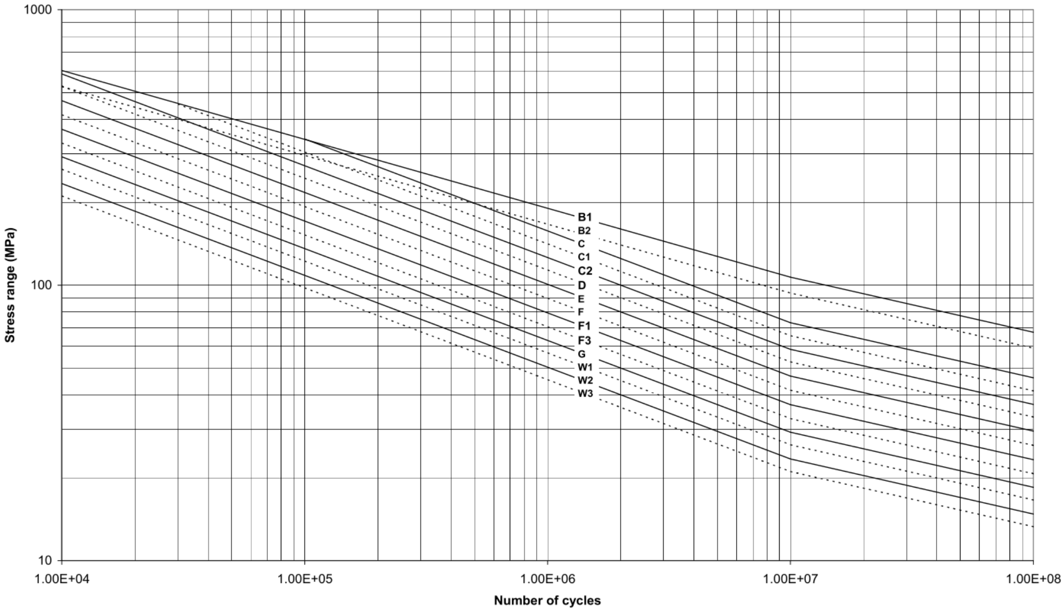

Figure 2.4: SN-curve in DNVGL-RP-C203.

The fatigue design limit state of marine structures generally follows the SN curve given in DNVGL-RP-C203. The input of the SN curve should be the equivalent stress range obtained from random load history.

2.6.2 Rain Flow Counting

The rainflow counting [41] is a commonly used technique to get the equivalent stress range from the history of random loads. The important random loads include axial force F_a, fore-aft bending moment M_y and side-side bending moment M_z. The normal stress time series is computed from the times series of these loads d through

$$S(t) = \frac{F_a(t)}{A} + \frac{M_y(t)\,z}{I_y} + \frac{M_z(t)\,y}{I_z} \tag{2.6.6}$$

The general idea of train flow counting is to count the cycles of the strain deformation. The count of load cycles is done by finding terminations of flow. The flows terminates when it merges with the flow starts from previous tensile peak or it encounters an opposite tensile peak with larger amplitude. Also, it ends at the end of time series. The process is shown in the Figure 2.5, where the half cycles counted include 0-1, 1-2, 2-3, 3-4, 4-5. The WAFO toolbox [42] provides the functions to perform the rainflow counting.

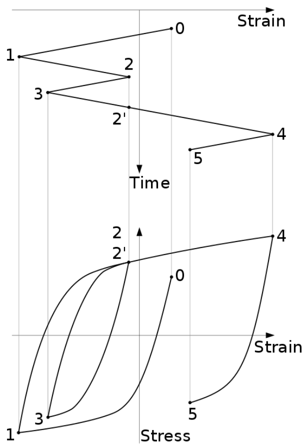

Figure 2.5: Rainflow counting example.

https://commons.wikimedia.org/wiki/File:Rainflow_counting_vs_stress-strain_curve.svg

After counting the load cycles, the equivalent stress range can be calculated through

$$\Delta S_{eq} = \left[\frac{\sum_i n_i (\Delta S_i)^m}{\sum_i n_i} \right]^{1/m} \tag{2.6.7}$$

For the continuous load history, the load cycles can be assumed to follow a 2-parameter Weibull distribution. The equivalent stress range is the input of SN curve.

$$\Delta S_{eq} = \frac{\Delta S_0}{(\ln n_0)^{1/h}} \left[\Gamma \left(1 + \frac{m}{h} \right) \right]^{1/m} \tag{2.6.8}$$

To calculate the fatigue damage, the Miner sum rule is used

$$D = \sum_i \frac{n_i}{N_i} \tag{2.6.9}$$

The exact 1-hour fatigue damage contribution under each working condition should be multiplied with the probability of that working condition, which can be noted as D^*. If the working condition is determined by wind speed, significant wave height and time period, the fatigue damage contribution can be written as

$$D^* = D\ f_{U_w,H_s,T_p}(u,h,t) \tag{2.6.10}$$

The total fatigue damage considering all possible working conditions can be written as

$$D^*_{tot} = \sum_{i=1}^{n} D^{(i)}\ f^{(i)}_{U_w,H_s,T_p}(u,h,t) \tag{2.6.11}$$

Chapter 3

Wind Turbine Parameters & Environmental Conditions

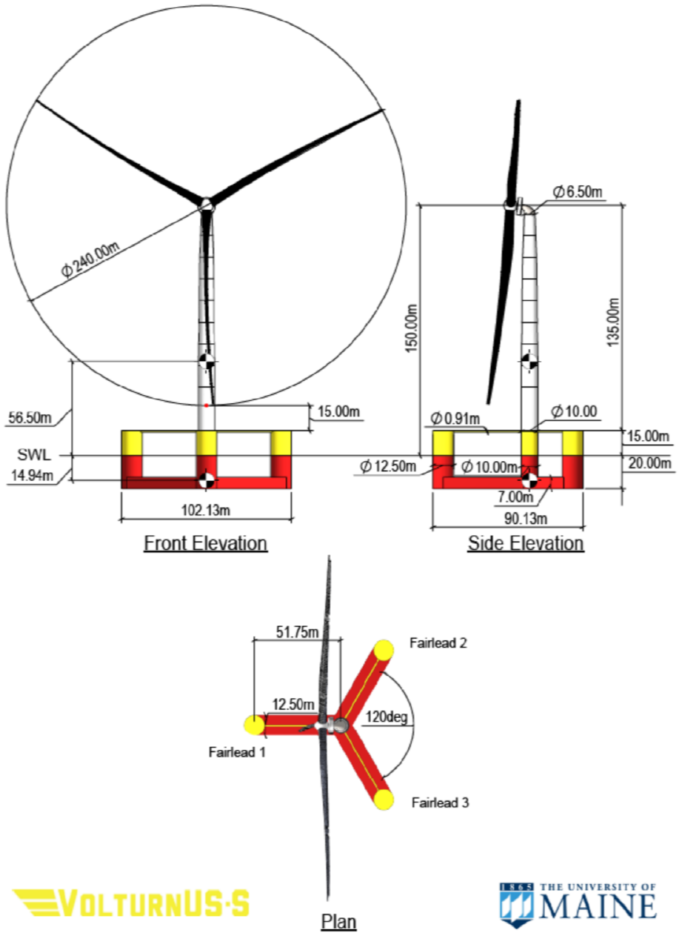

Figure 3.1: General properties of UMaine model [22].

This section principally prepares for the practice of time domain simulations. The input to the simulation tool is the model information and environmental state. A general description of the concept of 15 MW FOWT is described first. After that, the target site and related environmental model is introduced.

3.1 Description of 15 MW Floating Wind System

The model selected for the study in this thesis is the IEA Wind 15-Megawatt offshore wind turbine [43]. The corresponding supporting structure is the UMaine VolturnUS-S platform. This platform is a semi-submersible floating structure stablized by buoyancy and mooring lines. It has the pros of high flexibility and easy installation. It also has the cons including large footprint on the seabed and large relative translational motions. In the work of this thesis, the substructure of the 15 MW FOWT is focused. The concept model of tower and floater is shown in Figure 3.2.

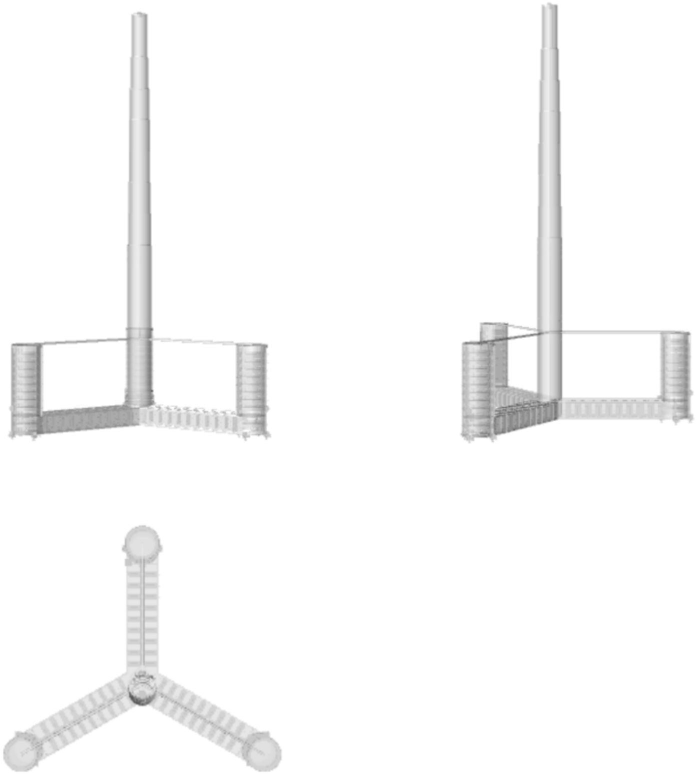

Figure 3.2: Concept Model of the substructure.

3.1.1 Tower Description

The general properties of the tower is given by the IEA report [22]. As described in the report, the tower was designed as an isotropic steel tube with high stiffness.

The designed fore-aft and side-side bending frequency was out of the 1P and 3P frequency. The properties are listed in Table 3.1.

Parameter	**Value**	**Units**
Mass	1263	tonne
Length	129495	m
Base Outer Diameter	10	m
Top Outer Diameter	6.5	m
1st Fore-Aft Bending Mode	0.496	Hz
1st Side-Side Bending Mode	0.483	Hz
E	2.00e+13	Pa
G	7.93e+12	Pa
ρ	7850	kg/mˆ3

Table 3.1: Properties of floating tower.

Along the tower, the cross section and thickness are varying. The numerical model built in SIMA follows the parameters of each cross section listed in Table 3.2.

Height [m]	**Outer Diameter** [m]	**Thickness**[mm]
15.000	10.000	82.954
28.000	9.964	83.073
41.000	9.967	82.799
54.000	9.927	29.900
67.000	9.528	27.842
80.000	9.149	25.567
93.000	8.945	22.854
106.000	8.735	20.250
119.000	8.405	18.339
132.000	7.321	21.211
144.000	6.500	21.211

Table 3.2: Tower dimensions of different cross section.

3.1.2 Floater Description

The floater of the IEA 15 MW model is composed of one central column and three side columns which are connected by the pontoons. The Table 3.3 gives the parameters which are used for the hydrostatic verification. The important parameters include the area and inertia of the cross sections.

The floater is not given with detailed designing parameters, especailly the inner layout and mass distribution. To estimate the fatigue damage at the floater, the parameters of the columns and pontoons are estimated based on assumed plate thickness. The relevant properties are given in the Table 3.4.

Parameter	**Value**	**Units**
Hull Displacement	20206	mˆ3
Hull Steel Mass	3914	tonne
Tower Interface Mass	100	tonne
Ballast Mass (Fixed/Fluid)	2540/11300	tonne
Draft	20	m
Freeboard	15	m
Vertical Center of Gravity from SWL	-14.94	m
Vertical Center of Buoyancy from SWL	-13.63	m
Roll Inertia	1.25e+11	kg*mˆ2
Pitch Inertia	1.25e+11	kg*mˆ2
Yaw Inertia	2.36e+10	kg*mˆ2

Table 3.3: Basic parameters of the floater.

	Central Column	**Side Column**	**Pontoon**
ρ[**kg/m^3**]	7850	7850	7850
t[**mm**]	80	80	80
$\mathbf{S}_{in}$[**m**]	78.2256	112.4564	87.1104
$\mathbf{S}_{out}$[**m**]	78.5398	113.0973	87.5
E[**Pa**]	2.10e+11	2.10e+11	2.10e+11
ν	0.3	0.3	0.3
G[**Pa**]	7.69e+10	7.69e+10	7.69e+10
$\mathbf{I}_y$[**m^4**]	3.9191	11.5032	7.2139
$\mathbf{I}_z$[**m^4**]	3.9191	11.5032	1.74E+01
$\mathbf{I}_p$[**m^4**]	22.974	7.8304	24.5645
EA[**N**]	6.60e+10	1.35e+11	8.18e+10
$\mathbf{EI}_y$[**Nm^2**]	8.23e+11	2.42e+12	1.51e+12
$\mathbf{EI}_z$[**Nm^2**]	8.23e+11	2.42e+12	3.64e+12
$\mathbf{GI}_y$[**Nm^2**]	3.01e+11	8.85e+11	5.55e+11
$\mathbf{GI}_z$[**Nm^2**]	3.01e+11	8.85e+11	1.33e+12

Table 3.4: Properties of the floater columns and pontoons.

3.2 Model of Joint Probability Distribution

Figure 3.3: Approximate location of the selected site named Norway 5.

The applied site for operation is the site named Norway 5, of which the joint distribution of is established by Li et al. [44]. The location of the site is marked in the map in Figure 3.3. The model is developed based on 10-year measured data. The water depth is approximately 200m, which is suitable for the utilization of the semi-submersible platform. The given probability model describing the joint distribution of H_s, T_p and U_w can be written as

$$f_{U_w,H_s,T_p}(u,h,t) = f_{U_w}(u) \cdot f_{H_s|U_w}(h|\, u) \cdot f_{T_p|H_s}(t|\, h) \tag{3.2.1}$$

This probability model is a simplified model, the conditional distribution of T_p with given U_w and H_s is replaced by the conditional distribution of T_p with given H_s. The marginal distribution of mean wind speed U_w follows the two-parameter Weibull distribution.

$$f_{U_w}(u) = \frac{\alpha_u}{\beta_u}(\frac{u}{\beta_u})^{\alpha_u-1} \cdot exp[-(\frac{u}{\beta_u})^{\alpha_u}] \tag{3.2.2}$$

The α_u and β_u are shape and scale parameters respectively, $\alpha_u = 2.209$ and $\beta_u = 9.409$. The conditional PDF of H_s over U_w is given as a two-parameter Weibull distribution.

$$f_{H_s|U_w}(h|\, u) = \frac{\alpha_{HC}}{\beta_{HC}}(\frac{h}{\beta_{HC}})^{\alpha_{HC}-1} \cdot exp[-(\frac{h}{\beta_{HC}})^{\alpha_{HC}}] \tag{3.2.3}$$

Here, the α_{HC} and β_{HC} are shape and scale parameters respectively, expressed by the form of power functions of mean wind speed. The a_1, a_2, a_3, b_1, b_2 and b_3 are the parameters obtained by fitting the raw hindcast data.

$$\begin{aligned} \alpha_{HC} &= a_1 + a_2 \cdot u^{a_3} \\ \beta_{HC} &= b_1 + b_2 \cdot u^{b_3} \end{aligned} \tag{3.2.4}$$

conditional distribution of Tp given Hs, the data follow as lognormal distribution.

$$f_{T_p|H_s}(t|\,h) = \frac{1}{\sqrt{2\pi}\sigma_{LCT}t} \cdot exp[-\frac{1}{2}(\frac{ln(t) - \mu_{LCT}}{\sigma_{LCT}})^2] \tag{3.2.5}$$

μ_{LCT} and σ_{LCT} are the mean value and the standard deviation of $ln(t)$. Here, the μ_{LCT} and σ_{LCT} are written as the functions of H_s, while the c_1, c_2, c_3, d_1, d_2 and d_3 are the parameters obtained by smoothing the H_s.

$$\begin{aligned} \mu_{LTC} &= c_1 + c_2 \cdot h^{c_3} \\ \sigma^2_{LTC} &= d_1 + d_2 \cdot exp(d_3 h) \end{aligned} \tag{3.2.6}$$

With the joint distribution of environmental condition, the next step is to define the working conditions as the input of time domain simulations (different combinations of H_s, T_p and U_w). Kvittem et al. [6] studied the influence of simulation bin size, number of seeds and simulation time duration. Due to that this study applied the data from specific numerical model, the exact input applied in this thesis should be re-evaluated.

Before running simulations to study the fatigue of the 15 MW FOWT, the number of cases can be estimated roughly. According to the IEC standard [45], the bin size of mean wind speed, significant wave height and peak wave period should be 2m/s, 0.5m and 0.5s respectively. The input of H_s, T_p and U_w are as follows

- H_s: [1,6] with bin size 0.5m
- T_p: [4,12] with bin size 0.5s
- U_w: [4,22] with bin size 2m/s

The probability of these inputs in total is very close to 100%, and the scatter diagrams are produced based on these inputs. The example of $U_w = 8m/s$ is shown in Figure 3.4. The highest probability is marked with red color, while lowest with green color. scatter diagrams of different wind speed are attached in Appendix C.

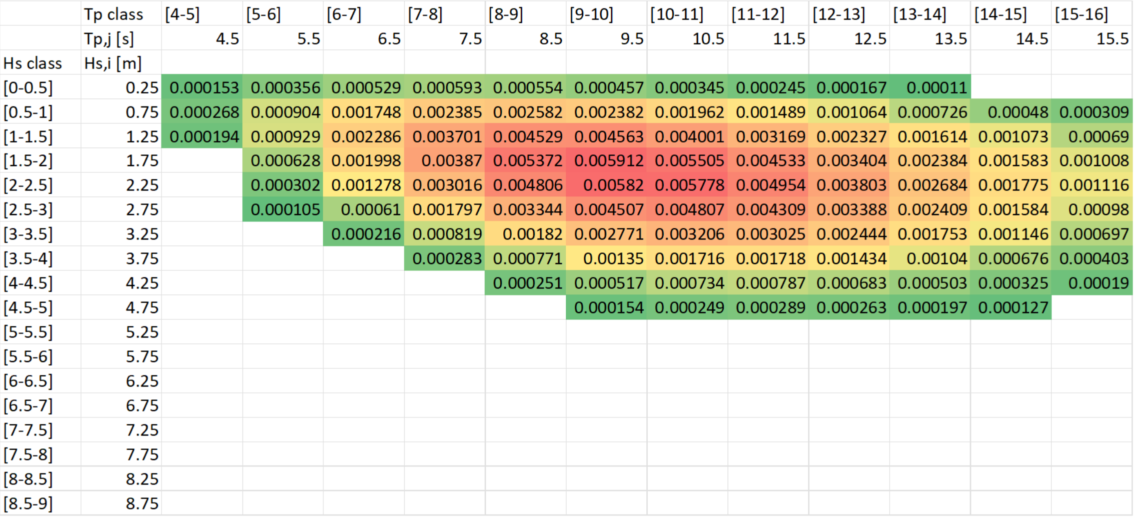

	Tp class	[4-5]	[5-6]	[6-7]	[7-8]	[8-9]	[9-10]	[10-11]	[11-12]	[12-13]	[13-14]	[14-15]	[15-16]
	Tp,j [s]	4.5	5.5	6.5	7.5	8.5	9.5	10.5	11.5	12.5	13.5	14.5	15.5
Hs class	Hs,i [m]												
[0-0.5]	0.25	0.000153	0.000356	0.000529	0.000593	0.000554	0.000457	0.000345	0.000245	0.000167	0.00011		
[0.5-1]	0.75	0.000268	0.000904	0.001748	0.002385	0.002582	0.002382	0.001962	0.001489	0.001064	0.000726	0.00048	0.000309
[1-1.5]	1.25	0.000194	0.000929	0.002286	0.003701	0.004529	0.004563	0.004001	0.003169	0.002327	0.001614	0.001073	0.00069
[1.5-2]	1.75		0.000628	0.001998	0.00387	0.005372	0.005912	0.005505	0.004533	0.003404	0.002384	0.001583	0.001008
[2-2.5]	2.25		0.000302	0.001278	0.003016	0.004806	0.00582	0.005778	0.004954	0.003803	0.002684	0.001775	0.001116
[2.5-3]	2.75		0.000105	0.00061	0.001797	0.003344	0.004507	0.004807	0.004309	0.003388	0.002409	0.001584	0.00098
[3-3.5]	3.25			0.000216	0.000819	0.00182	0.002771	0.003206	0.003025	0.002444	0.001753	0.001146	0.000697
[3.5-4]	3.75				0.000283	0.000771	0.00135	0.001716	0.001718	0.001434	0.00104	0.000676	0.000403
[4-4.5]	4.25					0.000251	0.000517	0.000734	0.000787	0.000683	0.000503	0.000325	0.00019
[4.5-5]	4.75						0.000154	0.000249	0.000289	0.000263	0.000197	0.000127	
[5-5.5]	5.25												
[5.5-6]	5.75												
[6-6.5]	6.25												
[6.5-7]	6.75												
[7-7.5]	7.25												
[7.5-8]	7.75												
[8-8.5]	8.25												
[8.5-9]	8.75												

Figure 3.4: Example of scatter diagram of joint probability distribution [$U_w = 8\,\mathrm{m/s}$].

Chapter 4

Numerical Modeling of 15 MW FOWT

With the theoretical support, the time domain analysis starts from modeling a coupled model with a rigid floater. This model is firstly compared with the given results in IEA report to verify its usability. After that, it is set as a reference for the modeling of a flexible multi-body floater model. The verification of the flexible multi-body floater model is through comparing the kinetic and dynamic performance with the rigid-body model. In other words, the modeling of rigid-body floater is the foundation for the exploration of modeling flexible floater.

4.1 Modeling of Rigid Floater

The setup of fully-coupled time domain analysis requires different numerical models built in different numerical tools. The state-of-the-art computer codes applied for the preparation of coupled analysis include GeniE [46], HydroD [47] (containing WADAM), SIMA (containing SIMO and RIFLEX) and Wamit [37]. The time domain simulation of the rigid-floater model is based on SIMO/RIFLEX code. In SIMO, the floater is a rigid floater, the total hydrodynamic coefficients are added to the floater. A technical roadmap is developed to illustrate the modeling and analysis with the state-of-the-art codes, as shown in Figure 4.1.

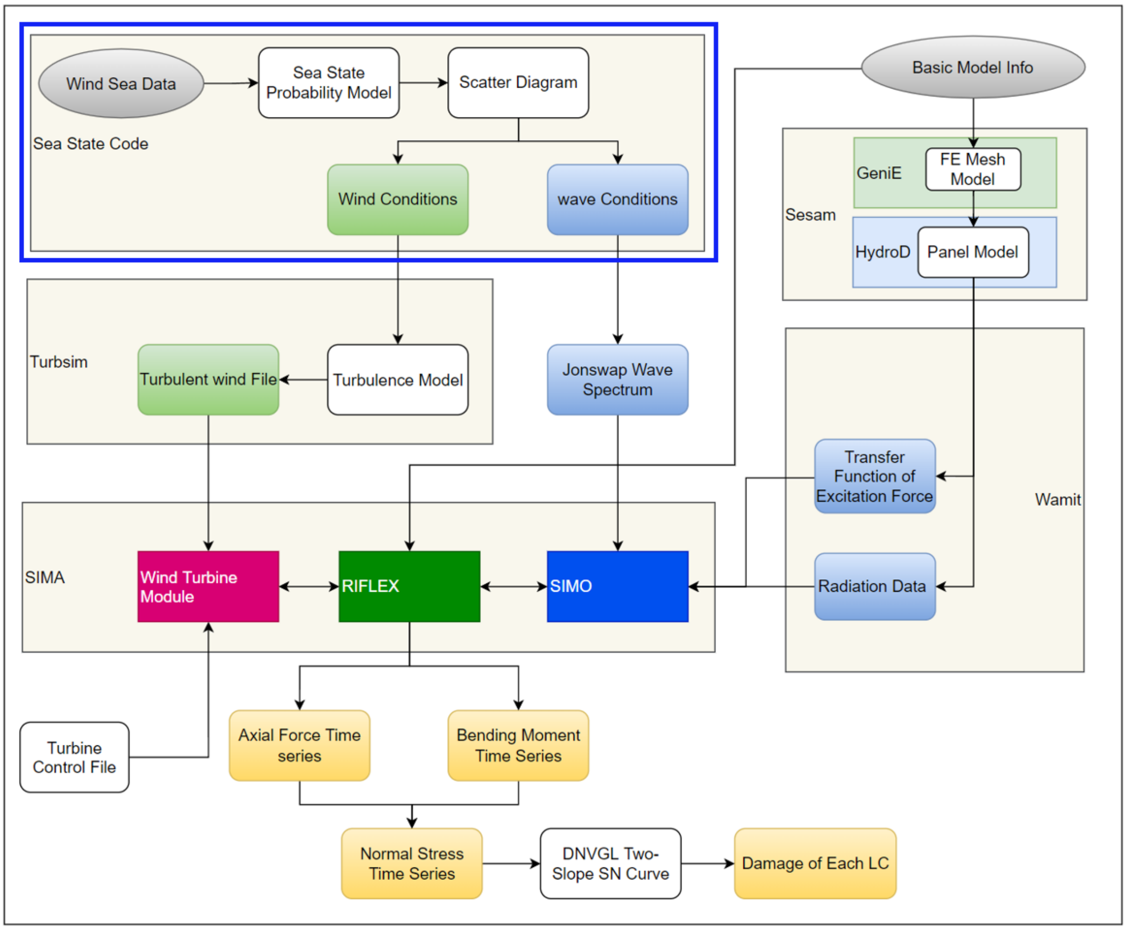

Figure 4.1: Working flow of rigid-floater numerical coupled model for fatigue analysis (based on time domain simulations).

Figure 4.1 visualizes the procedure of implementing fatigue analysis with the rigid-floater numerical model. Starting from the top left corner in Figure 4.1, the Sea State Code is self-developed in order to generate scatter diagrams of loading cases (LC), marked in the blue block. This code also enables the calculated fatigue damage is mapped to scatter diagrams. Turbsim [48] code generates turbulent wind based on the scatter diagrams. The wind files are input to the aerodynamic module in SIMA. From the top right corner, the basic model information is used for building numerical model in Sesam code package from DNV. Panel model built in Sesam code package is transferred to Wamit for both hydrodynamic radiation and diffraction coefficients, which are input into SIMO module to describe the rigid body motions in waves. In SIMA, The aerodynamic and hydrodynamic loads are transformed to the beam elements defined in RIFLEX module, and then the dynamic response of the structure like turbine blades, tower and mooring lines can be computed. The normal stress time history can be computed from nodal load history, and Rainflow counting technique can be used for counting load cycles. Then, the equivalent stress range can be obtained and input into the two-slope SN curve to get the damage of corresponding loading case. The total damage can be calculated with Miner sum method.

4.1.1 Panel Model - GeniE & HydroD &WAMIT

The Sesam software GeniE [46] and HydroD [47] are utilized to build up the panel model for the hull of the floater. In GeniE, a finite element (FE) model is established based on the geometry of the concept model. The mesh is drawn on the surface of the geometry with relatively fine mesh. The diagonal length of the grid is 0.5 meter, which is sufficient for the hydrodynamic analysis [7, 36]. The FE model built in GeniE is shown in Figure 4.2

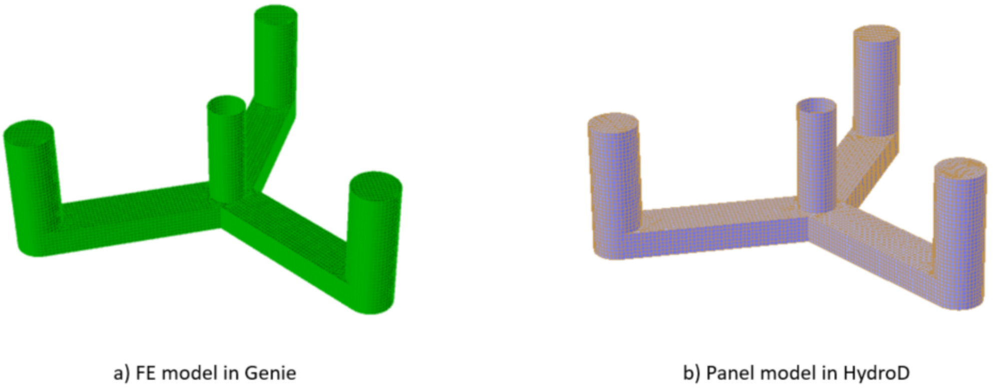
a) FE model in Genie

b) Panel model in HydroD

Figure 4.2: FE model in GeniE and panel model in HydroD.

The FE model is imported into HydroD to generate the 3D panel model. The panels are created based on the FE grids to capture the hydrodynamic pressure. The FE model and panel model are shown in Figure 4.2. The wave direction is from 0 deg to 180 deg with 11 directions. The wave frequency ranges from 0.01 rad/s to 5 rad/s with 60 frequencies. The mass is calculated with the option "fill from buoyancy", being approximately 20679 tonnes, which is very close to the mass given in Table 3.3.

4.1.2 Hydrodynamic Inputs to SIMO/RIFLEX

As mentioned above, panel model built in Sesam HydroD is utilized to calculate the coefficients regarding diffraction and radiation. This calculation is finished in Wamit. Appendix A includes both the plots of radiation and diffraction terms. Observed from the plot of excitation transfer functions, wave in 0^o direction gives the highest excitation in surge, heave and pitch, while the excitation for sway, roll and pitch is zero due to the symmetry of geometry. Figure 4.4 shows that the amplitude and phase angle of excitation force or moment of unit wave elevation in surge, heave and pitch, when wave is in 0^o direction. The maximum excitation forces of surge and heave are 180^o out of phase with the wave elevation. The maximum excitation forces of pitch is 110^o out of phase. The wave in 0^o direction is of importance, since it gives the largest excitation to the pitch motion. The pitch motion is very relevant to the fore-aft bending moment.

Figure 4.3 plots the frequency dependent added mass and radiation damping. It can be observed that the added mass and damping of yaw motion are much larger. The added mass and damping coefficient of surge nearly equal to that of sway. It is the same with pitch and roll. There is the coupling between surge and pitch, also between sway and roll. The added mass A_{15} is of the same amplitude with A_{24}, but they are 180 degree out of phase. The damping B_{15} and B_{24} also present the same regularity. The curves plotted coincides with that of the IEA report [22]. This proves that the rigid-floater model was set up correctly. The total added mass and damping from HydroD can be used for the analysis of the rigid floater in SIMO/RIFLEX.

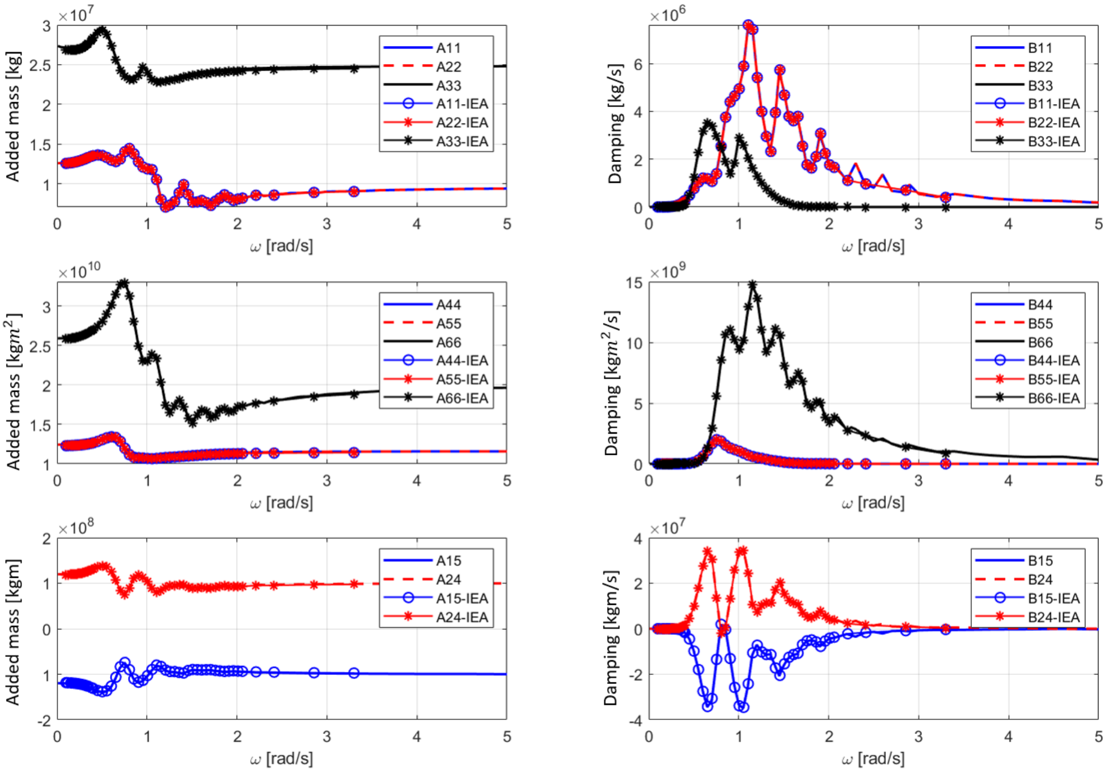

Figure 4.3: Added mass and radiation damping computed from HydroD.

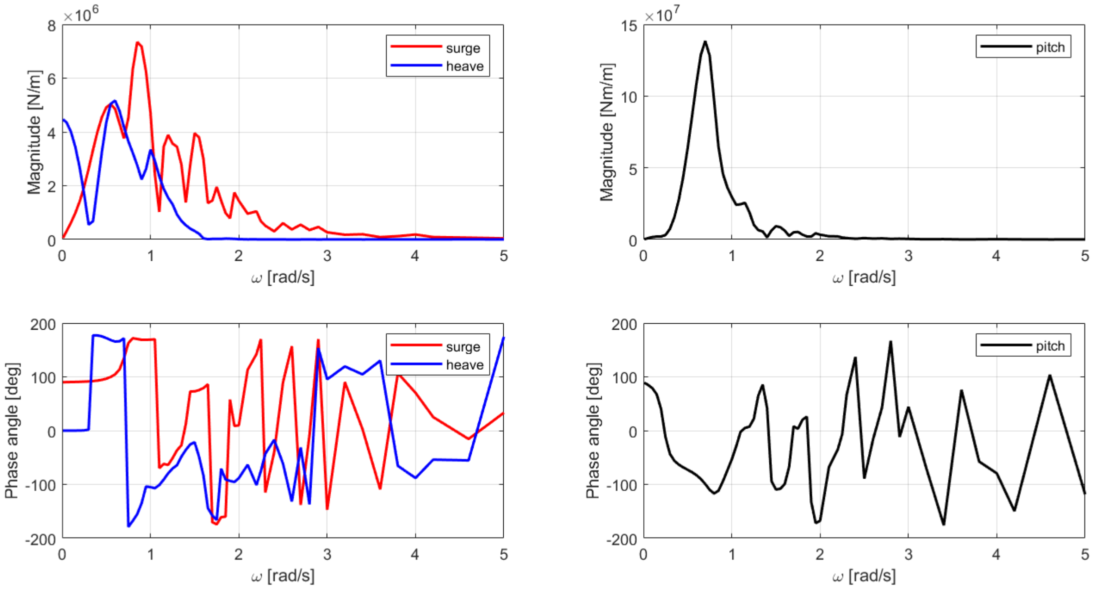

Figure 4.4: Excitation force amplitude and phase angle in surge, heave and pitch, in 0^o wave direction.

Based on the result in HydroD, the added mass of infinite frequency can be written as Equation 4.1.1. This is the parameter in the equilibrium in time domain. The unit of $A_{\infty[1-3,1-3]}$ is kg. The unit of unit of $A_{\infty[1-3,1-3]}$ is kgm^2, while that $A_{\infty[1-3,4-6]}$ and $A_{\infty[4-6,1-3]}$ is is kgm.

$$A_\infty = \begin{bmatrix} 9.54e6 & & & & -9.91e7 & \\ & 9.54e6 & & 9.91e7 & & \\ & & 2.46e7 & & & \\ & 9.91e7 & & 1.15e10 & & \\ -9.91e7 & & & & 1.15e10 & \\ & & & & & 2e10 \end{bmatrix} \begin{bmatrix} kg \\ kg \\ kg \\ kgm \\ kgm \\ kgm \end{bmatrix} \begin{bmatrix} 1 \\ 1 \\ 1 \\ m \\ m \\ m \end{bmatrix}^T \tag{4.1.1}$$

The frequency dependent potential damping and added mass are calculated utilizing the retardation function introduced in Section 3.1.2. The quadratic damping matrix is taken from the IEA report [22], which is computed with CFD method. The unit of $B_{Q[1-3,1-3]}$ is kg/m, while that of $B_{Q[1-3,4-6]}$ is kgm, and unit of $B_{Q[4-6,1-3]}$ is kg. The unit of $B_{Q[4-6,4-6]}$ is kgm.

$$B_Q = \begin{bmatrix} 9.23e5 & & & & -8.92e6 & \\ & 9.23e5 & & 8.92e6 & & \\ & & 2.3e6 & & & \\ & 8.92e6 & & 1.68e10 & & \\ -8.92e6 & & & & 1.68e10 & \\ & & & & & 4.8e10 \end{bmatrix} \begin{bmatrix} kg/m \\ kg/m \\ kg/m \\ kg \\ kg \\ kg \end{bmatrix} \begin{bmatrix} 1 \\ 1 \\ 1 \\ m^2 \\ m^2 \\ m^2 \end{bmatrix}^T \tag{4.1.2}$$

The hydrostatic restoring force matrix is written as

$$C = \begin{bmatrix} 0 & & & & & \\ & 0 & & & & \\ & & 4.46e6 & & & \\ & & & 2.19e9 & & \\ & & & & 2.19e9 & \\ & & & & & 0 \end{bmatrix} \begin{bmatrix} N/m \\ N/m \\ N/m \\ N \\ N \\ N \end{bmatrix} \begin{bmatrix} 1 \\ 1 \\ 1 \\ m \\ m \\ m \end{bmatrix}^T \tag{4.1.3}$$

The unit of $C_{[1-3,1-3]}$ is N/m, while that of $C_{[1-3,4-6]}$ and $C_{[4-6,1-3]}$ is$N$. The unit of $C_{[4-6,4-6]}$ is Nm. Then the global motion of the platform with quadratic damping in timedomain can be written as

$$(M + A_\infty)\ddot{x}(t) + \int_{-\infty}^{\infty} k(t-\tau)\dot{x}(\tau)d\tau + B_Q\dot{x}(t)|\dot{x}(t)| + Cx(t) = f_{exc}(t) \tag{4.1.4}$$

The excitation here includes the force or moment transferred from tower.

4.1.3 Coupled Analysis Model - SIMO/RIFLEX

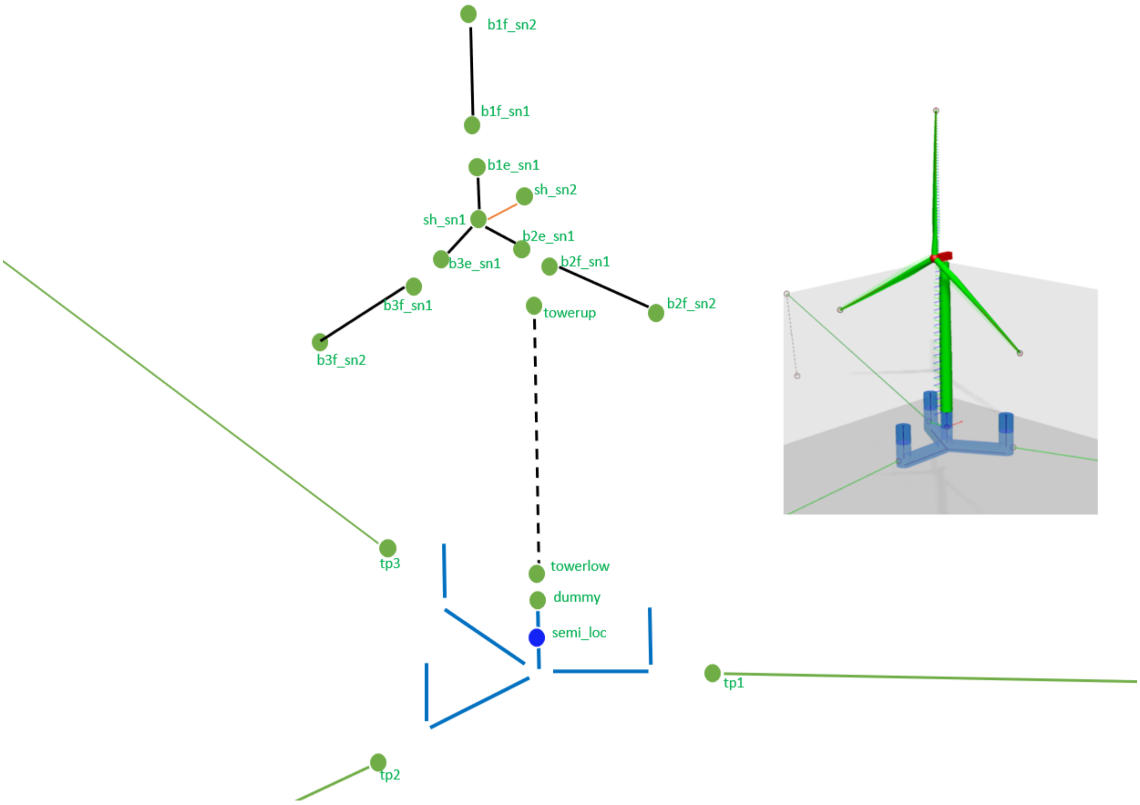

Figure 4.5: Illustration of node connection of the rigid-floater 15 MW wind turbine model in SIMA.

SIMO/RIFLEX is the numerical tool used for the integrated time domain simulation, which is inside SIMA platform. SIMO is principally employed to describe the rigid-body motions. Hydrodynamic kinetic properties can be defined in SIMO body. RIFLEX provides the function of modeling beam or bar elements for dynamic analysis. Mooring lines, tower and blades of offshore wind systems are modeled in RIFLEX to capture the dynamic response of these slender elements. SIMO/RIFLEX can model the floating wind turbine, where the floater is modeled as a SIMO body and the mooring lines, tower and blades are modeled as flexible beams. The connections of different components are shown in Figure 4.5.

4.2 Test of Rigid-floater Model

4.2.1 Constant Wind Test

The constant wind test is to check the performance of the wind turbine and the controller. The relevant results are integrated in Figure 4.6.

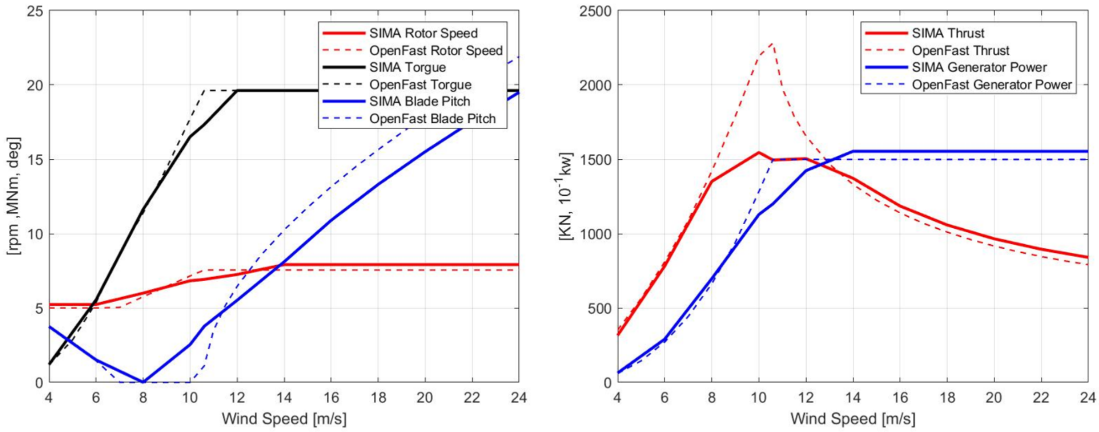

Figure 4.6: Rotor Speed, Torque, Blade Pitch, Generator power and Thrust Force of Constant Wind Test.

The wind speed ranges from 4m/s to 24m/s with the bin size of 2m/s. In addition, the designed rated speed of 10.6m/s is also taken into the test. In Figure 4.6, the plotted results include the variation of rotor speed, torque, blade pitch, generator power and thrust force along wind speed is plotted .

In general, the SIMA results match the result from OpenFast in IEA report . After the turbine is rated, the rotor speed and torque reaches the maxima and levels out. It is the same with the power generated, since the power is proportional to the torque and rotor speed. The blade pitch angle gets increased along with the increase of wind speed due to the control strategy. There is a obvious difference between the results from SIMA and OpenFast. The thrust force is clipped due to 'peak shaving'. This is done by the controller in order to reduce the peak load on the rotor and substructure in case of larger wind turbines. This is expected based on the controller file used.

4.2.2 Decay Test

The decay test is one way to estimate the natural period, linear and quadratic damping coefficients. To conduct the decay test, an impulse should be added on the body for a period of time and then get removed. After removing the impulse, the body will oscillate to perform the free decay motion. The 6-DOF free decay motions are shown in the Figure 4.7.

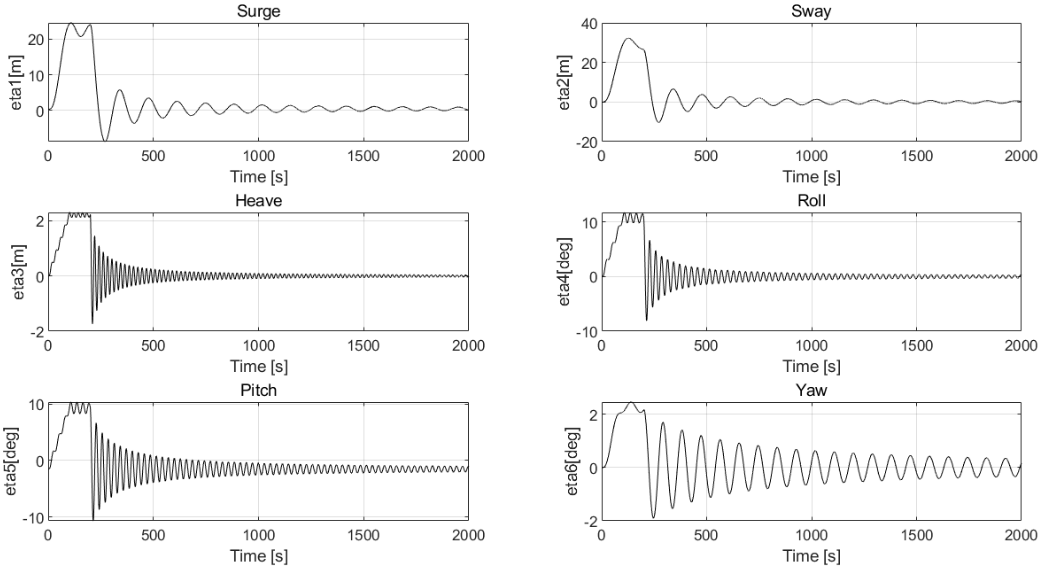

Figure 4.7: Free decay of six degree of freedom.

The PQ method is applied to find the damping coefficients. The equation of the free decay motion can be written as

$$m\ddot{x} + b_1\dot{x} + b_2|\dot{x}|\dot{x} + kx = 0 \tag{4.2.1}$$

b_1 and b_2 represents the coefficients or linear and quadratic damping respectively.

After removing the impulse, the damping force works to reduce the oscillation. The kinetic energy loss can be expressed by the potential energy difference between the peaks of the motion, where the kinetic energy is transformed into potential energy.

$$\Delta U_i = \frac{1}{2}kx_i^2 - \frac{1}{2}kx_{i+1}^2 = \frac{1}{2}k(x_i + x_{i+1})(x_i - x_{i+1}) = \frac{1}{2}k(\overline{x_i})(x_i - x_{i+1}) \tag{4.2.2}$$

The work done by the damping force in one cycle can be expressed as the integration along time.

$$W_i = \int_{t_i}^{t_{i+1}} (b_1\dot{x} + b_2|\dot{x}|\dot{x})\dot{x}dt \tag{4.2.3}$$

The motion and velocity can be expressed as

$$\begin{aligned} x &= \overline{x_i}\cos(\omega t + \epsilon) \\ \dot{x} &= -\omega\overline{x_i}\sin(\omega t + \epsilon) \end{aligned} \tag{4.2.4}$$

The total work of the damping force will be equal to the total loss of the kinetic energy of the system. The $W_i = \Delta U_i$ can be written into

$$\frac{x_i - x_{i+1}}{\overline{x_i}} = \frac{\omega\pi}{k} b_1 + \frac{8\omega^2}{3k} b_2 \overline{x_i} \tag{4.2.5}$$

The equation gives a linear relation ship between $\frac{x_i - x_{i+1}}{\overline{x_i}}$ and $\overline{x_i}$. The equation can be written as

$$\frac{x_i - x_{i+1}}{\overline{x_i}} = P + Q\overline{x_i} \tag{4.2.6}$$

The P and Q can be estimated through the linear regression of the data points ($\overline{x_i}$, $\frac{x_i - x_{i+1}}{\overline{x_i}}$). With the P and Q found by linear regression, the linear and quadratic damping coefficient can be estimated. The P is the y-intercept and the Q is the slope of the fitted straight line, as shown in Figure 4.8. The result of the linear regression actually is affected by the selection of the set of data points. To give a more accurate estimation, the former part of the decay motions are selected where the work of damping is more significant.

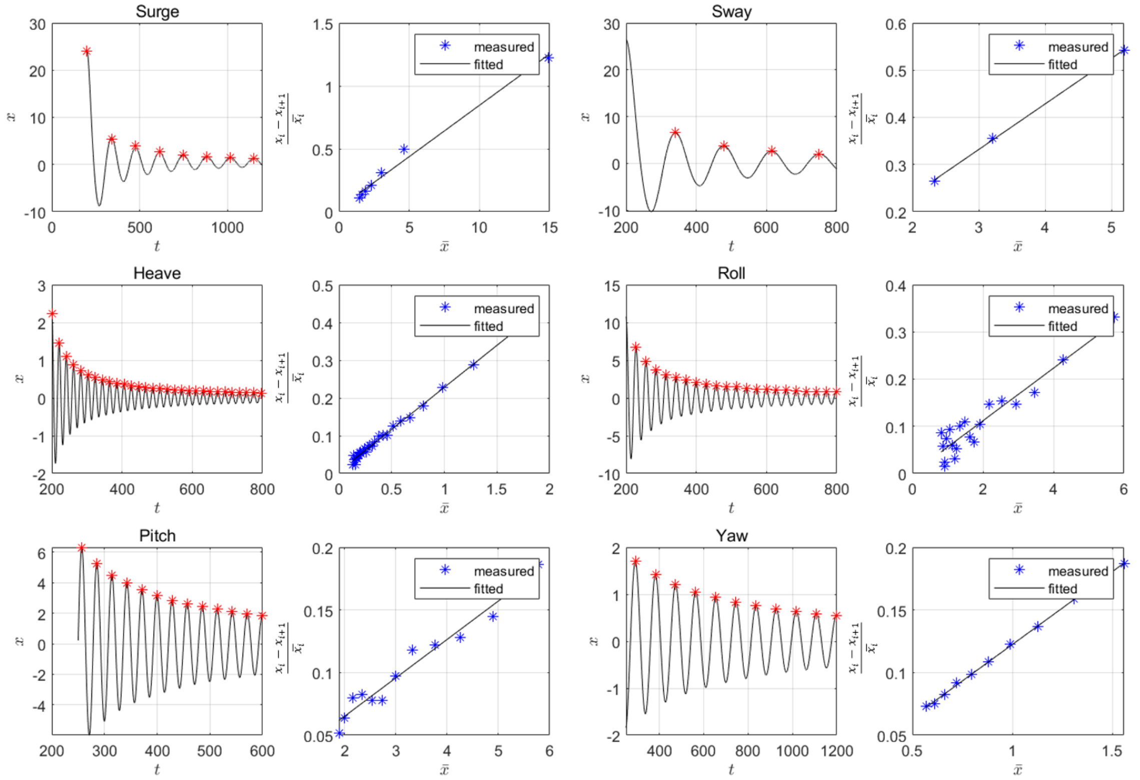

Figure 4.8: Maxima counting and linear regression to get the P&Q values.

The damping coefficients obtained from the PQ analysis are listed in Table 4.1. Compared with the hydrodynamic damping of the floater, it can be noticed that there is the difference from the damping coefficients estimated through PQ analysis. This means the hydrodynamic load on the floater only contributes to part of the damping. The upper structure and mooring system also provide the damping. Also, the quadratic damping contributes most to the total damping of the entire system.

Mode	Linear damping b1	Quadratic damping b2
Surge	$1.80E+04\ [kg/s^2]$	$1.30E+06\ [kg/m]$
Sway	$2.00E+04\ [kg/s^2]$	$1.20E+06\ [kg/m]$
Heave	$2.40E+04\ [kg/s^2]$	$3.90E+06\ [kg/m]$
Roll	$1.30E+06\ [kgm^2/s^2]$	$1.12E+09\ [kgm]$
Pitch	$1.50E+06\ [kgm^2/s^2]$	$7.01E+08\ [kgm]$
Yaw	$6.47E+06\ [kgm^2/s^2]$	$2.12E+09\ [kgm]$

Table 4.1: Damping coefficients estimated from PQ analysis

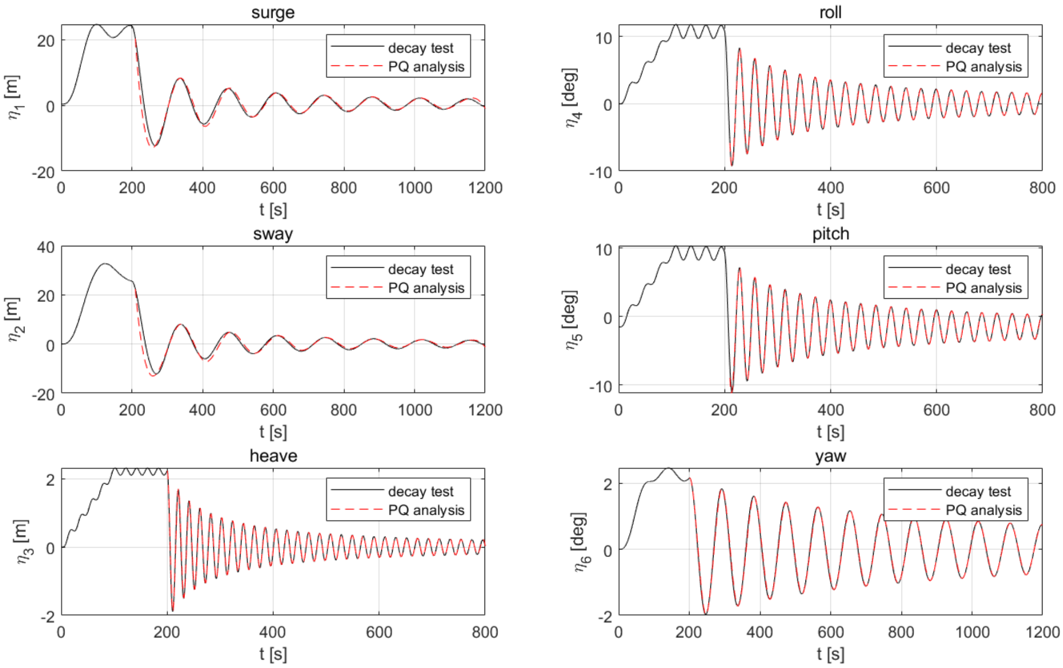

Figure 4.9: Free decay of six degrees of freedom with re-mapped PQ analysis result.

The Figure 4.9 shows the remapped decay motions of 6 DOFs. It can be observed that the remapped curves fit the original curves well. This means the data fitting is quite accurate. The Table 4.2 compares the damped natural frequency calculated in the decay test and that given in IEA report [22]. The results match each other. This verifies that the model of the rigid body is correctly built up in the SIMO/RIFLEX code.

	Natural frequency [HZ]	
Mode	**IEA report**	**SIMA**
Surge	0.007	0.0074
Sway	0.007	0.0073
Heave	0.049	0.0504
Roll	0.036	0.0367
Pitch	0.036	0.0367
Yaw	0.011	0.011

Table 4.2: Damped natural frequencies of 6 DOFs

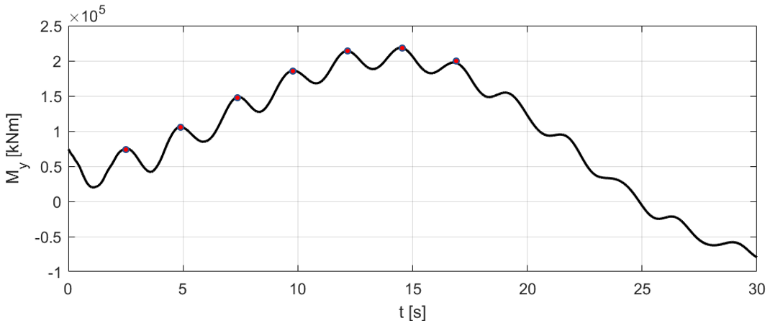

Figure 4.10: Bending moment variation at the beginning of pitch motion decay test.

After finding the natural frequency of motions. The natural frequency of fore-aft bending behavior should be found. This frequency can also be found from decay test. The initial 30 seconds of the bending moment history at tower base is plotted in Figure 4.10 to find the natural period of fore-aft bending behavior of the tower. The natural period can be found through counting the peaks, and the natural period is approximately 2.4 s, which is slightly longer than value given in IEA report.

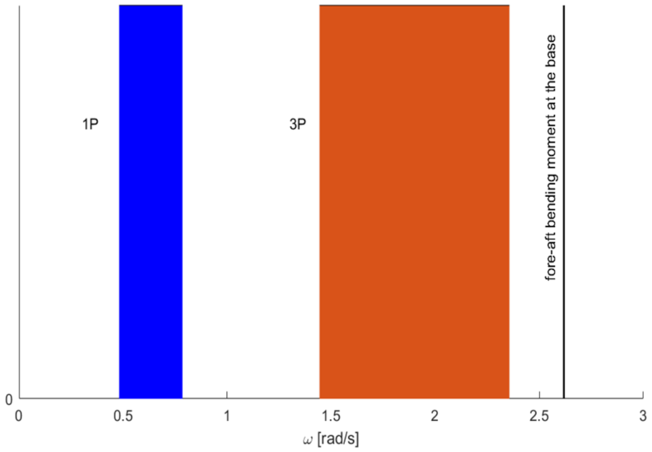

Figure 4.11: Frequency plotting of 1P, 3P and fore-aft bending frequency.

The Figure 4.11 gives the fore-aft bending frequency compared to the 1P and 3P frequencies. The fore-aft bending frequency is out of the range of both 1P and 3P. This result coincides with the description in IEA report [22]. The result also indicates the design is a stiff-stiff design.

4.2.3 Static Position

Due to that the mass of the turbine is not located at $x = 0$ and the rigid floater assumes the mass distribution of floater is uniform, there will be an initial pitch angle. Two initial boundary conditions are applied to still water case. One is that the floater is free and stabilized after static analysis, and the other one is fixed and released at $t = 0$ in dynamic analysis. The Figure 4.12 gives the initial pitch angle is approximately $-1.5°$. The initial boundary condition of fixed floater has the pro of better convergence while there is a small disturbance .

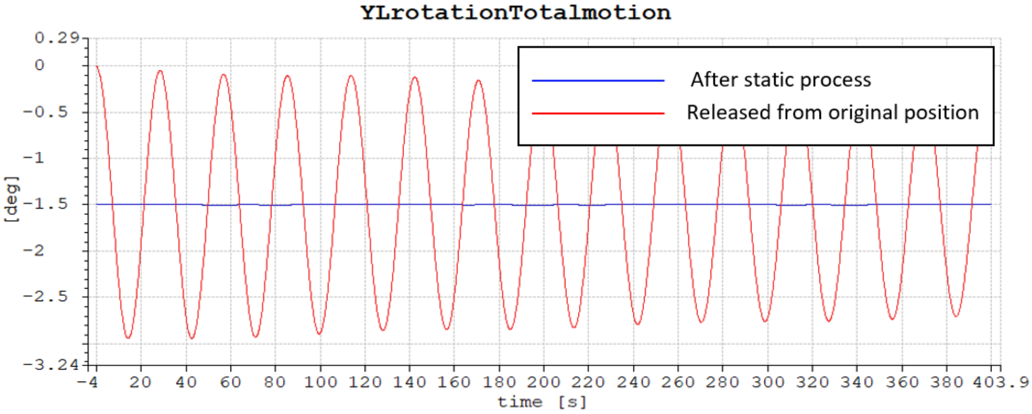

Figure 4.12: Pitch motion when the FOWT is positioned on still water.

4.2.4 Restoring Force Verification

The decay test of the numerical model in SIMO/RIFLEX presents kinetic characteristics which matches those given in IEA report. The added mass, damping coefficients computed are sufficiently accurate to describe the kinetic behavior of the platform, but the restoring matirx input is from the IEA report, as listed in Equation 4.1.3. This restoring matrix neglects the coupling effect between motions and should be examined through comparision to the result calculated using Equation 2.3.18. The C matrix integrated using Equation 2.3.18 is listed in Equation 4.2.7. The amplitude of C_{44} and C_{55} is slightly larger than the value in Equation 4.1.3. Also, there are surge-pitch, roll-sway and roll-yaw coupling terms highlighted in blue color. These terms are quite small compared with the diagonal terms but can contribute to the translational and rotational motions of the platform.

$$
\begin{aligned}
C^* = & \\
& \begin{bmatrix} & & 0.008 & -1.16e-9 & -659.13 & -5.59e-8 \\ & & -5.12e-9 & 710.16 & -1.12e-7 & -31.03 \\ 0.008 & -5.12e-9 & 4.47e6 & -5.96e-8 & 82.5 & \\ -1.16e-9 & 710.16 & -5.96e-8 & 2.21e9 & 8.82e-6 & -2.32e4 \\ -659.13 & -1.12e-7 & 82.5 & 8.8215e-6 & 2.21e9 & -2.38e-7 \\ -5.59e-8 & -31.03 & & -2.32e4 & -2.38e-7 & \end{bmatrix} \\
& * \begin{bmatrix} N/m & N/m & N/m & N & N & N \end{bmatrix}^T \\
& * \begin{bmatrix} 1 & 1 & 1 & m & m & m \end{bmatrix}
\end{aligned} \tag{4.2.7}
$$

To visualize the influence of the restoring matirx, decay tests with two different restoring matrix are proceeded. The decay-test result of the same model using different restoring matrix is presented in Figure 4.13. As shown in the plots, the sway motion is apparently weakened, while the roll motion is strengthened. As mentioned, the restoring matrix may influence the motions slightly when there is coupling effect. This coupled behavior more or less influences the motion in sway and roll. The influence is only on the amplitude of oscillation in the decay test, while the frequency is not affected. Although the difference is small, due to that the system is a highly non-linear system, slight difference can lead to remarkable variance in the result. The control of modeling accuracy is of significance and the C matrix calculated with Equation 2.3.18 should be put into practices.

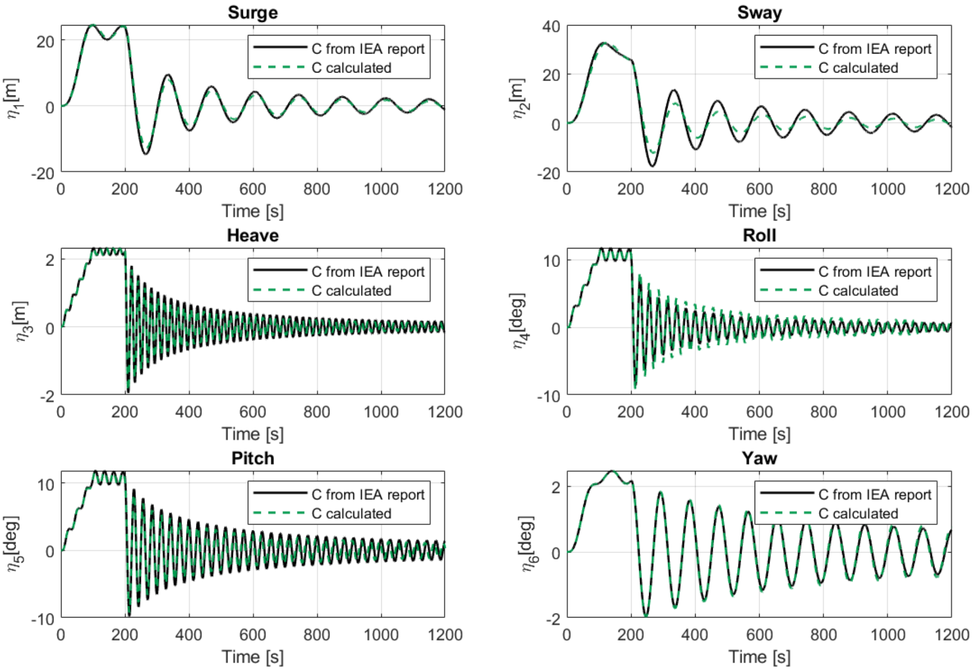

Figure 4.13: Decay test of rigid-floater model using restoring matrix from IEA report and self-developed program respectively.

Chapter 5

Novel Modeling of Flexible Floater Model

The conventional coupled analysis of FOWTs normally defines the floater as a rigid body. This assumption makes the numerical modeling easy to implement, but structural analysis of the floater cannot be carried out. To tackle this challenge, there should be an improvement in the fully-coupled time domain simulations. It is preferable to make improvement in already-existing code like SIMO/RIFLEX instead of coupling with some other finite element program to avoid increasing simulation time. Also, this preference can avoid the incompatibility with another solver. In other words, the goal is to maximize the utilization of functions in SIMO/RIFLEX. The proposed solution is that the floater can be cut into sub-bodies connected by beams, and cross sections on the connecting beams can output the dynamic response of force and moment. This idea can be exactly implemented in SIMO/RIFLEX without importing other numerical tools.

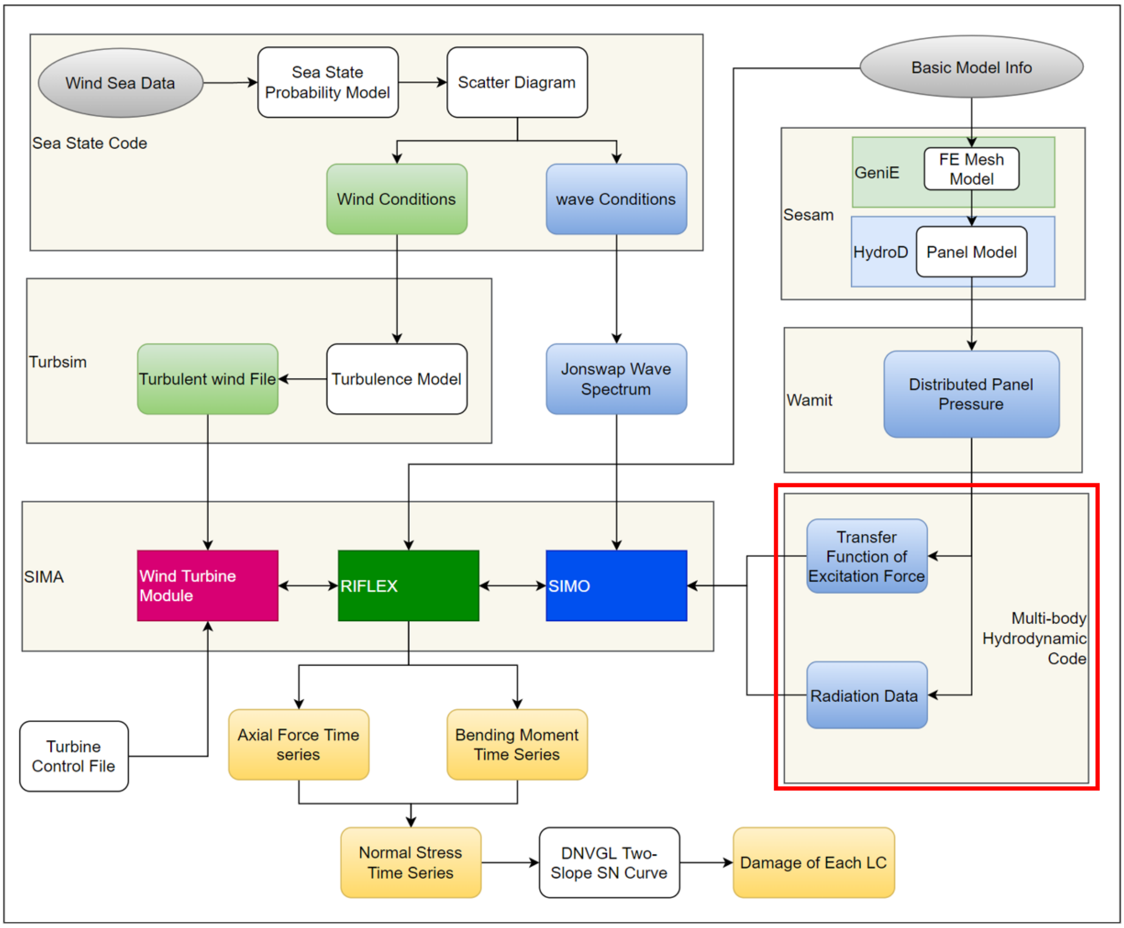

Figure 5.1: Working flow of flexible-floater numerical coupled model for fatigue analysis (based on time domain simulations).

With the rigid-floater model as a reference, the modeling of a multi-body numerical model is described by Figure 5.1. The main difference between Figure 5.1 and Figure 4.1 is that the radiation and diffraction coefficients of each predefined sub-body are obtained from integration of panel pressure using self-developed code. The different part is highlighted in a red block as shown in Figure 5.1. The kinetic properties of each body are described by the result from integration, while the bodies are connected by RIFLEX beam elements for the computation of sectional dynamic response.

To capture the reacting forces and moments on the floater, the floater is discretized first. Figure 5.2 demonstrates how the floater is discretized. As mentioned, to implement the redistribution of hydrodynamic force on each section of the multi-body model, WAMIT code is used to generate panel pressure. Dynamic pressure on each panel is integrated over each section by self-developed code. The body below the water surface (shown in the small figure in Figure 5.2) is used in the calculation inside WAMIT program and the output includes the coordinate information of panels and pressure on panels.

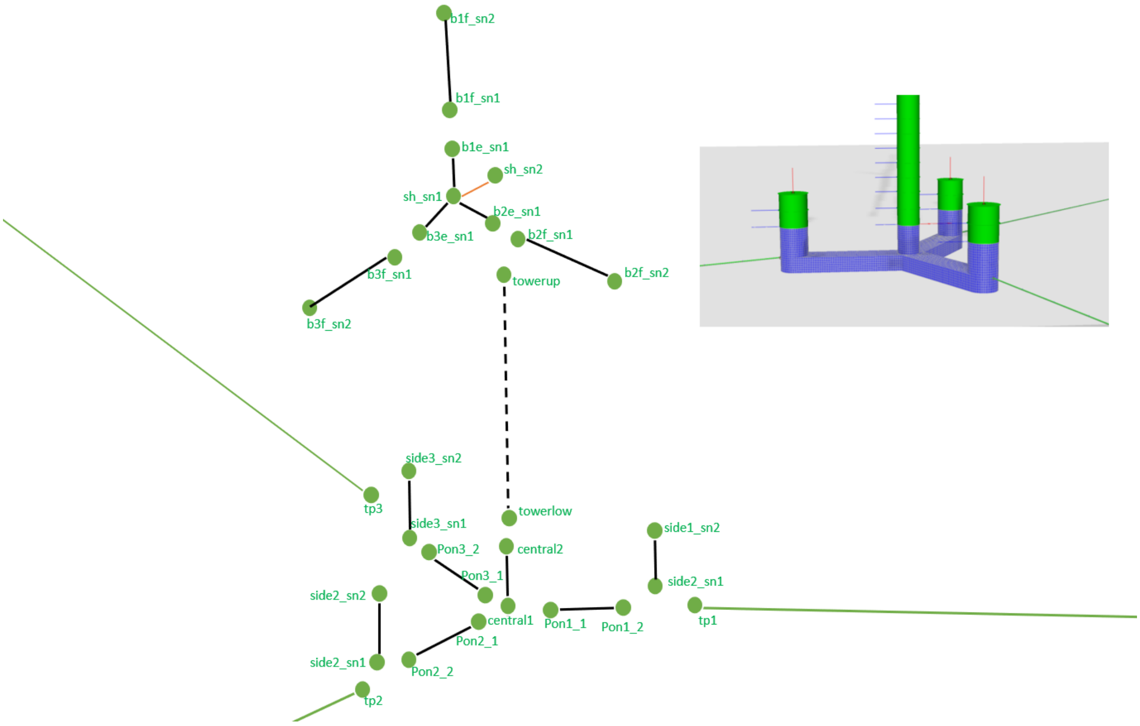

Figure 5.2: Illustration of node connection of the 15 MW wind turbine model in SIMA.

5.1 Modeling of Flexible Floater

Based on the description above, the work of establishing a flexible multi-body model in SIMO/RIFLEX can be divided into two parts. The first part is to recalculate the hydrodynamic coefficients including added mass, damping and restoring coefficients as well as transfer functions of excitation forces. The second part of work is to input the hydrodynamic terms to the model in SIMO/RIFLEX code and connect those sub-bodies with beam elements. As required, the newly-built model should present nearly the same hydrodynamic performance as the rigid-floater model.

5.1.1 Body Division & Hydrodynamic Coefficients of Sub-Bodies

Before the recalculation of hydrodynamic coefficients, the floater should be divided. In substance, body division means that coordinate range of sub-bodies is confirmed. If the coordinate of a panel is within the range, the panel pressure is integrated over that range. The floater can be divided into 4 columns and 3 pontoons as shown in Figure 5.3 .

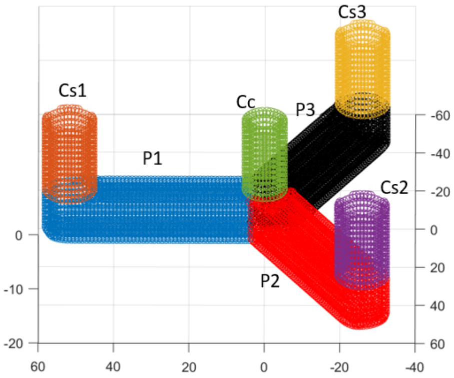

Figure 5.3: Illustration of floater divided into 7 parts.

To capture the dynamic response at the columns and pontoons, the columns and pontoons can be further divided. Figure 5.4 demonstrates how the columns and pontoons are divided into sections. Pressure on panels over each section is integrated to compute radiation and diffraction coefficients.

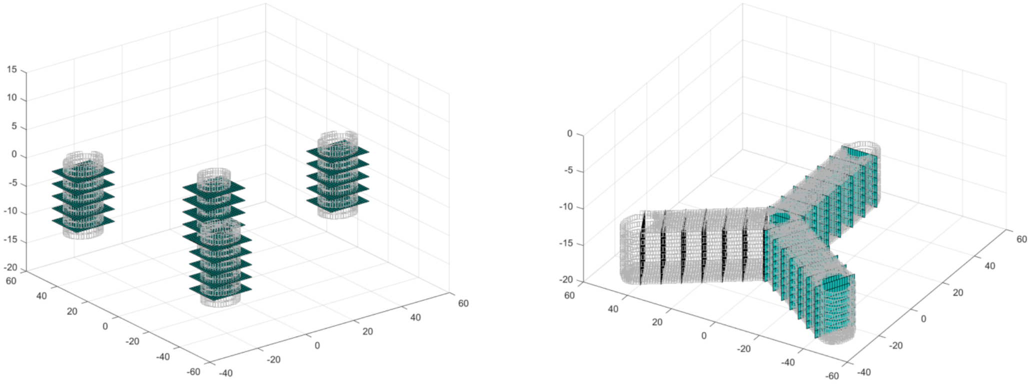

Figure 5.4: Illustration of how columns and pontoons are cut into sections.

Figure 5.5 and Figure 5.6 examine which part of the floater contributes most to added mass and damping. The 7 main components of the floater (4 columns and 3 pontoons) are colored in the 3D geometry plot in Figure 5.5 and Figure 5.6. The colors on the body correspond to the color of curves in other three subplots.

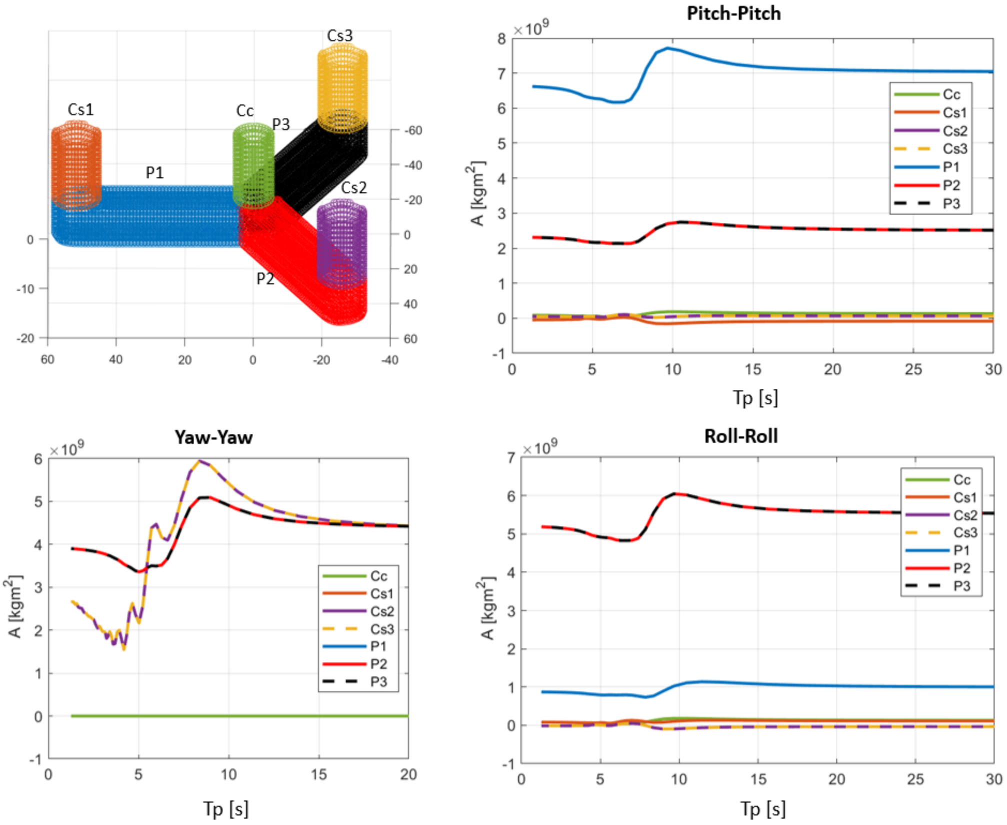

Figure 5.5: Comparison of added mass (A_{55}, A_{44} and A_{66} of different parts of the floater).

For the three modes of rotational motion, the total added mass is dominated by the contribution of pontoons. The pontoon NO.1 is the one aligned with x-axis. It provides most of the added mass to pitch motions, while the other two pontoons produce large added mass to roll motions.

Figure 5.6 shows the corresponding damping coefficients in pitch-pitch, roll-roll and yaw-yaw mode respectively. The pontoons also contribute most to the damping in roll and pitch motions, while the side columns provide most of the yaw damping. This finding reminds that correctly modeling of pontoon is very important.

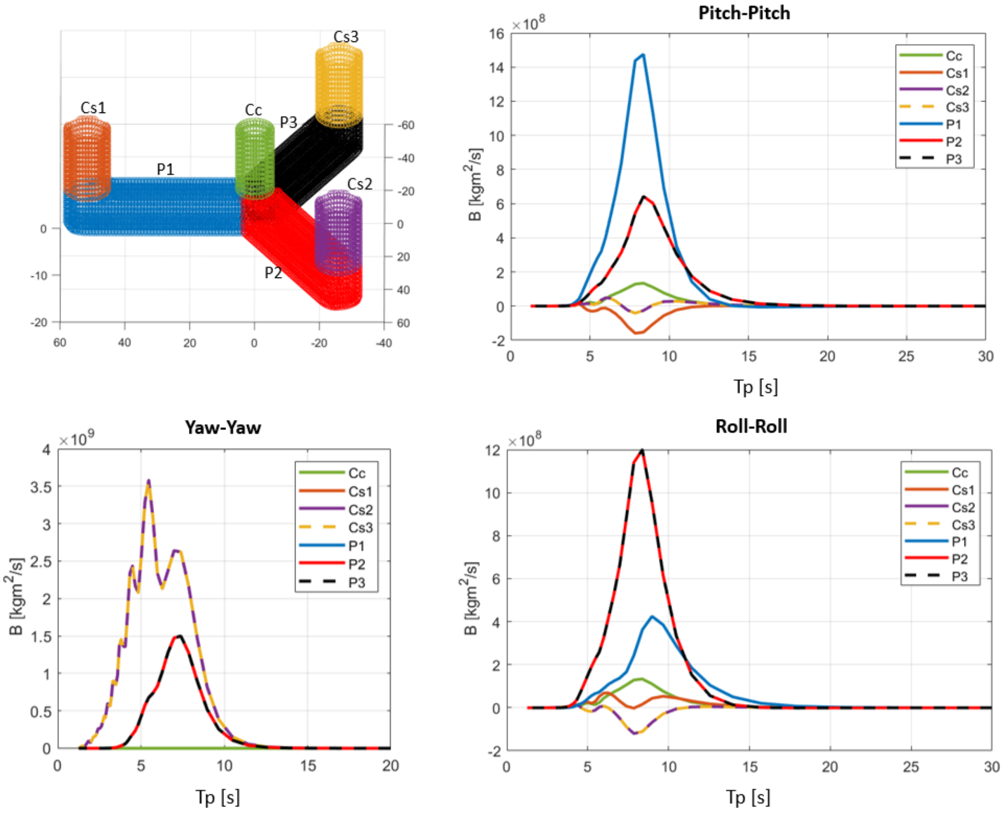

Figure 5.6: Comparison of damping coefficients (B_{55}, B_{44} and B_{66} of different parts of the floater).

Before modeling the multi-body floater in SIMA, the hydrodynamic coefficients of sub-bodies are summed up to be compared with the direct output from Wamit, where the floater is one body only.

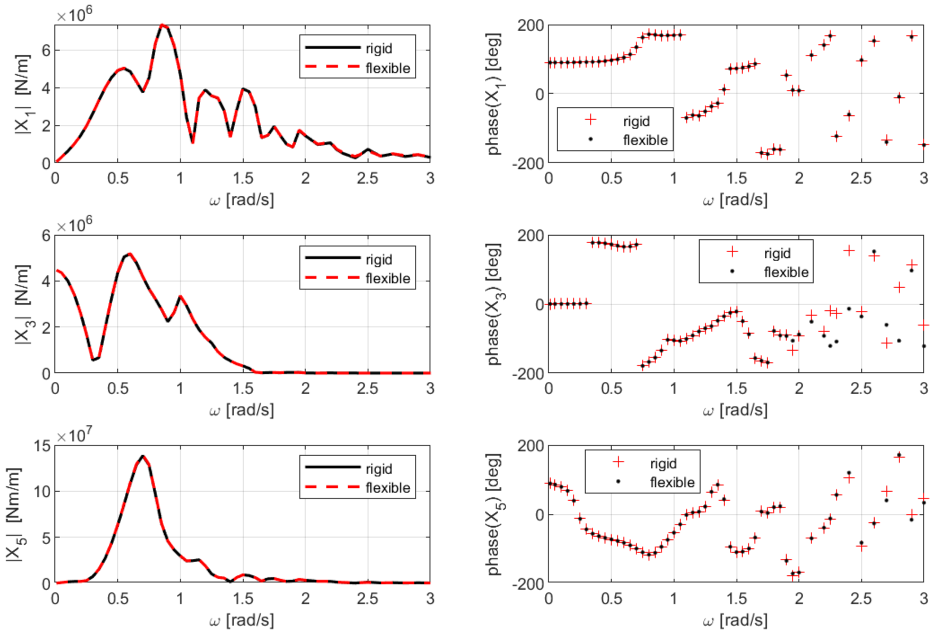

Figure 5.7: Comparison of transfer functions of 0-degree wave (the red curves represent the module of summation of sectional excitation transfer function, while the black curves represents the module of excitation transfer function from Wamit; the red scatters represent the phase of summation of sectional excitation transfer function, while the black scatters represent the phase of excitation transfer function from Wamit).

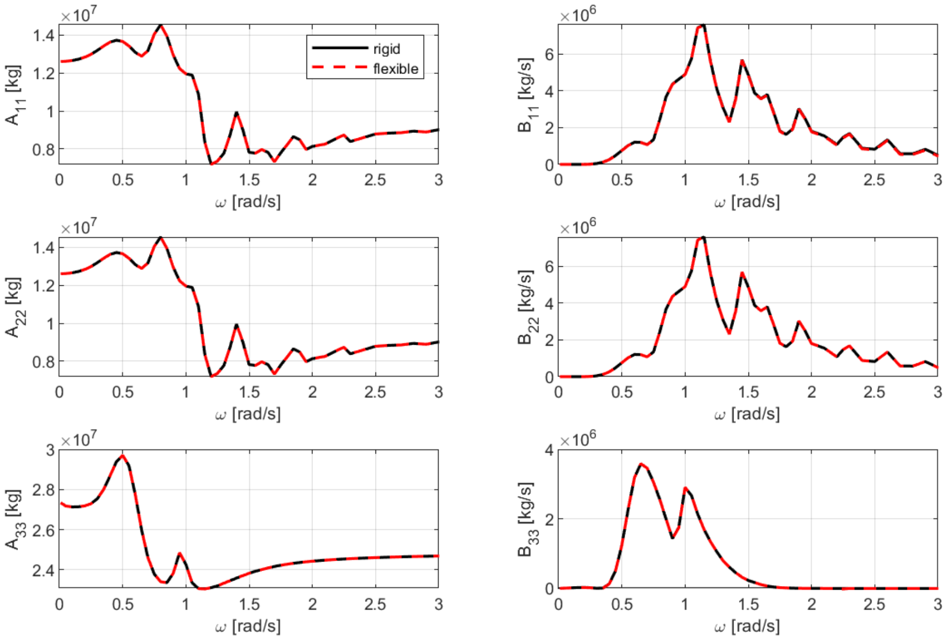

Figure 5.8: Comparison of translational added mass and damping components (the red curves represent the summation of sectional added mass and damping, while the black curves represents the output of total added mass and damping from Wamit).

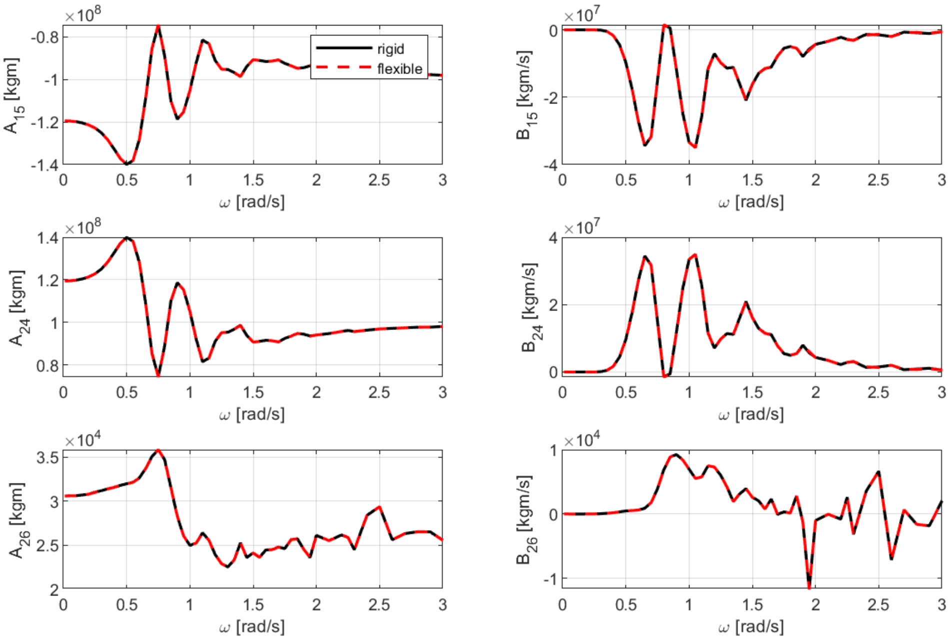

Figure 5.9: Comparison of of selected off-diagonal added mass and damping coefficients (the red curves represent the summation of sectional added mass and damping, while the black curves represents the output of total added mass and damping from Wamit).

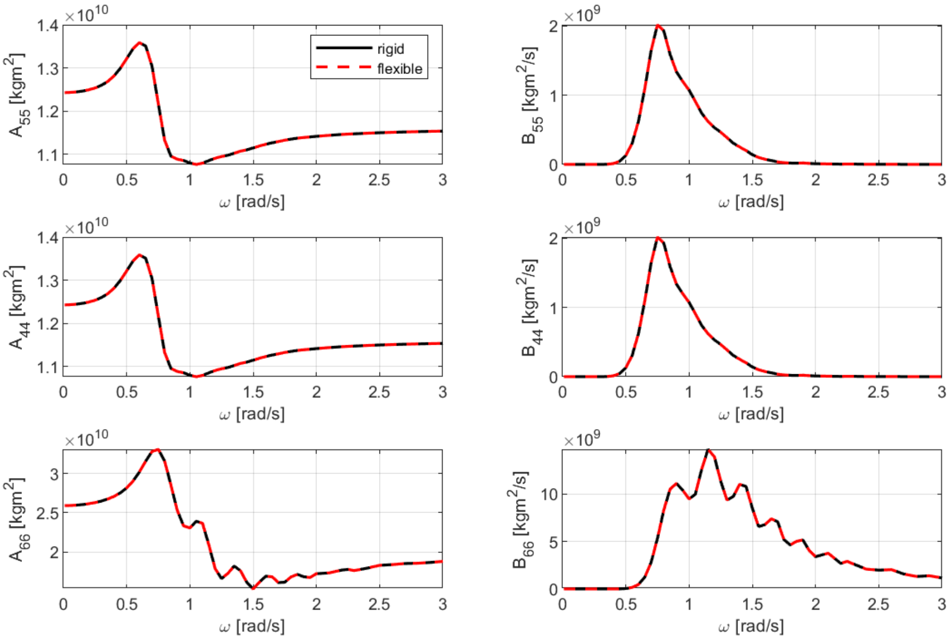

Figure 5.10: Comparison of diagonal added mass and damping components (the red curves represent the summation of sectional added mass and damping, while the black curves represents the output of total added mass and damping from Wamit).

Figure 5.7 compares the excitation transfer functions of wave from 0-degree direction. The amplitude of recalculated excitation transfer functions matches the result from Wamit perfectly, while there is small bias in the phase angle due to numerical errors. Figure 5.8, Figure 5.9 and Figure 5.10 compare the added mass and damping coefficients. The recalculated result matches the output of Wamit. The recalculated added mass, damping coefficients and transfer functions of excitation can be used in the modeling of multi-body floater.

5.1.2 Modeling in SIMO/RIFLEX

After the recalculation of distributed added mass, damping coefficients and transfer functions of excitation, the modeling work in SIMO/RIFLEX can be started. In the modeling tool, required inputs are not limited to added mass, damping coefficients and transfer functions of excitation. The inputs to sub-bodies should include:

- Added mass and damping coefficients
- Transfer functions of excitation force
- Restoring stiffness
- Buoyancy and buoyancy centers

- Mass, inertia and COGs

The modeling work is complicated, which can be simplified through utilizing functions in RIFLEX code. Different modeling strategies have been practiced and listed as follows.

- Simplified method 1 (S1):
  Input integrated translational terms of added mass, damping coefficients and transfer functions of excitation force. The stiffness introduced by hydro-static pressure and gravity is automatically computed from the mass and cross section properties of beam elements in RIFLEX.
- Simplified method 2 (S2):
  Input integrated added mass coefficients, damping coefficients and excitation transfer functions (both tranlational and rotational) to the SIMO bodies connected to beam nodes. The stiffness introduced by hydro-static pressure and gravity is automatically computed from the mass and cross section properties of beam elements in RIFLEX.
- Complete method (C1):
  Input integrated added mass coefficients, damping coefficients, excitation transfer functions, mass and restoring coefficients to the SIMO bodies, while RIFLEX beams are only used as connections to calculate internal force between sections.

The method S1 is the simplest modeling method, utilized by Svendsen [7], Hegseth [8] and Brevik [9], who studied a TLP model, a semi-submersible and two spar models respectively. This method worked well for TLP and spar model where the models are feature by one single column. However, in the practice to the semi-submersible model, this method produces unavoidable bias in rotational added mass and damping. This is due to that the added mass and damping of pontoons are not described correctly, when the added mass and damping caused by local rotations are neglected.

The method S2 is derived from method S1 and makes up the deficiencies of method S1. This method is capable of keeping the same added mass and damping. However, there exists the bias in rotational inertia and restoring stiffness, since these two terms are automatically computed in RIFLEX. This means that there is still improving space for SIMO/RIFLEX code to make method S2 applicable, but currently this scheme should be dropped. The detailed discussion of these two non-applicable methods is in Appendix D and will not be expanded here.

The finally determined scheme is to use method C1. For the method C1, the SIMO code is responsible for nearly all the inputs describing the kinetic characteristics, while the RIFLEX module is only used to connect different bodies defined in SIMO and transfer forces and moments. This method improves the control of consistency between multi-body model and rigid-floater model, but it increases the complexity of modeling. A small adjustment of the model like increasing sections requires modification of almost all the input files to ensure the similarity to the reference model.

In the practice of this thesis, from the perspective of both simplicity and practicality, one third of the structure is modeled into sub-bodies as shown in Figure 5.11. This simplicity is applicable since the work in this thesis focuses on the situation that wave and wind are aligned and come from 0-degree direction. Figure 5.11 illustrates how the sub-bodies are defined in SIMO and connected by beams defined in RIFLEX. The beam connections are given with quite large stiffness here. One reason is that the sub-bodies should not have very large relative motions. If there is very large relative motions between sub-bodies, the multi-body model cannot be compared with rigid-floater model. The kinetic and dynamic performance might be totally different. It can be guessed that the floater is perhaps quite flexible, but the study of flexibility should have experiment as reference. This will not be further expanded here.

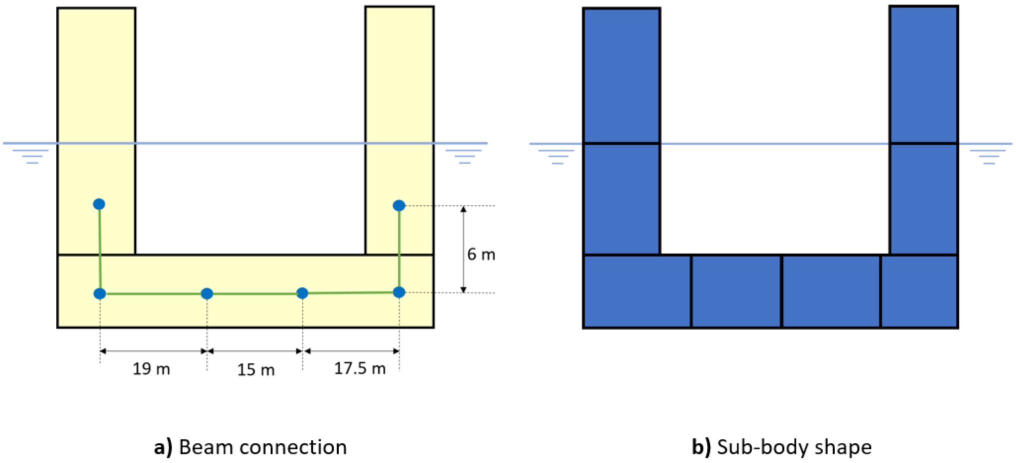

a) Beam connection

b) Sub-body shape

Figure 5.11: Sketched illustration of beam connections, sub-body shape and cross sections defined.

Figure 5.12 visualizes exactly the outlook of the flexible multi-body model in SIMA. The blue columns are the slender bodies used for adding viscous force, where the difference is that the slender lines are distributed to sub-bodies with the same drag coefficients given in rigid-body model.

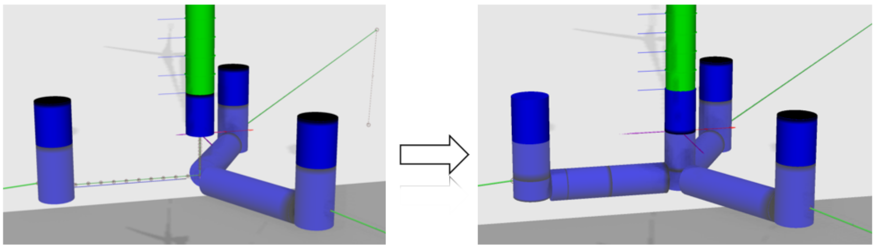

Figure 5.12: Flexible multi-body floater modeled in SIMA.

5.2 Test of Flexible-floater Model

5.2.1 Decay Test

Decay test is the first step to check the consistency with the rigid-floater model. As illustrated in Figure 5.13, the free decay test of the flexible multi-body model presents highly-consistent kinetic performance, compared to the rigid-floater model. This means that properties like mass, restoring stiffness, added mass and damping coefficients as well as damped natural period are under very strict control.

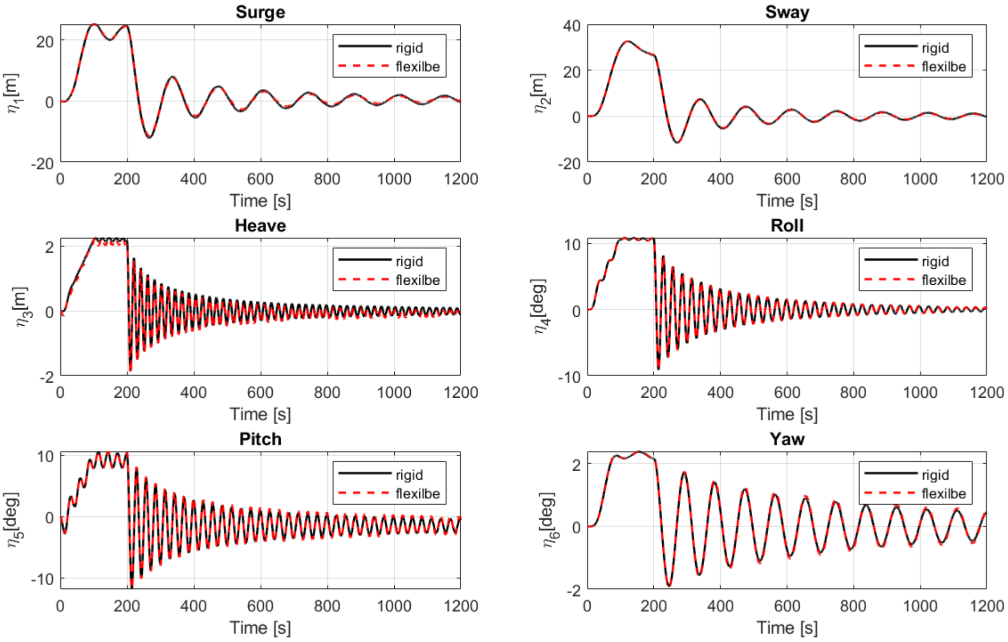

Figure 5.13: Decay test of flexible multi-body model compared with rigid-body model.

5.2.2 Irregular Wave Test

After decay test, the actual performance in wave sea should be compared. Irregular wave tests are proceeded before the turbulent wind is added to conduct fully-coupled simulations. The basic set of loading cases for fully-coupled time domain simulations are most-probable combinations of Hs and Tp under each Uw. Four representative irregular wave conditions are selected from that set and listed in Table 5.1. These waves are from the 0°. The simulations under these four wave conditions are accomplished to compare the motions of both the rigid-floater model and flexible-floater model.

	Hs [m]	**Tp [s]**
LC1	2.25	9.5
LC2	3.25	10.5
LC3	4.25	11.5
LC4	6.25	12.5

Table 5.1: Loading cases of irregular wave set.

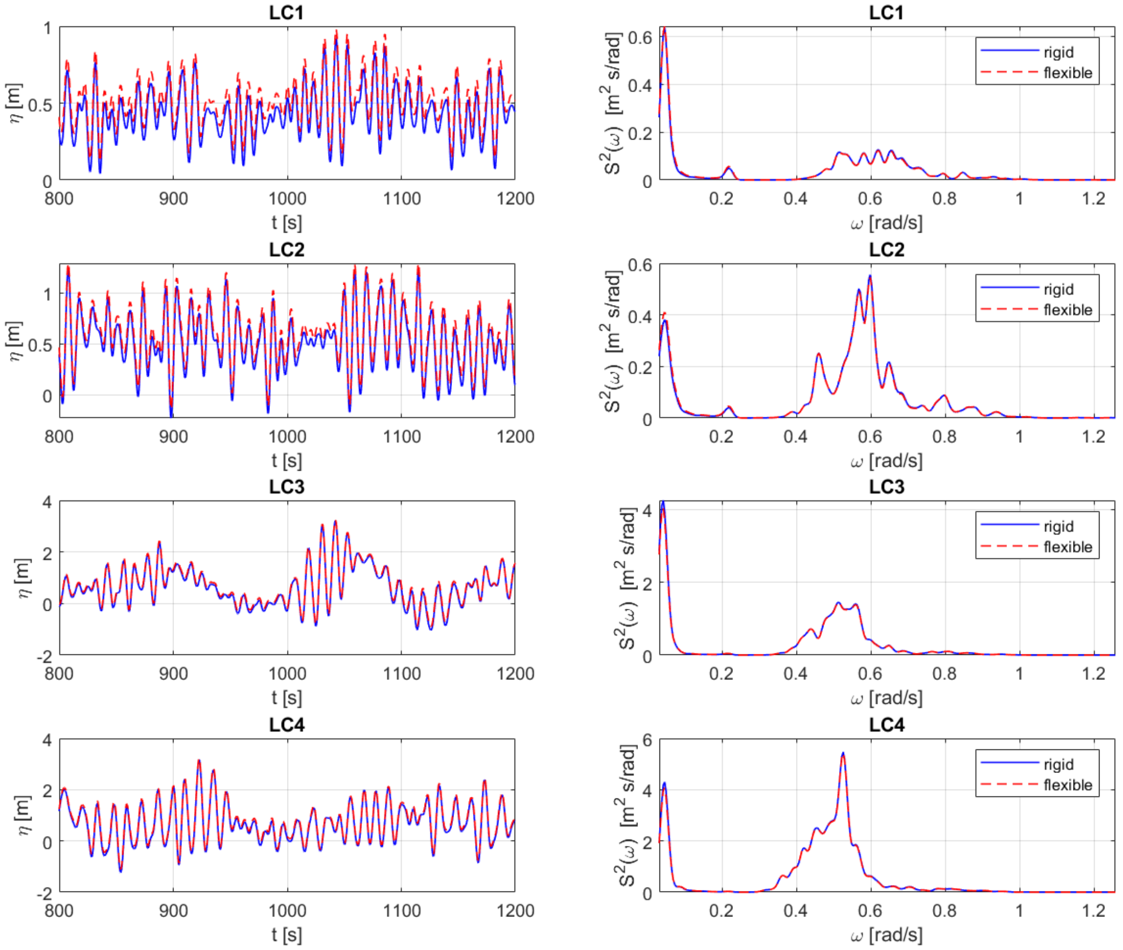

Figure 5.14: Surge motion comparison between rigid-floater model and flexible-floater model.

Principally, the surge, heave and pitch motions are compared, since these motions influences the the axial force and fore-aft bending moment at the tower base, especially when the wave and wind are aligned. The wave used in the simulations is given with the same random seed (realization of simulations). The comparison of motions in wave sea is to check the modeling consistency of the multi-body model compared with rigid model.

The standard of consistency in the wave test should be that the time series of two model generally coincides. Also, the frequency component and peaks in the power spectra should match. The zoomed-in time series and power spectra of surge, heave and pitch motions are given in Figure 5.15, Figure 5.15 and Figure 5.16 respectively.

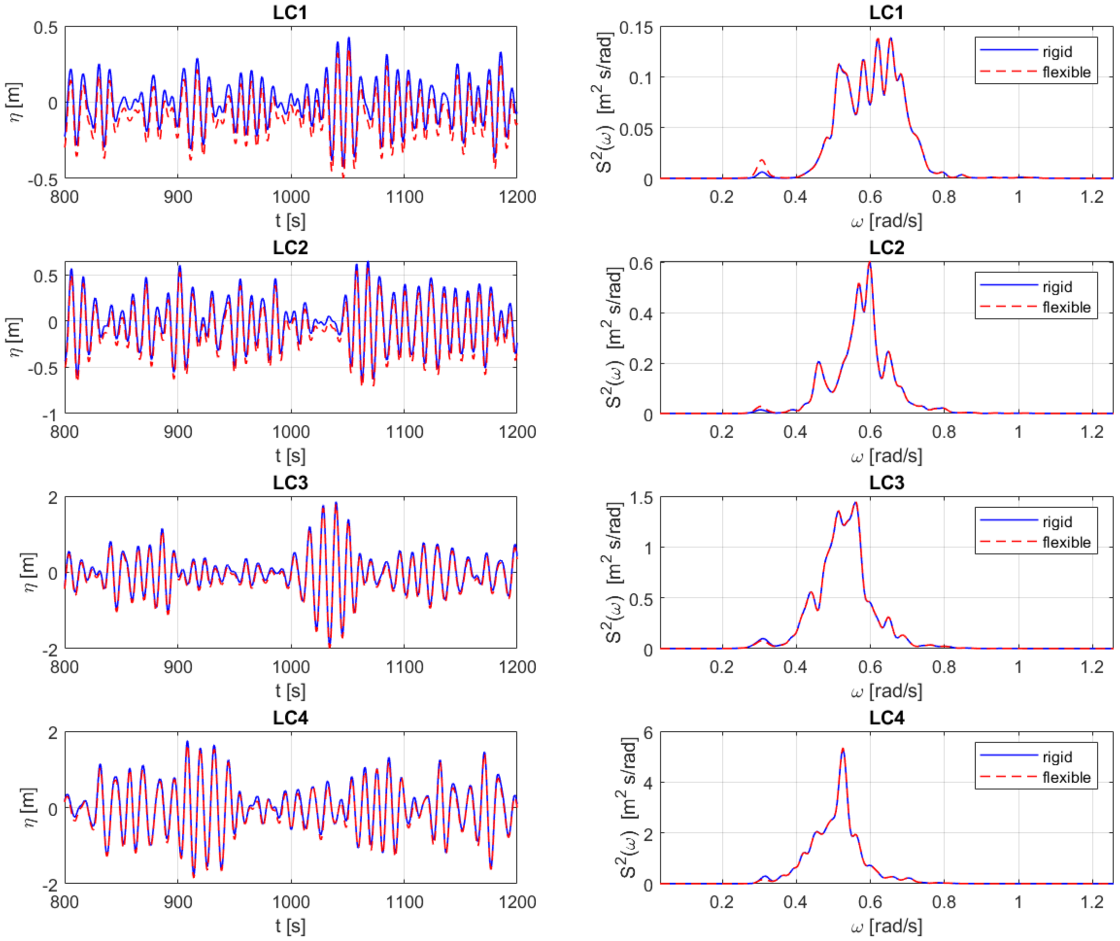

Figure 5.15: Heave motion comparison between rigid-floater model and flexible-floater model.

As shown in Figure 5.14 and Figure 5.15, for LC1 and LC2, there is a slight mean offset between the two time series. The mean offset means that the initial position at $t = 0$ has slight difference. The sight difference is very likely due to the numerical errors when the mass and hydro-static pressure are distributed. Another reason for the numerical error can be the change of numerical precision when data is transported from code to codes. But generally, the surge, heave and pitch motions of the flexible-floater model present the same trend as the rigid-floater model. The difference is negligible due to that it does not influence the frequency components in the power spectra.

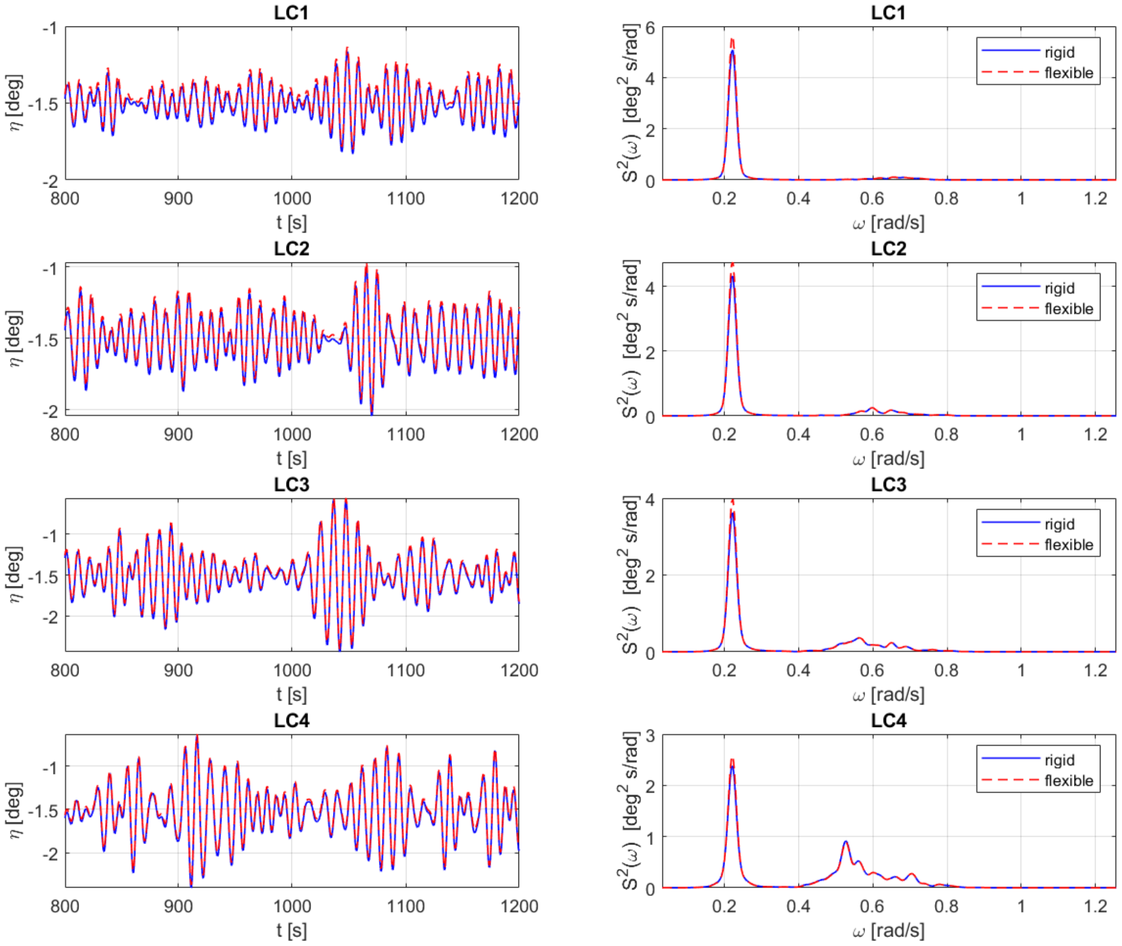

Figure 5.16: Pitch motion comparison between rigid-floater model and flexible-floater model.

5.2.3 Turbulent Wind Test

Turbulent wind test is also conducted to check if the dynamic response at certain cross sections is the same. The cross section that is compared is the tower base. The time series and power spectra of bending moment are compared to check the consistency in dynamic response. The standard of being consistent is still that the time series of two model generally coincides, and the frequency component and peaks in the power spectra should match.

As mentioned in the section of irregular wave test, most probable combinations of Hs and Tp under each Uw are selected to make up a set for the test of fully-coupled time domain simulations. The set of selected loading cases are listed in Table 5.2.

	Uw [m/s]	**Hs [m]**	**Tp [s]**
LC1	4	1.75	9.5
LC2	6	1.75	9.5
LC3	8	1.75	9.5
LC4	10	2.25	9.5
LC5	12	2.75	10.5
LC6	14	3.25	10.5
LC7	16	3.25	10.5
LC8	18	4.25	11.5
LC9	20	4.75	11.5

Table 5.2: Loading case of turbulent wind and irregular wave set

The zoomed-in time series of the fore-aft bending moment of two models are plotted in Figure 5.17. The two bending moment time series exactly match each other, which attests that the motion difference in the irregular wave test is tolerable. The slight bias in wave test has no significant influence to the dynamic response on the tower base section. The spectra of the bending moments are compared in Figure 5.18. The consistence in the power spectra of bending moment testifies the usability of the flexible multi-body model.

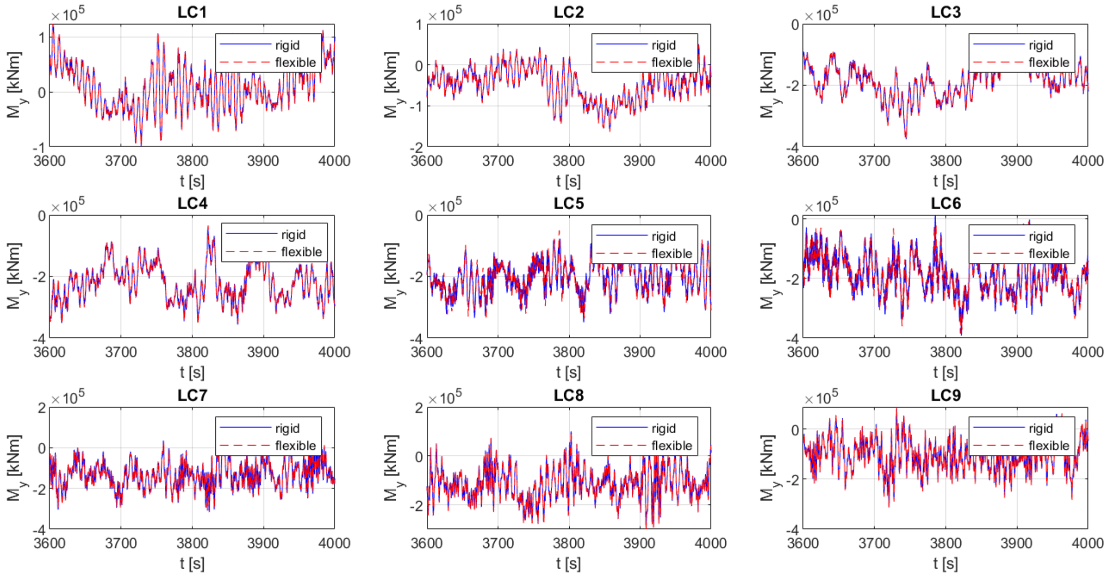

Figure 5.17: Time series of bending moment on tower base of rigid-floater model and flexible-floater model.

It should be noticed that the peak at wave frequency and pitch natural frequency ($\omega = 0.23\, rad/s$) gets enhanced from LC1 to LC9. These two frequencies stand out in the spectra of pitch motion in Figure 5.14. This points out that bending moment on tower has strong correlation with pitch motion. Also, when the mean wind speed is over rated speed, the frequency component at fore-aft bending frequency ($\omega = 2.5 - 2.6\, rad/s$) is noticeable. The fore-aft bending behavior is excited in these cases.

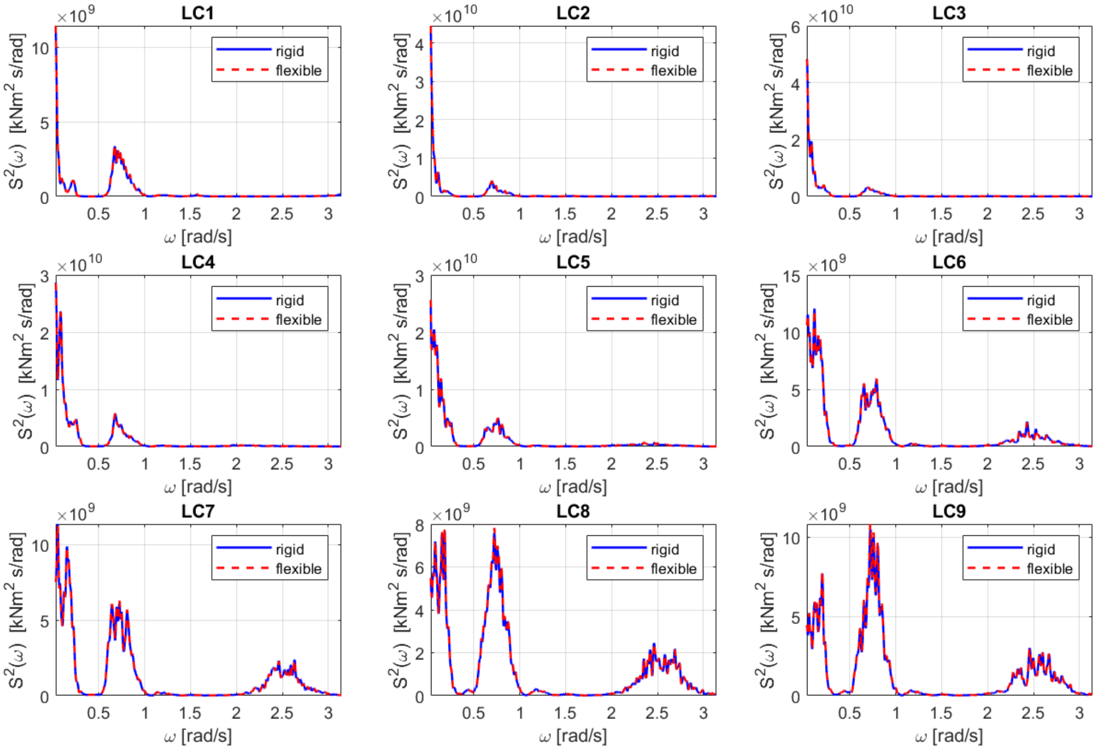

Figure 5.18: Spectra of bending moment on tower base of rigid-floater model and flexible-floater model.

Based on the results of this simulation set, the fatigue damage under each case can be estimated and compared. The fatigue damage under each loading case is benchmarked in Figure 5.19. The calculated fatigue damage between two models gives very close results to each other. There is apparently a certain trend that the fatigue damage increases with the wind speed. If those most probable combinations of Hs and Tp under each wind speed can be representative of the average of all the combinations under that wind speed, a fitted model to these cases can be used for prediction. This will be further discussed in chapter 6.

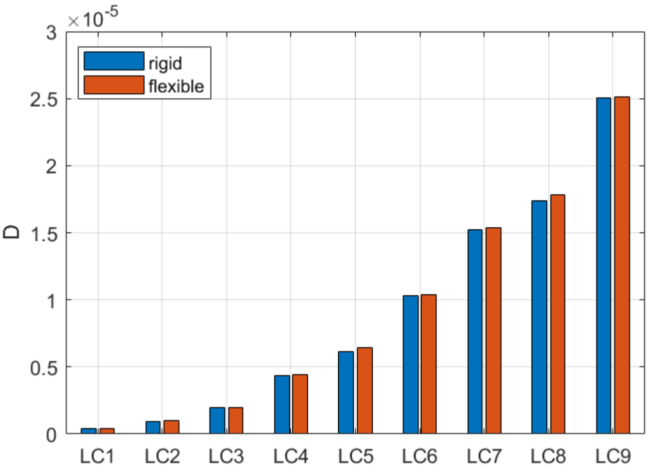

Figure 5.19: Fatigue damage comparison between rigid-floater model and flexible-floater model under nine loading cases.

5.3 Sectional Response on Floater Hull

Previously, one third of the floater is cut into sub-bodies to study the sectional response on the floater. Figure 5.20 gives information about the predefined cross sections which are employed to discuss the dynamic response. The color marked in Figure 5.20 corresponds to the plot color of the results in the lateral discussion of sectional response.

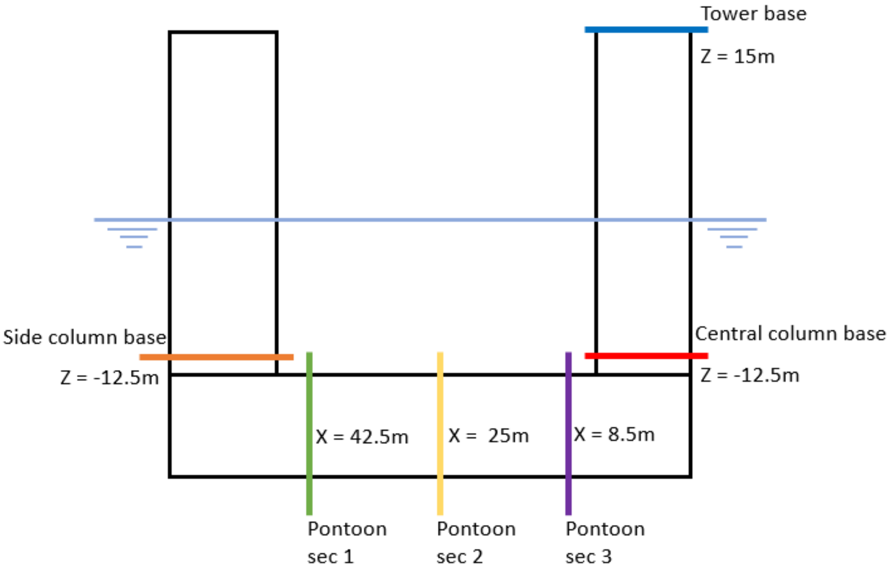

Figure 5.20: Sketched illustration of cross sections defined.

Since the connections between columns and pontoons are welded together, these connections are regarded as vulnerable due to stress concentration. For simplicity, the connections between columns and pontoons can be regarded as tubular joints. The column can be treated as a brace, and the pontoon can be counted as a chord. For the fatigue analysis, the response at two points close to the welding should be extracted, and the hot-spot stress is calculated. However, the detailed design parameters of the floater is not ensured, and it is rational to compare the sectional loads and estimate the fatigue damage. The work in this section aims at providing insight for further analysis to fatigue issue of floater hull.

5.3.1 Sectional Loads on Central Column

The original rigid-floater model only enables the capture of dynamic response at the tower base. But literally, more intensive response may occur to the central column base. This location undertakes the hydrodynamic loads directly, and there is very large bending moment induced by wind. It is very likely that this location undergoes severe fatigue failure, and the dynamic response of this location should be examined.

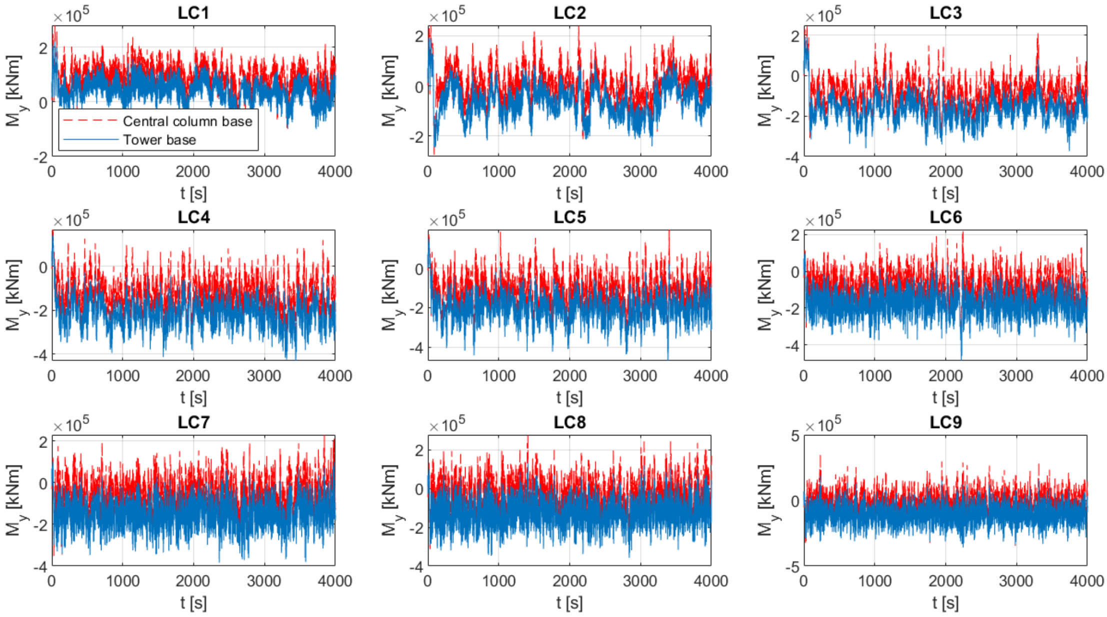

Figure 5.21: Time series comparison between bending moment at tower base and central column base.

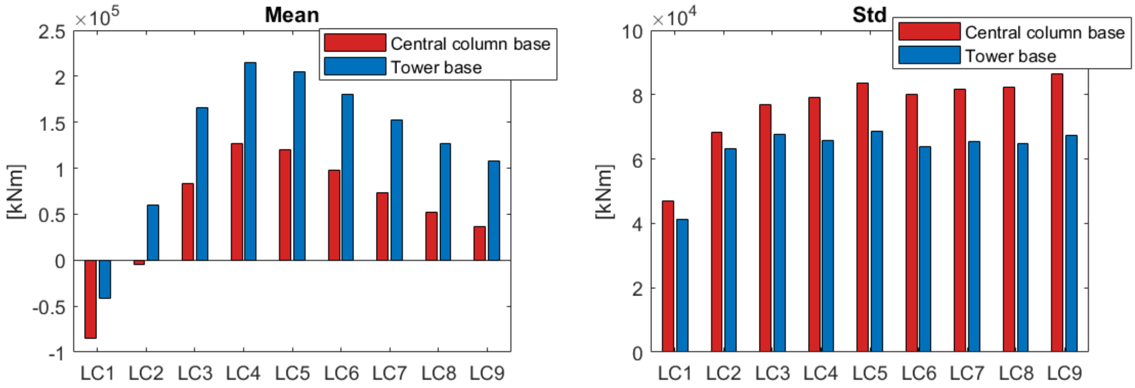

Figure 5.22: Mean and standard deviation of bending moment at tower base and central column base.

The time series of fore-aft bending moment at the tower base and central column base are plotted in Figure 5.21. The two curves present similar trend of vibration with a mean offset introduced by gravity. Figure 5.22 compares the mean and standard deviation of bending moment time sereis at tower base and central column base. The bending moment in negative direction at low wind speed cases is due to the initial pitch angle of the FOWT. The distribution of mean fore-aft bending moment generally follows the trend of thrust force depicted in Figure 4.6 as expected. The bar graph of standard deviation tells that the bending moment at central column base varies in a wider range. It can be guessed that the central column base will suffer from severer fatigue damage, if it is designed with the same plate thickness with tower base.

The time series in Figure 5.21 also shows that the proportion of wave-frequency components is higher as Uw and Hs are improved. This is reflected in Figure 5.23, where the shape of power spectra is close to each other. The pitch motion contributes to the fore-aft bending moment significantly. It can be guessed that the fatigue damage at the central column base is severe.

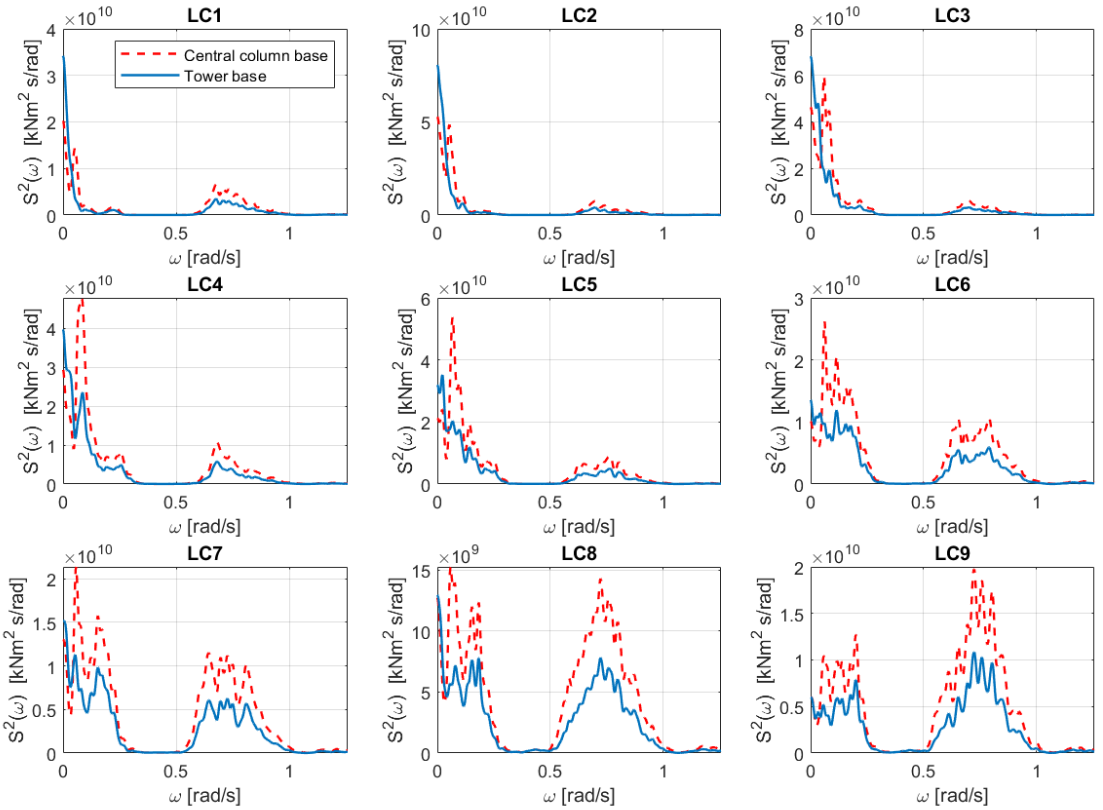

Figure 5.23: power spectra comparison between bending moment at tower base and central column base.

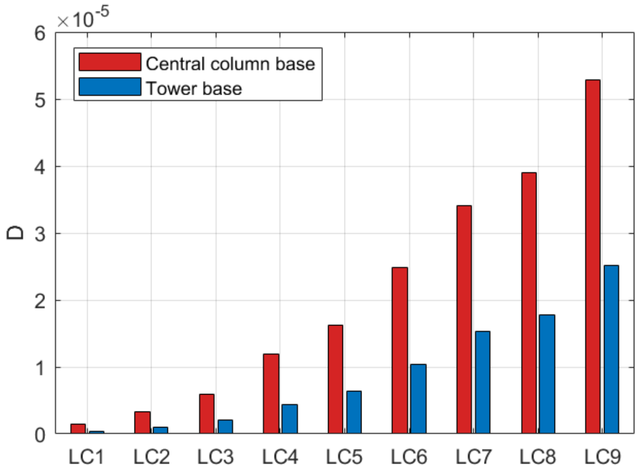

Figure 5.24: 1-hour fatigue damage at tower base and central column base.

The estimated 1-hour fatigue damage (D) at central column bottom under each loading case is benchmarked in Figure 5.24. The damage at central column base is approximately twice the damage at tower base. The fatigue damage of central column base is an estimated value, since the detailed design inside the column (including girders or stiffeners) is not confirmed. The value can merely function as a reference for further detailed analysis. This part of structure can be deemed as an extension of the tower, welded with the pontoons. The stress concentration around welding plus high load cycles make this location very dangerous. This warns that designers should be circumspect when designing the central column. Besides, Figure 5.24 tells that the distribution of the damage generally follows a similar trend to that of tower base. This regularity enables the utilization of the same technique as used in fatigue estimation at tower base.

5.3.2 Sectional Loads on Side Column

The central column is connected to the tower directly. The dynamic behavior at central column base presents similar characteristic compared to tower base. But when it comes to the side columns, the result might be very different. The side column and central column are connected by the pontoon in between. The bending moment related to pitch motions does not matter for the response on side columns. Instead, translational motions are important to this part of structure, since the mooring line is connected directly to the side columns.

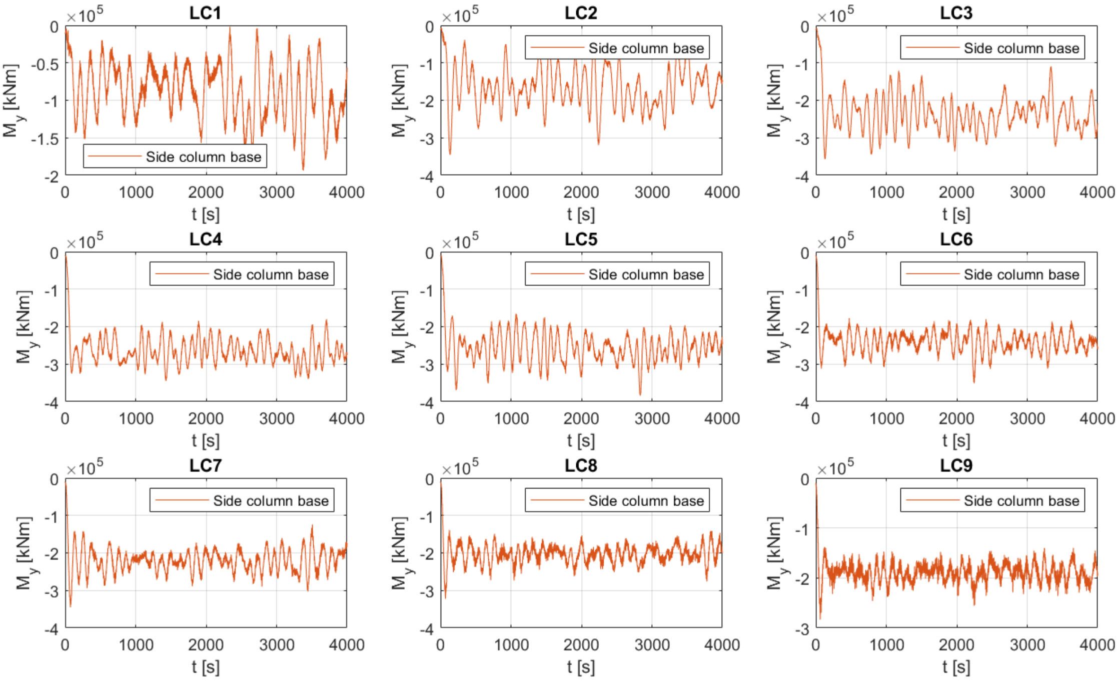

Figure 5.25: Time series of fore-aft bending moment at side column base.

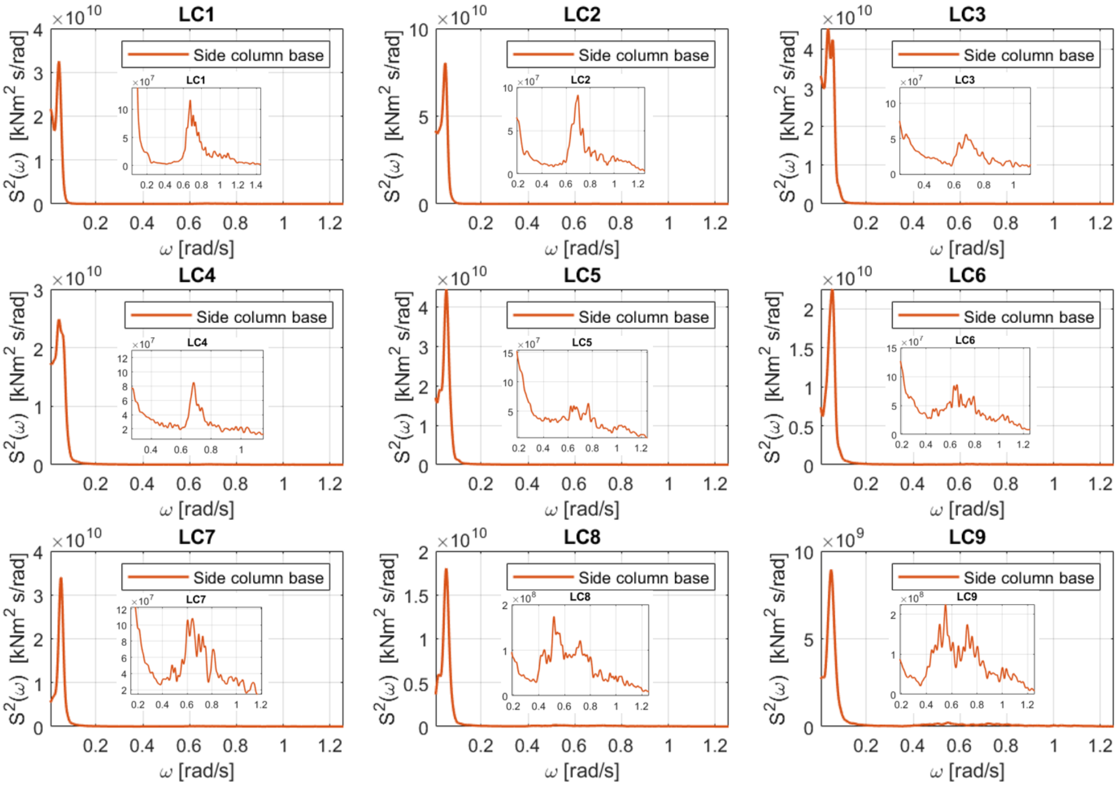

Figure 5.26: Power spectra of fore-aft bending moment at side column base.

The time series of the fore-aft bending moment at side column base is plotted in Figure 5.25 for a genral view of the dynamic response. Larger vibration is noticed in the loading case under rated wind speed. It can be observed that there is very high proportion of low-frequency components from the time series plots for the 9 loading cases. This is reflected in Figure 5.26, where the peaks are located at around surge motion natural frequency ($\omega = 0.044\, rad/s$). The amplitude of wave-frequency component is much lower for the case of side column. If zoomed in, the peak under wave frequency is not even $\frac{1}{1000}$ of that in the low-frequency range. The spectra plot of bending moment at side column base is very similar to spectra of stress in mooring lines. It can be confirmed that there is correlation between surge motions and dynamic response on the side column. The response on the side column is featured to be similar to that of mooring lines.

The bar graph of standard deviation in Figure 5.27 compares the mean and standard deviation under each loading case. The distribution of mean fore-aft bending moment generally follows the trend of thrust force depicted in Figure 4.6 as expected. The graph of standard deviation benchmarks the intensity of vibration. The standard deviations of bending moment under LC2 and LC3 are quite high. This is indirectly reflected in Figure 5.28, where the fatigue damage under LC2 and LC3 is much larger than that under other loading cases.

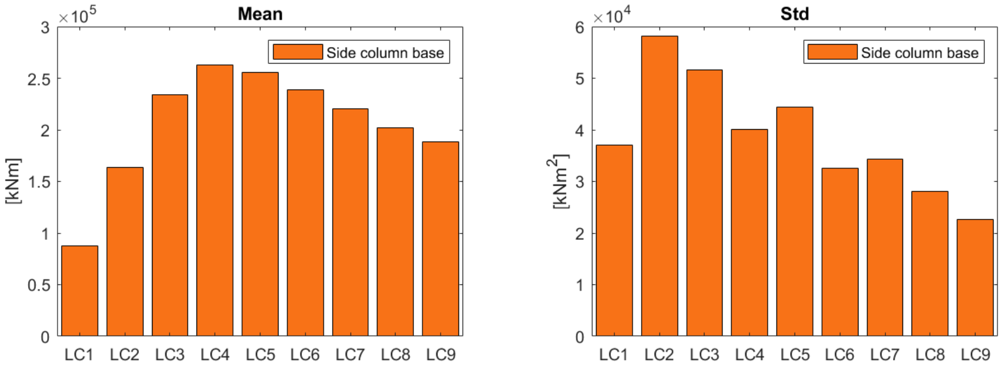

Figure 5.27: Mean and standard deviation of fore-aft bending moment at side column base.

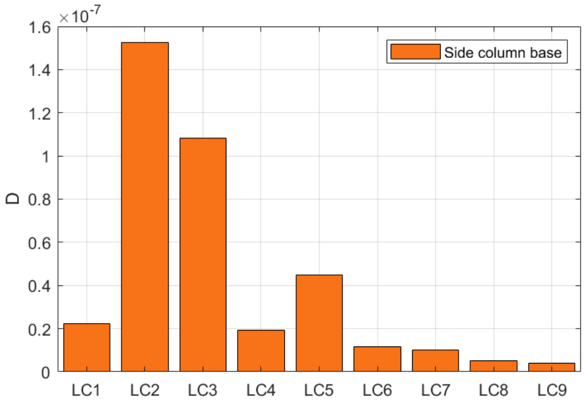

Figure 5.28: 1-hour fatigue damage at side column base.

Results in Figure 5.28 shows that the distribution of fatigue damage does not follow the trend in Figure 5.24. It gives that the simplified strategy applied for tower base is not suitable for analyzing fatigue at side columns. Also, since the outer part of the pontoon is connected with the side column, it can be guessed that the dynamic response of that part is influenced by mooring lines, resonant at surge-motion natural frequency. This will be discussed in the following section.

5.3.3 Sectional Loads on Pontoon

For the 15 MW model, the pontoon is a very long beam, which undertakes very large bending moment also. The pontoon selected is towards the x-axis direction, and the bending moment around y-axis is regarded to dominate the contribution to the sectional stress. The first cross section is the farthest cross section from the central column, while the third is the nearest one.

The time series of sectional bending moments on three cross sections under nine loading cases are plotted in Figure 5.29. The time series plot shows that the largest mean bending moment occurs to the inner section, while the outer section suffers from low-frequency loads most. Figure 5.30 quantifies the mean and standard deviation of bending moment on three cross sections. The trend of mean bending moment versus wind speed is close to that of thrust force. The bar graph of mean value tells that the pontoon close to the central column bears largest mean bending moment. The result is reasonable since the moment on this cross section balances the moment introduced by the gravity on the left. According to the ranking of mean loads on the three cross sections, it can be said that extreme value analysis for ULS should consider the cross sections close to the center. The bar graph of standard deviation illustrates that the largest oscillation occurs to the outer cross section under low wind speed, and the standard deviation of cross section 1 is always the largest from LC1 to LC9. Since the stress is principally determined by the bending moment, high stress cycles can be speculated to exist, and fatigue damage can be large under those low wind speed for section 1. This speculation is proved by Figure 5.31, where estimated fatigue damage at three cross sections are compared.

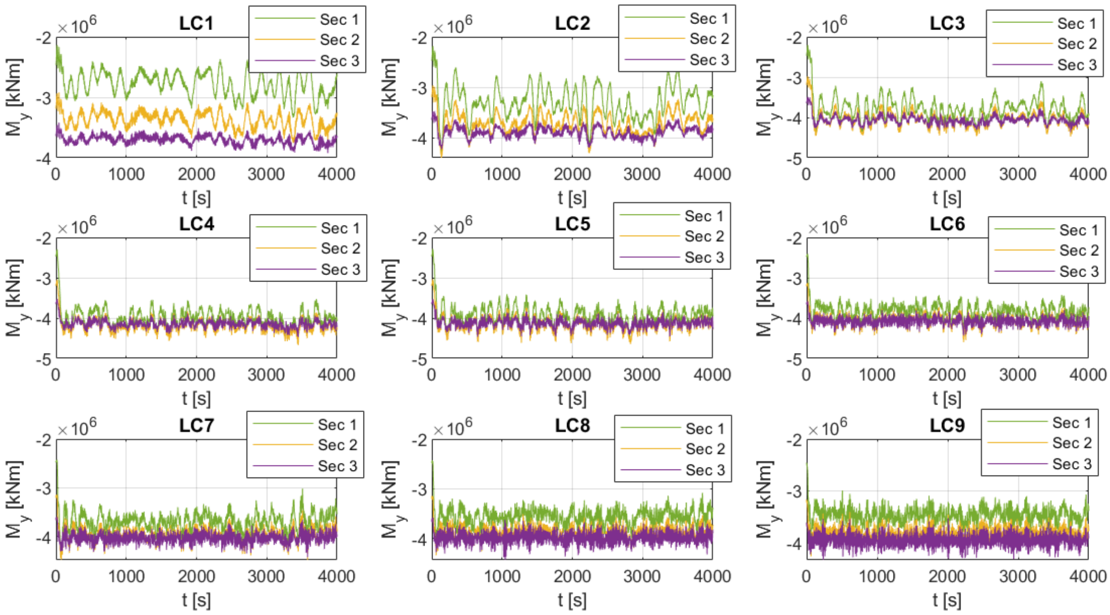

Figure 5.29: Time series of sectional bending moments on three cross sections of one pontoon.

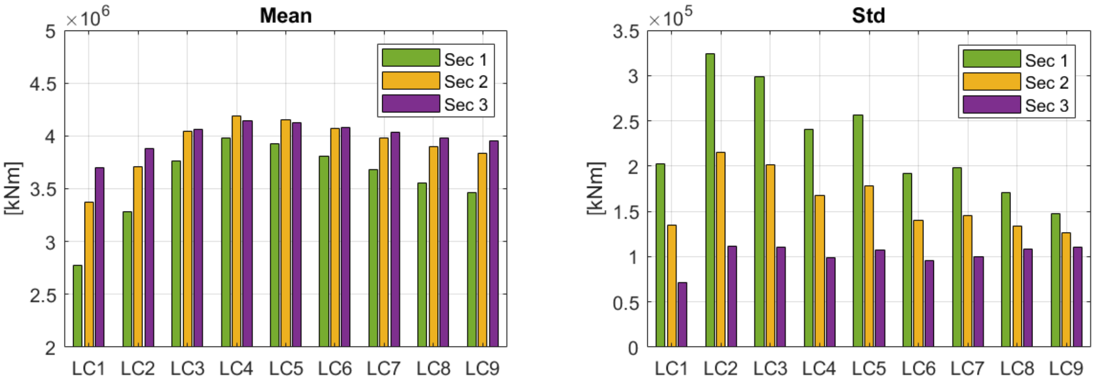

Figure 5.30: Mean and standard deviation of sectional bending moments on three cross sections of one pontoon.

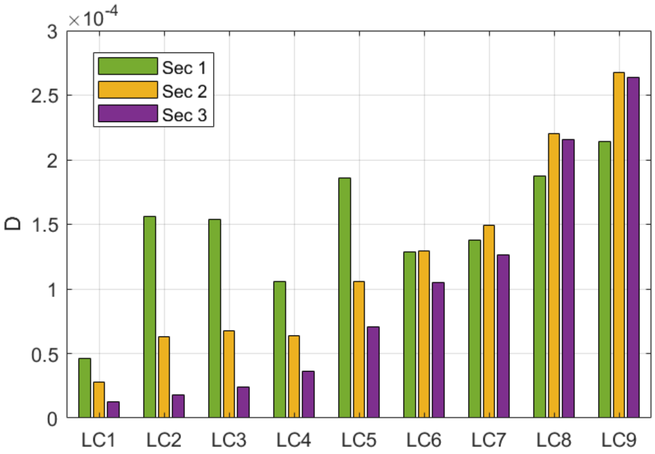

Figure 5.31: Roughly estimated fatigue damage on the three cross sections of one pontoon.

The fatigue damage on the three cross sections are roughly estimated to see the regularity, as plotted in Figure 5.31. The cross section is regarded as a hollow rectangle. Since the fore-aft bending moment contributes most to the stress on the cross section when the wave and wind are aligned, the stress calculated is on the upper surface of the pontoon, where the plate is subjected to large tension.

In Figure 5.31, it is depicted that the sections closer to the central column follows similar trend as that of the tower, as can be seen from the trend of damage on cross section 2 and cross section 3. Estimated damage on section NO.1 does not follow a trend that fatigue damage increases along with wind speed. The fatigue damage under low wind speed stands out and gets close to the fatigue damage under high wind speed.

Power spectra of sectional bending moments on three cross sections are plotted in Figure 5.32 to reason the distribution of fatigue damage. The spectra of cross section 2 and cross section 3 are close to the spectrum of tower base, while the spectrum of cross section 1 is close to that of side column. The sections close to the side column and central column are the hot-spot locations for studying the fatigue around welding area. The two locations present different loading characteristics and should be dealt differently when simplifying the analysis approach. Due to that the inner-space design of pontoons is not confirmed (including girders and stiffeners), the magnitude of estimated fatigue damage is not that accurate. However, the fatigue damage on the pontoon can be dramatic and should not be neglected.

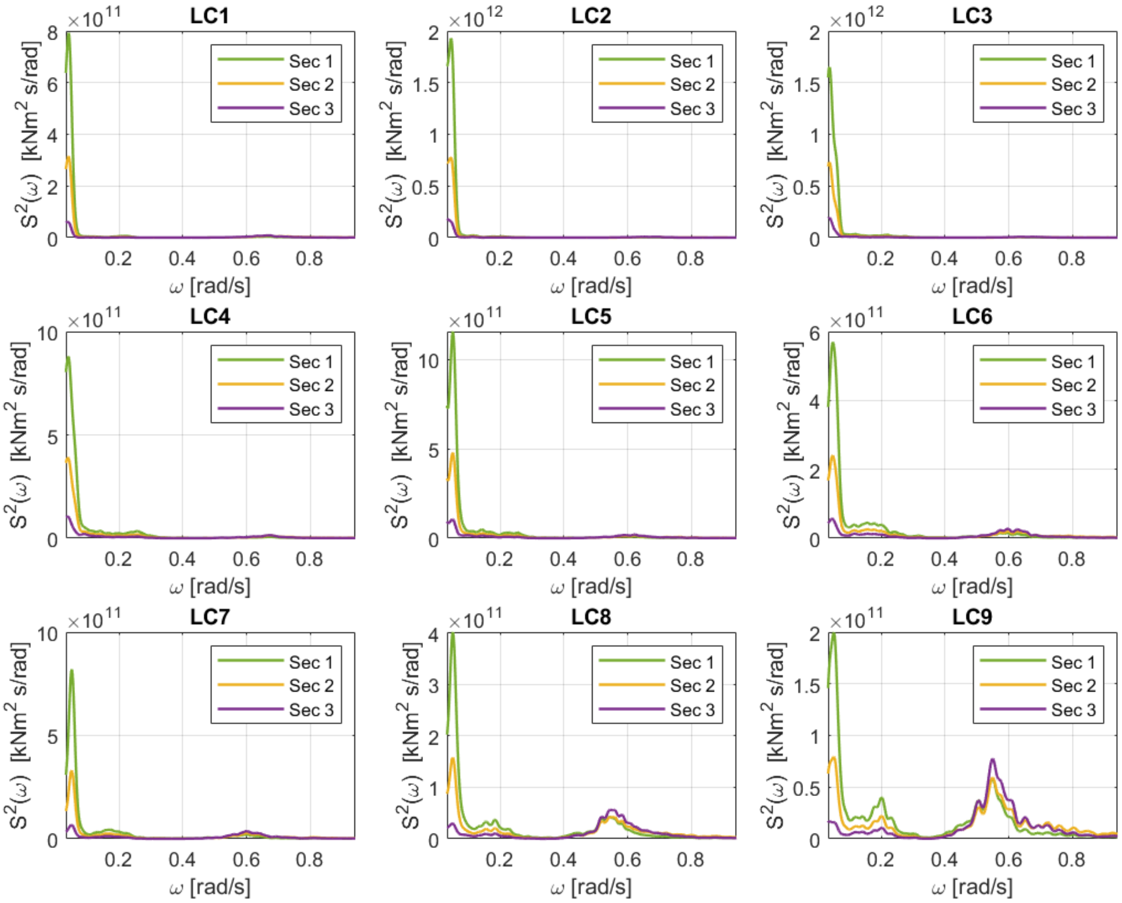

Figure 5.32: Power spectra of bending moments on three cross sections of one pontoon.

5.4 Summary

This section describes the procedure of modeling a multi-body floater model. The modeling is strictly controlled to be consistent with the original rigid-floater model. The comparison through decay test, irregular wave test and turbulent wind test is conducted. the result of comparison verifies the correctness of selected modeling scheme. The sectional dynamic response is also explored using the newly-built multi-body floater. The results from those cross sections provide some insights into the future work of fatigue on floater hull.

- The load range of bending moment at central column base is very large. The central column may undertake larger fatigue damage than the tower base. The tower base design should be careful concerning fatigue issue.
- The side column may not suffer from large fatigue damage. But larger fatigue damage occurs to the weather with lower wind speed.

- Very severe fatigue damage is likely to occur to the pontoon. The pontoon should also be specially designed to avoid severe fatigue failure.
- The location close to the joint of central column and pontoon suffers from not only large fatigue damage but also large extreme load.
- Fatigue analysis to the locations close to central column can apply the same simplified manner, since the results from those locations present similar dynamic characteristics.
- Fatigue simplification to different locations on the floater may vary, since the dynamic response is very different from center to the side.

The study in this section also has some insufficiency that should be improved.

- The values calculated especially at the pontoon cannot be regarded to be accurate enough. Detailed inner design is needed for further analysis.
- The connections between sub-bodies are quite stiff to keep the consistence with rigid-floater model. There is the concern that the result may be very different if the floater is very flexible in reality.
- There is not a positive correlation between mean wind speed and fatigue damage of those locations on the side. High fatigue damage occurs to scenarios with low wind speed. The reason for the high fatigue damage at low wind speed should be found.
- More loading cases should be given to confirm that locations around the center present similar regularity in fatigue response.

Chapter 6

Long-term Fatigue Analysis

Driven by the motivation of exploring regularities behind fatigue problem and simplifying fatigue analysis at the early design phase of a ultra-scale FOWT, long-term fatigue analysis is conducted. The selected reference location is the tower base. There are several reasons for that as listed.

- The design parameter of the tower is confirmed and practiced by IEA. Although the numerical model for floater analysis is established, due to that the inner design (including girders or stiffeners) of the floater is not confirmed yet, long-term analysis to the floater hull is not that practical.
- The locations around the center exhibit similar response characteristics to the tower base. The result of tower base can provide insights into the fatigue issue at other locations.
- The fatigue at tower base should be studied first. If the tower base fatigue is intolerable at the beginning, other locations on the floater cannot be spared.

In this section, the work concentrates on the the analysis of results from large-amount simulations. The distribution of fatigue damage and relative regularity are visualized to provide some insights for the further analysis dealing with large-scale FOWTs.

6.1 Condition Set for Time-domain Simulations

Metocean design basis is developed based on the work of Li et al. [44]. Scatter diagrams with Hs, Tp and Uw are developed as the input of time-domain simulations. The selected bin size creates in total 2376 environmental conditions to be considered. However, many of these 2376 cases has very low probability of occurrence. According to the DNV standard [49], environmental conditions which are below the probability level of 10^{-4} are excluded. After filtering, there are in total

1018 cases that should be taken into consideration. The sum of probability of these cases is close to 99%. However, this number is still very large for the exploration stage. The size of the condition set is shrunk further into 383 cases, after cases with probability lower than 10^{-3} are filtered out. The sum-up probability of 383 cases is around 80%. In the stage of exploring and understanding the fatigue behavior of the 15MW model, a medium-size condition set is preferable for the avoidance of time wasted on meaningless results.

The exact size of the condition set should be multiplied by the number of random seeds. The number of seeds means the number of realizations at given wind and wave condition. The usage of different realizations is to cover the stochastic uncertainties. The number of seeds recommended by Kvittem [6] is 10. The selection of 6 random seeds is also pointed out to be applicable. 6 seeds multiplied by 383 environmental conditions makes 2298 cases in total. Before running thousands of simulations, it is smarter to examine the minimum number of random seeds, since increasing one more seed means adding additional 383 simulations. Therefore, most probable combinations of Hs and Tp under each wind speed are selected as the testing set. This means that there are two groups of simulations. The first group tests the influence of random seeds, while the second group maps fatigue damage into scatter diagrams.

Based on the discussions above, two groups of simulations are accomplished. Group one includes most-probable combinations of Hs and Tp under each given mean wind speed. These cases can provide an outlook about how the fatigue damage distributes along with mean wind speed. Each case has 6 random seeds. This work can help to find a minimum number of time-domain realizations which are sufficient to return an accurate fatigue estimation. If the number of seeds can be reduced, the computational effort for fatigue analysis can be reduced significantly. The cases of most probable combinations of Hs and Tp under each mean wind speed are listed in Table 6.1.

Uw [m/s]	**Hs [m]**	**Tp [s]**	**Prob**
4	1.75	9.5	0.39%
6	1.75	9.5	0.55%
8	1.75	9.5	0.59%
10	2.25	9.5	0.58%
12	2.75	10.5	0.51%
14	3.25	10.5	0.40%
16	3.25	10.5	0.28%
18	4.25	11.5	0.19%
20	4.75	11.5	0.12%
22	5.25	11.5	0.07%

Table 6.1: Most probable combinations of Hs and Tp under each mean wind speed.

The second group is a large number of time domain simulations which cover approximately 80% of the possible environmental conditions. The result is set as a reference for comparison. Predicted result from simplified method will compared with the result from raw data to verify the accuracy of prediction. The probability distributions of selected 383 cases under each mean wind speed are plotted in Figure 6.1.

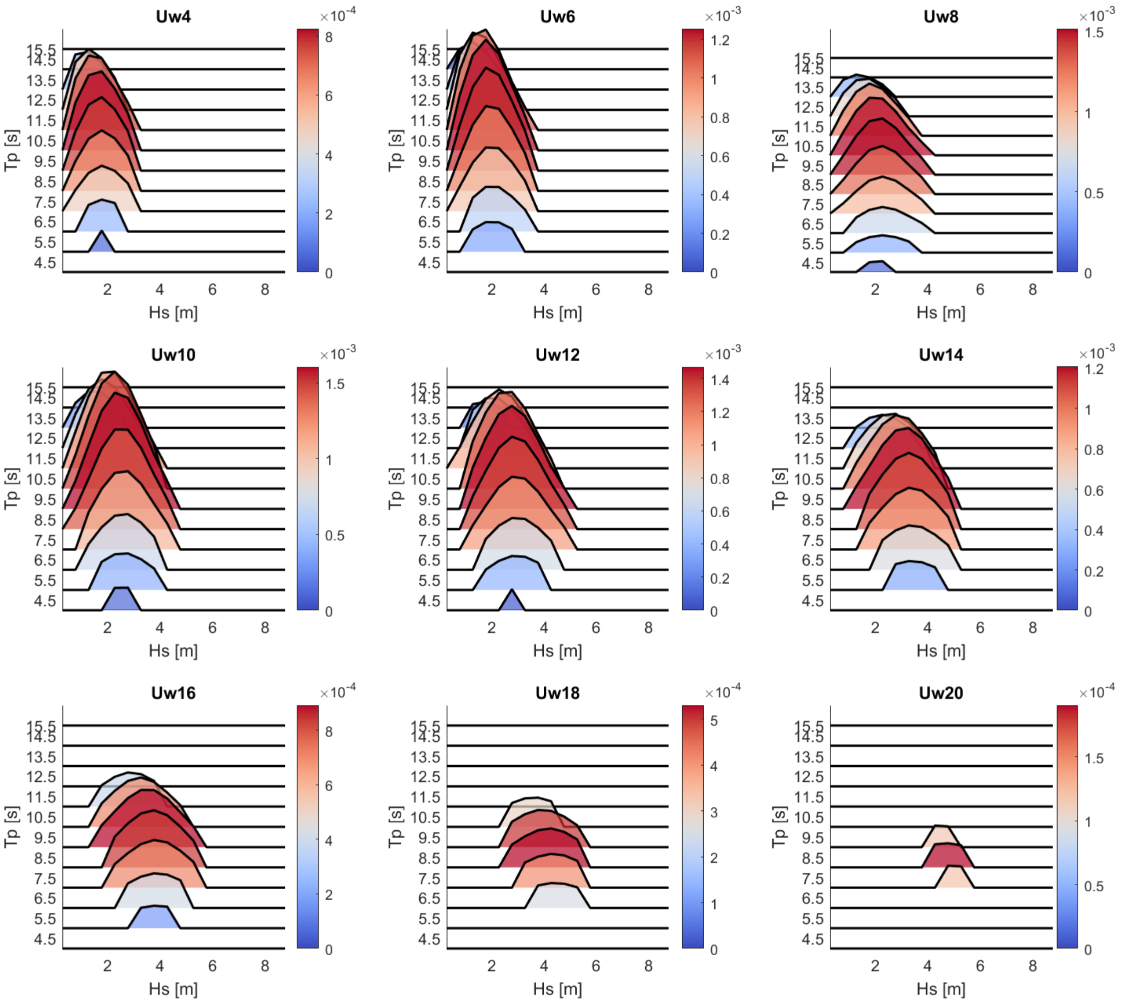

Figure 6.1: Distribution of sea states of given Uw, Hs and Tp.

In Figure 6.1, the height or color of these ridges in the plot reflects the probability density at given Hs and Tp. This plot is set as a reference. Similar plot will be made to fatigue damage D^*, which is the damage at given Hs and Tp multiplied by corresponding probability. Through comparing the plot of D^* and probability density, the influence of probability to exact fatigue damage can be observed.

6.2 Results From Time Domain Simulations

6.2.1 Results from Simulation Group 1

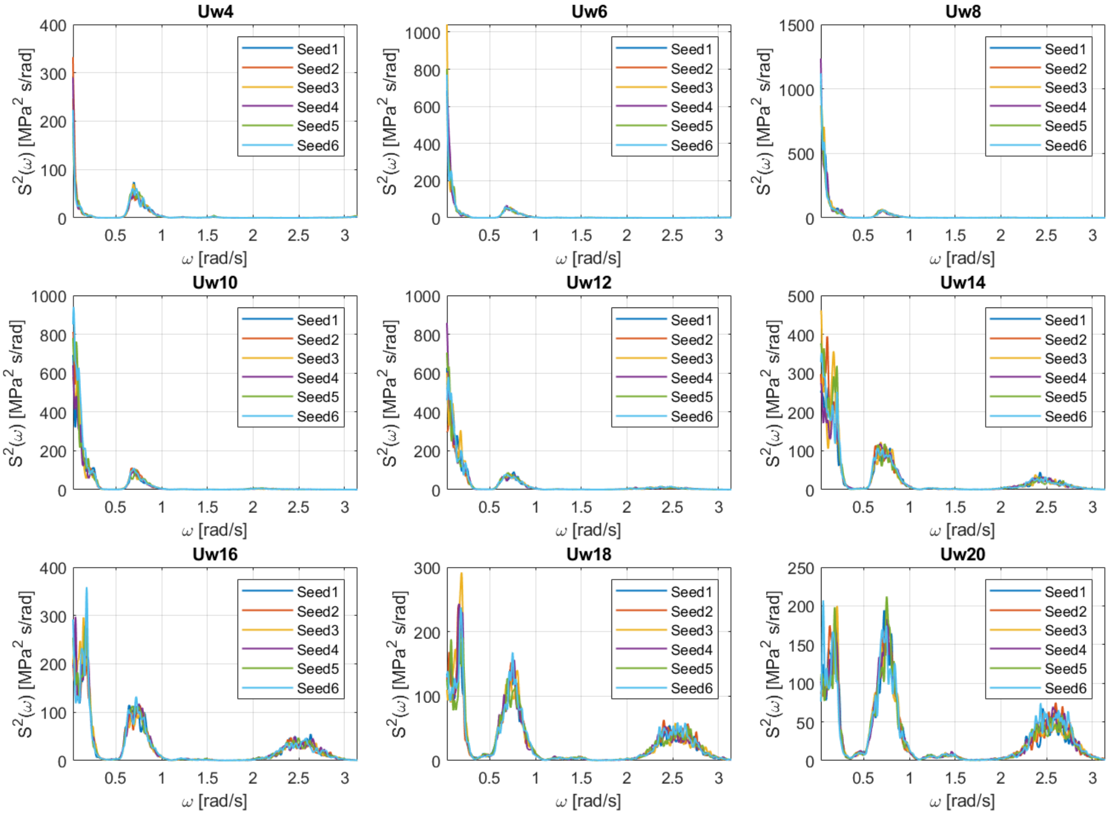

Figure 6.2: Spectrum comparison of most probable combination of Hs and Tp under each mean wind speed using 6 random seeds.

Before comparing fatigue damage, there is the necessity of examining the dominating frequency component through spectrum analysis. Figure 6.2 compares the power spectra of most probable combinations of Hs and Tp under each mean wind speed using six random seeds. The spectra plot in Figure 6.2 matches that in **??**. The six-seed spectra gives similar frequency components and spectrum density amplitude. There is only observable difference in the amplitude of spectrum density at low frequency, which is due to the stochastic nature of turbulent wind. It can be noticed that the proportion of wave-frequency and high-frequency components is improved, as the wind speed is increasing. It can also be noticed that the amplitude of spectrum density at around $\omega = 0.23rad/s$ is improved as wind speed is increasing. This frequency is the pitch motion natural frequency. The strengthened pitch motion will contribute significantly to the dynamic response at the cross section of tower base.

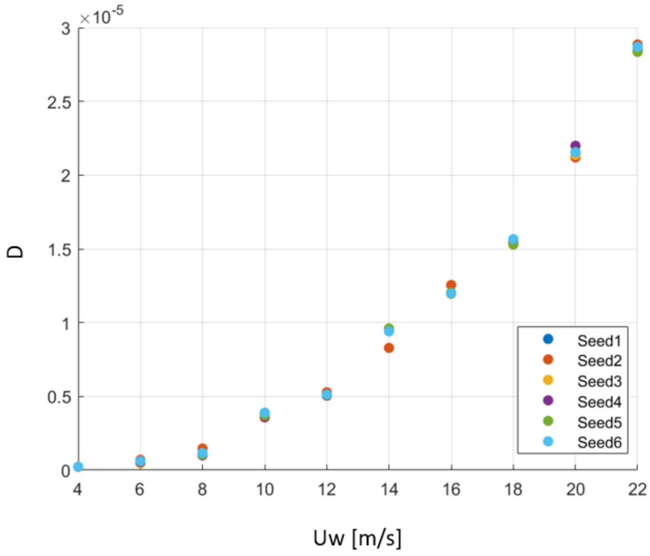

Figure 6.3: Fatigue damage of the most probable combination of Hs and Tp under each wind speed, using 6 random seeds.

The fatigue damage result of group one simulation is plotted in Figure 6.3. This scatter graph is to prove that less random seeds is also applicable for long-term analysis. Also, the scatter graph can serve for data fitting. The six series of scatters in the plot represent the fatigue damage result from six random seeds, marked with 6 different colors. Under each wind speed, the scatter from six random seeds almost covers each other. The plot gives the information that the number of seed has very small influences on the result of fatigue damage, with only the case of Uw = 14m/s presents larger variance. Simulations with one random seed can be applicable at the early stage of fatigue analysis, which will reduce the workload significantly. The distribution in this plot is seen to follow certain trend that the fatigue damage increases along with the enhancement of mean wind speed. This can be explained by the result of spectra study in Figure 6.2. Figure 6.2 has revealed that the contribution from excited pitch motions is enhanced as the wind speed is increasing (but it should be noticed the Hs is also increasing). Since the trend in Figure 6.3 bonds fatigue damage and wind speed in certain relationship (the fatigue damage versus wind speed follows an approximate parabolic shape), this means that a mathematical model can be established to simplify the analysis. Granted, this finding is currently limited to this semi-submersible 15-MW FOWT model. Tt is of necessity to study different large-scale and ultra-scale FOWT models to check if there is the regularity in common.

6.2.2 Results from Simulation Group 2

The simulation group 2 emulates 383 loading cases using one random seed to calculate the fatigue damage at tower base. The fatigue result is remapped to scatter diagrams for the observation of regularities.

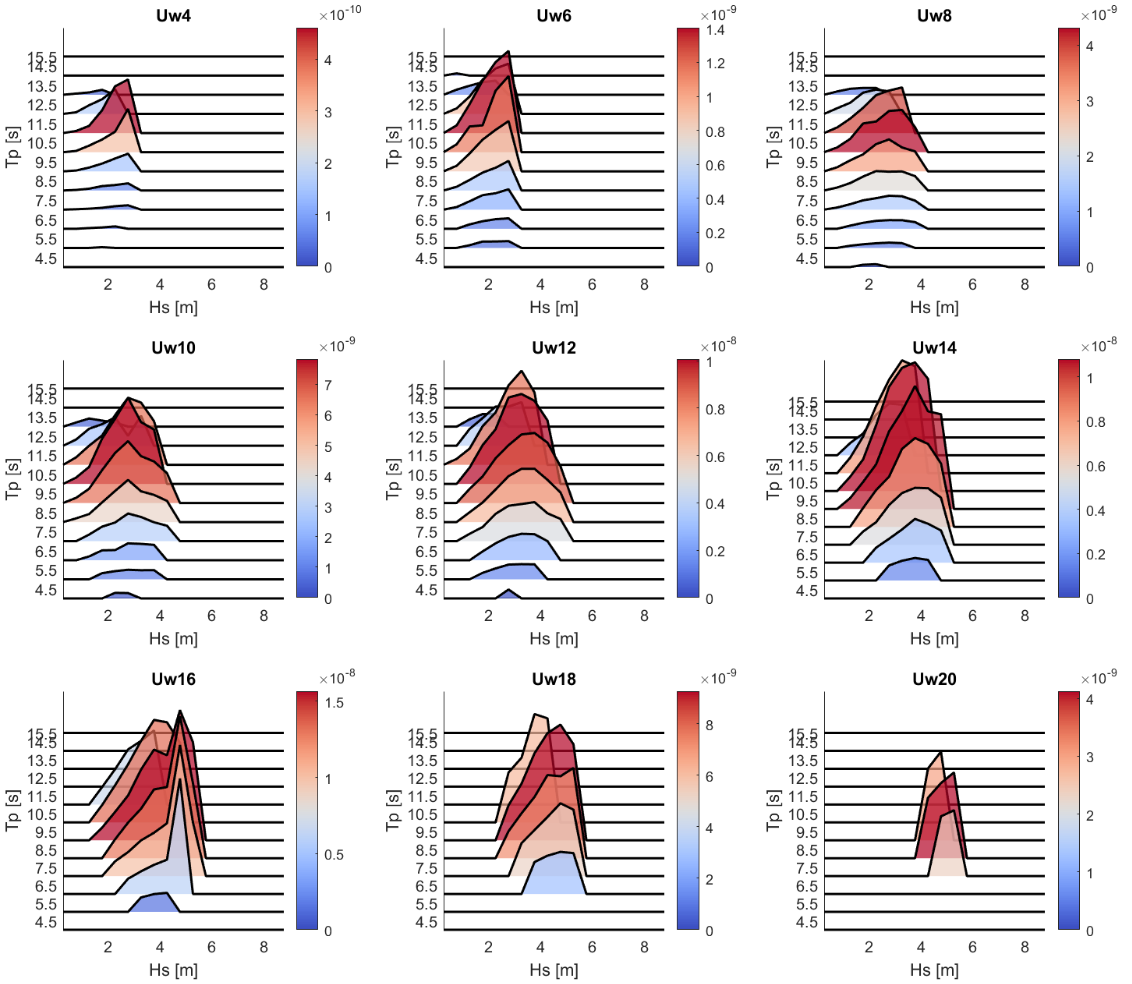

Figure 6.4: Distribution of D^* (fatigue damage multiplied by corresponding probability of given Uw, Hs and Tp) versus Hs and Tp under each wind speed; $D^* = D * f_{U_w,H_s,T_p}(u,h,t)$.

Figure 6.4 visualized the distribution of the tower base fatigue damage at given Hs, Tp and Uw multiplied by corresponding probability, which is marked as D^*. The shape of fatigue damage distribution in Figure 6.4 is close to that in Figure 6.1, which can be observed through comparing Figure 6.4 and Figure 6.1. The probability distribution generally controls the distribution of exact fatigue damage. This indicates that the selection of metocean design basis is important, which influences the final fatigue damage result.

The fatigue damage under each selected environmental condition is highlighted in Figure 6.5, with the lowest in blue and highest in red. This plot is made through remapping fatigue damage to those scatter diagrams. The fatigue damage highlighted in Figure 6.5 is the fatigue damage D, which is not multiplied by probability. This plot can generally describe how fatigue damage is influenced by Hs and Tp.

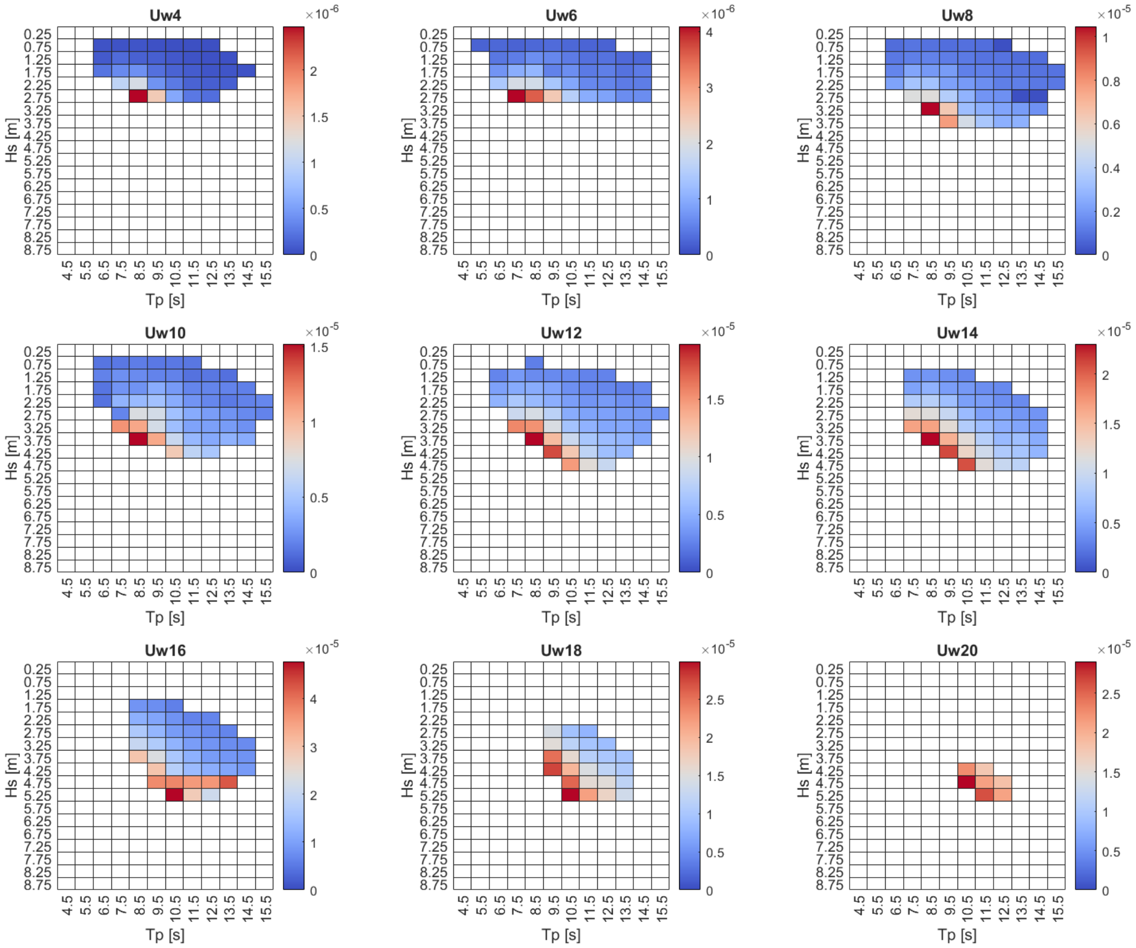

Figure 6.5: Distribution of D (fatigue damage without being multiplied by corresponding probability of given Uw, Hs and Tp) versus Hs and Tp under each wind speed.

Combining Figure 6.5 with the scatter diagram in Appendix C, it can be noticed that the highest-damage case is not located at the higher-probability zone. Instead, there is the trend that the individual fatigue damage is increasing towards the direction of steeper waves, which can bring larger wave loads. This regularity is not going to be expanded here, since the selected cases only take up half picture of the distribution. The summarize of fatigue damage versus Hs and Tp should be based on larger condition set.

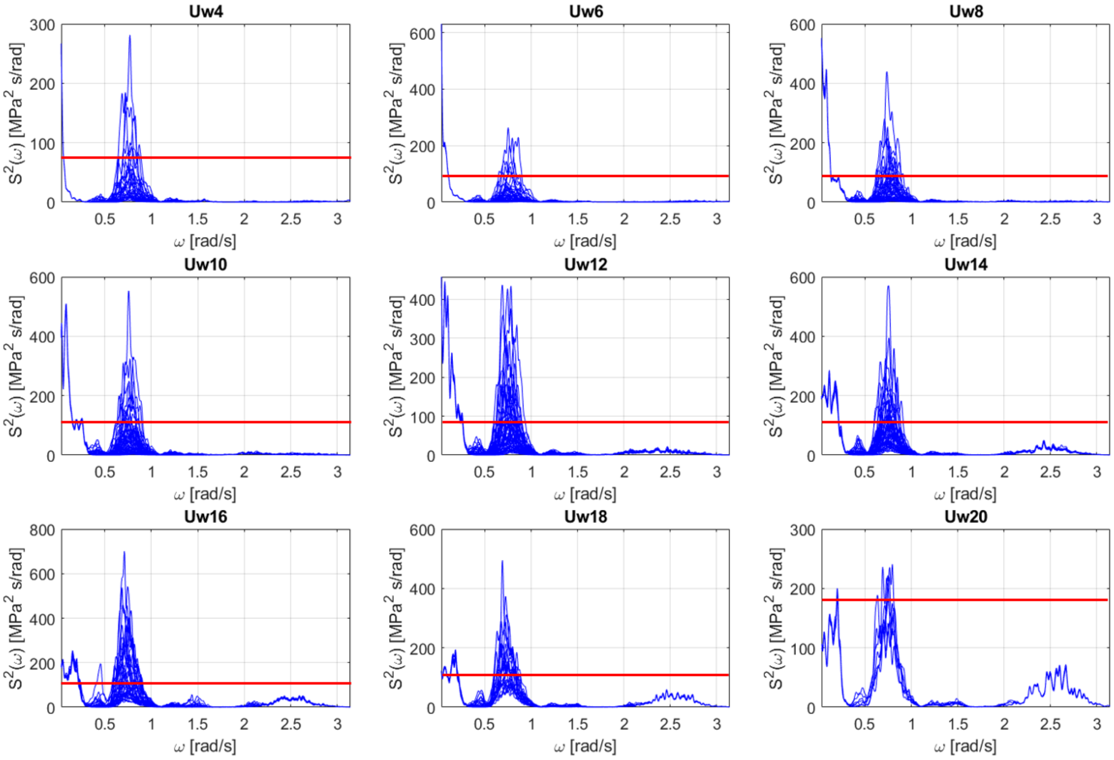

Figure 6.6: Spectrum comparison of stress power spectra of 383 simulations (the red line means the amplitude of peak at wave frequency of most probable cases).

Figure 6.6 displays the spectra of stress from all combinations of Hs and Tp under each mean wind speed. The two main peaks are located at low-frequency range and wave-frequency range respectively. The red horizontal line levels out as the amplitude of spectrum density at wave frequency of most probable combinations of Hs and Tp. The amplitude of spectrum density at low-frequency range is the same for all the cases under certain wind speed. This tells that the change of Hs and Tp has negligible influence on the low-frequency response. The peak of spectrum density at wave frequency varies in a wide range. For the cases of which wind speed ranges from 4m/s to 14m/s, majority of the peaks at wave frequency is below the red line. This implies that wave-frequency contribution of most probable cases benchmark at an average level.

After the spectra study of all the simulation results, there is also the need of checking the fatigue contribution of most probable combinations of Hs and Tp. This is to prove that the finding in Figure 6.3 can be used for making simplifications. To check the contribution of those most probable cases, the fatigue damage should be multiplied by corresponding probability. Figure 6.7 can be obtained after the values of each grid in Figure 6.5 are multiplied by corresponding probability in scatter diagrams.

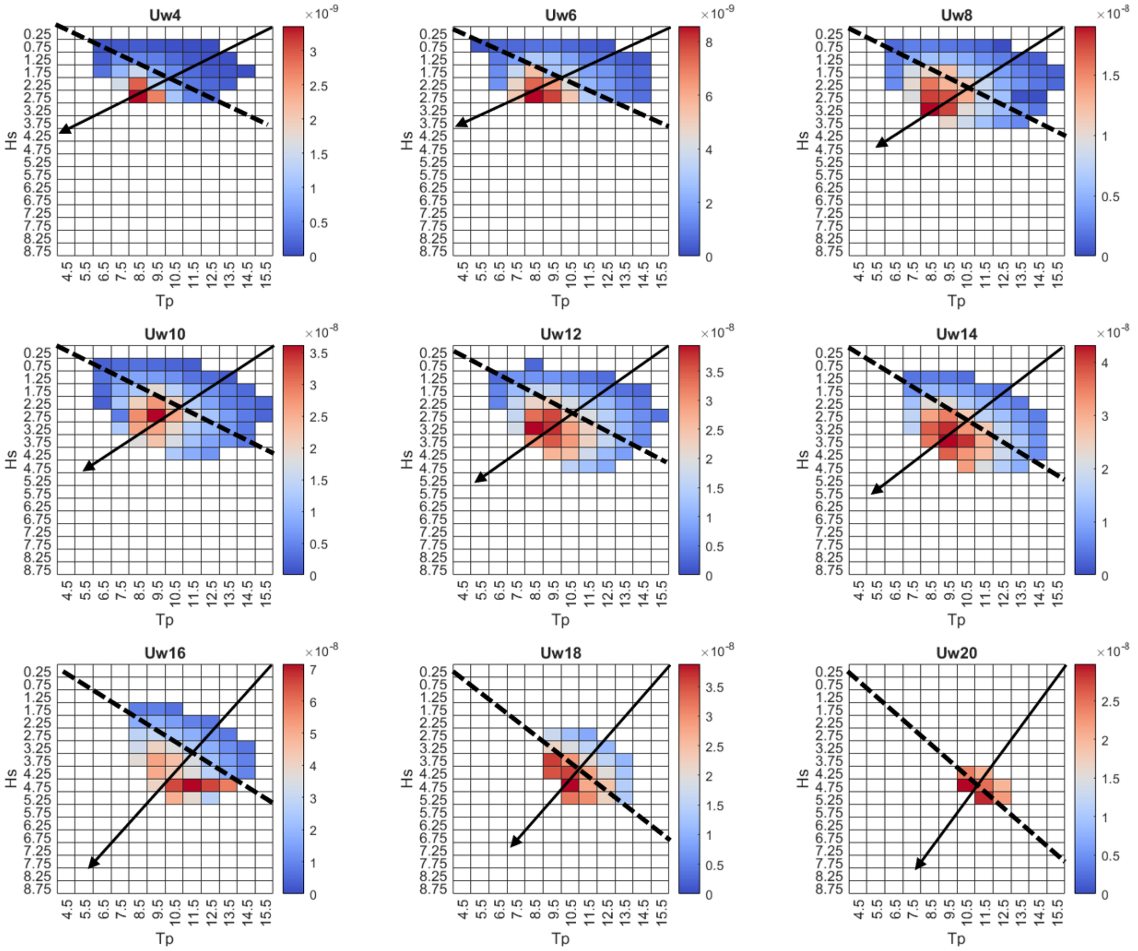

Figure 6.7: Distribution of D^* (fatigue damage multiplied by corresponding probability of given Uw, Hs and Tp) versus Hs and Tp under each wind speed; $D^* = D * f_{U_w,H_s,T_p}(u,h,t)$; The black arrow points towards the direction that fatigue damage is increasing; The black dot line marks the average level of fatigue damage.

In Figure 6.7, the black arrow points towards the direction that fatigue damage is increasing, while the black dot line marks the average level of fatigue damage. The intersection of these two lines is around the location of most probable combination of Hs and Tp. Furthermore, the fatigue damage of most probable cases is compared with the mean damage under each mean wind speed in Figure 6.8. Except the case of $Uw = 16\,m/s$, the damage of most probable cases is very close to the average level at given wind speed. This means that fatigue damage of most probable combination of Hs and Tp under each Uw can be representative of the average fatigue level. According to Figure 6.8, it should be pointed out that very large fatigue damage occurs at $Uw = 16\,m/s$. The corresponding Hs and Tp can be found in Figure 6.5, being $5.25m$ and $10.5s$ respectively.

Based on this suppose and the trend in Figure 6.3, the first idea of simplifying fatigue analysis comes out that most probable case under several wind speed can be simulated and used to predict the total fatigue damage.

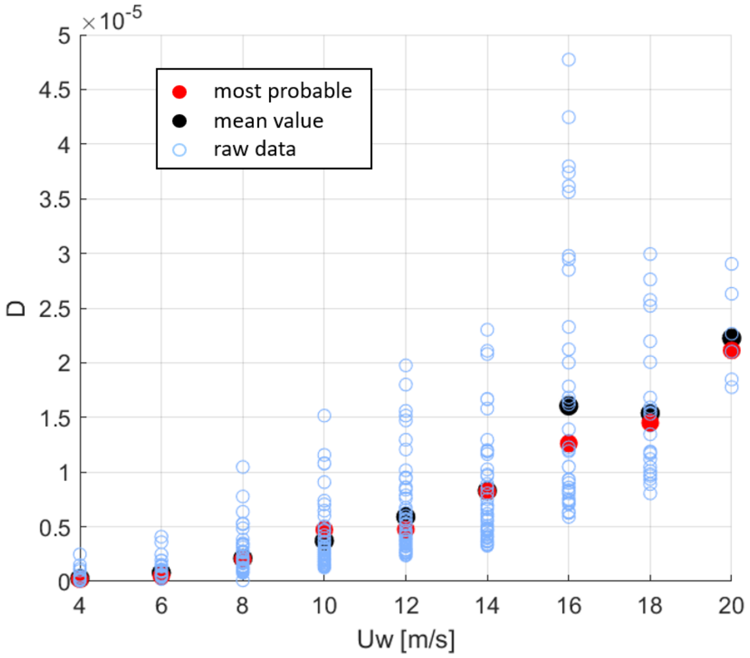

Figure 6.8: Fatigue damage comparison; Blue scatters are the results from 383 simulations; Black scatters are the mean damage at each wind speed; Red scatters are the damage of most probable cases.

6.3 Fatigue Prediction Based on Most Probable Cases & Linear-regression Model

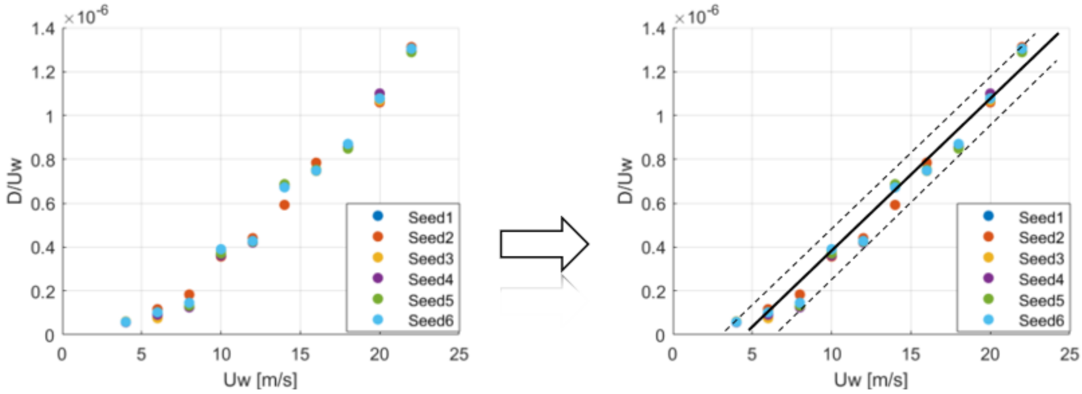

Figure 6.9: Linearized data of six-seed fatigue damage of most probable combination of Hs and Tp under each wind speed.

The data plotted in Figure 6.3 can be reorganized to find a proper regression model. The first attempt is to linearize the data and use linear regression to fit in a linear model. Since the raw data is in non-linear shape, the fatigue damage is divided by the integral power of corresponding mean wind speed to exploit a linear relationship.

It is found that the fatigue damage divided by mean wind speed presents a linear trend as shown in Figure 6.9. The fitted linear model after linear regression is shown in Figure 6.10. In Figure 6.10, the data is from 1-seed average to 6-seed average in the six subplots respectively. The fitted linear model and confidence bounds are colored in red. It can be observed that the data is within the 95% confidence range. The linear model can be a predictor of most probable damage under each wind speed.

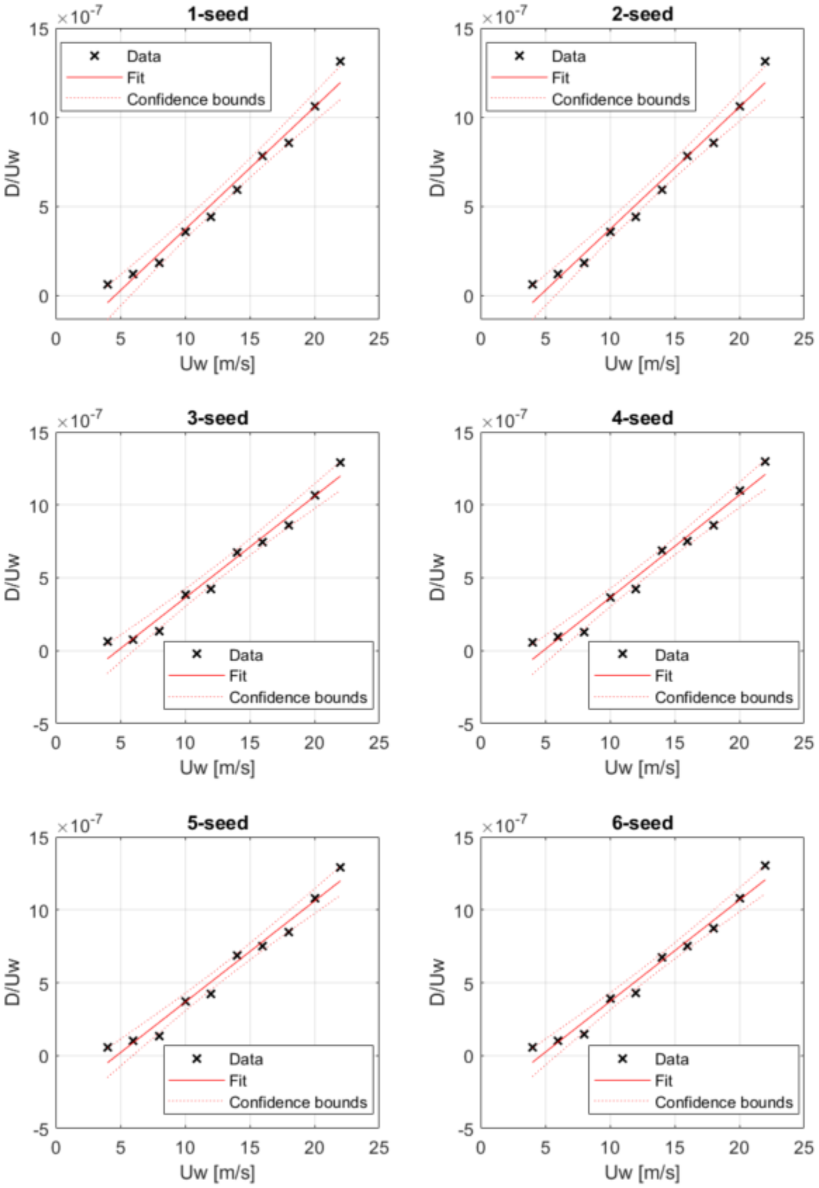

Figure 6.10: Linearized data of six-seed fatigue damage of most probable combination of Hs and Tp under each wind speed (using 1 seed average, 2 seed average, 3 seed average, 4 seed average, 5 seed average and 6 seed average respectively.

with the linear regression model and simulation results, predicted fatigue damage can be compared with result calculated from raw data. Table 6.2 provides the estimated damage from both 2-group simulation data and linear regression model. The group 2 data is selected as the reference due to the data size. The ϵ is the reletive error compared to the group 2 dataset. The group 1 data is used to compare the influence of the choice of seed number on the accuracy of damage prediction. The linear regression results include the model developed from different number of samples. The 5-sample linear model selects one cut-in-range speed, two rated-range speed and two cut-out-range speed, while the 3-sample linear model selects one cut-in,rated-range and cut-out speed respectively.

	D	ϵ
383 simulations	7.23E-06	
1-seed most probable cases	7.16E-06	1.02%
2-seed most probable cases	7.16E-06	1.02%
3-seed most probable cases	7.16E-06	1.02%
4-seed most probable cases	7.17E-06	0.87%
5-seed most probable cases	7.19E-06	0.57%
6-seed most probable cases	7.25E-06	0.25%
Linear model (9 samples)	7.48E-06	3.50%
Linear model (5 samples)	7.20E-06	0.44%
Linear model (3 samples)	7.57E-06	4.63%

Table 6.2: Comparison between fatigue damage estimated from large-amount simulations, most probable cases under each wind speed and linear regression model.

The result in Table 6.2 reveals the nature of linear regression that the selection of fitting samples has influence on the accuracy of predicted result. A proper selection of sampling data can significantly improve the accuracy as indicated by the result of using 5 sampling points, of which the relative error is barely 0.44%. It should also be noticed that the result from group 1 using 6-seed averaged result can also produce very accurate prediction, of which the the relative error is barely 0.25%. The increase of number of random seeds can help improve the accuracy of damage prediction, while the improvement from using 1-seed result to using 6-seed averaged samples is approximately 0.77%, which is very small. The prediction of using most probable cases under each wind speed controls the relative error within 1.02%, the accuracy can be over 98.98%. This in return proves the suppose based on Figure 6.5 that the most probable combination of Hs and Tp under each wind speed benchmarks the average level.

6.4 Summary

With the goal of exploring regularities behind fatigue issue, large amount of simulations are conducted and relevant data is processed. Some results from this study that can be helpful for future work dealing with large-scale FOWTs. The useful results are summarized as follows

- The distribution of fatigue damage has correlation with the metocean model selected.

- Pitch motion is important to the fatigue performance under the condition where wind and wave are aligned. For the design and optimization of FOWT, pitch control can help to decrease the risk of fatigue failure.
- Fatigue damage in general increases towards the direction of steeper wave and stronger wind.
- Most-probable combinations of Hs and Tp under each Uw can be used for fatigue predication, which returns quite accurate result.
- The condition set for time domain simulations can be further reduced through linearization of damage versus mean wind speed.

This study provides an overview of the fatigue issue related to ultra-scale FOWTs. There are also some limitations in this study.

- Remapped scatter diagram of fatigue damage distribution exactly gives half side of the full picture. A more complete picture with more cases is preferable to study the influence of Hs and Tp.
- Linear regression model is developed based on the finding of certain regularity. It returns surprisingly pleasant result in this special case regarding a 15-MW FOWT. But there is uncertainty if fatigue damage of any other large-scale FOWTs presents similar regularities.
- The study is limited to tower base. If the detailed design of floater is finished, it is preferable to study the fatigue damage at different locations on the floater hull.
- The study is also limited to one FOWT. There is the likelihood that the regularity found in this study is special to this case. Studies to more different large-scale and ultra-scale models are meaningful for summarizing common regularities.
- The applied scenario is that wind wave are aligned in 0°, which maximizes the influence of fore-aft behavior. There should be the work considering wind and wave from different directions to see if there is similar regularity behind fatigue issue.

Chapter 7

Conclusion & Discussion

Offshore wind is playing an important role in the global energy transition. The increasing need and decreasing cost of offshore wind drives the industry and research groups look towards larger wind turbine. With the turbine being upscaled, the design of supporting structure faces many challenges. In the work of this thesis, two challenges regarding a 15 MW FOWT have been proposed. One challenge is about the calculation of dynamic response on floater hull in numerical simulations. The other challenge is about fatigue analysis to the structure. In the work of this thesis, efforts towards these two challenges have been made. Regarding the first challenge, the functionalities of available simulation tools are exploited to study the dynamic response on floater hull. For the second challenge, some regularities are found from large amount of simulation results, and one simplified method has been proposed. Some conclusions regarding the thesis work and suggestions for future work are discussed in this final chapter.

7.1 Conclusion

The numerical model of 15 MW FOWT is modeled in SIMO/RIFLEX to implement fully-coupled time domain analysis. In the numerical tool, the aerodynamics of wind turbine is described by BEM, and hydrodynamics of the floater is described by potential flow theory. The blades, tower and mooring lines are modeled as flexible beams, described by Euler-Bernoulli beam theory. The numerical model is verified first through comparison with the result provided by IEA. The model is verified to be correctly set up.

When it comes to the study regarding multi-body floater, the modeling scheme in SIMO/RIFLEX has simplified the analytical procedure for obtaining response on the floater hull. With this scheme, the time for simulations is not increased, since there is no need for coupling SIMO/RIFLEX with other FE program. An exploratory study has been proceeded to compare dynamic response at different locations. The fatigue damage at these locations are roughly estimated to provide insights for further design and optimizations. The underwater-part central column is more vulnerable to fatigue failure compared to tower base, while the side column is relatively safe and mainly affected by the mooring line behavior. Although the damage calculation overestimates the fatigue on the pontoons, fatigue damage on pontoons is still non-negligible. The spectra study plus the estimated fatigue damage indicates that the fatigue issue at different locations can be very different. The result implies that the locations around the center can apply the same strategy for fatigue analysis. The result also indicates that pre-analysis of loading components through spectra study is important for applying proper method to simplify the study.

For the work regarding long-term fatigue analysis, it is found that fatigue damage of most probable Hs and Tp under each mean wind speed are ranked at average level among all the possible cases under each wind speed. This finding tells that most probable cases under each wind speed can be used to estimate fatigue damage. The estimated result from most probable cases under each wind speed and result from large-amount simulations has been compared. It is shown that the estimation based on most probable cases can control the relative error within 1%. This means that there is very high confidence in the prediction using $11 \sim 66$ out of 383 simulations.

The other finding is that fatigue damage under each wind speed generally follows a trend ($D \propto U_w$). The trend enables fitting samples with regression model, and linear regression is sufficient to describe this regularity. The general strategy is to select samples around cut-in, rated and cut-out wind speed first. And then linear regression technique is applied to these sampling points to get a predication function. Using linear regression, the needed cases can be reduced to 3, which returns over 95% accuracy. It should be noted that the accuracy of linear-regression model varies with the selection of sampling points. A proper selection can optimize the accuracy of prediction up to over 99%, while a poor sample set can still return approximately 95% accuracy. The study also highlights the importance of spectra analysis, which can provide information for selecting a both simplified and accurate manner of fatigue analysis. The spectra study provides evidence that pitch motions are strengthened with the increase of mean wind speed. Pitch motions contribute to the fore-aft bending moment significantly, which causes large fatigue damage at the tower base.

7.2 Recommendations For Future Work

This thesis has provided insights into how to implement analysis to the floater hull of semi-submersible platform in time domain simulations. However, there are deficiencies in this part of work. For the improved modeling scheme itself, one third of the floater is modified with flexible connections, since the fore-aft behavior is assumed to be most important. Further improvement is to divide the entire floater into sub-bodies, which enables the analysis to side-side behaviors. This should be proceeded to make the analysis complete. There is also the deficiency in the floater parameters. The detailed design inside the floater has not been confirmed yet by the group who put forward this conception model. The estimated fatigue damage up to now is not sufficiently accurate. For further analysis to floater hull, the inner design should be accomplished first. Furthermore, the exact flexibility is unknown and unable to be verified in current stage. It can be predicted that the result of dynamic response can be very different if the exact floater is very flexible.The flexibility of floater hull is of interest for future study. But there should be model experiment as comparison to verify the result.

As concluded, the work in this thesis look into the fatigue issue through remapping fatigue damage into scatter diagrams. Some regularities are found and a simplified method for estimation is put forward, but there is still insufficiency in this part of work. The first limitation is that the long-term analysis does not cover all the possible environmental conditions. It is preferable to expand the picture in the future to improve the confidence in the result. In this way, more detailed study regarding influence of Hs and Tp can be expanded. Based on the whole picture of fatigue damage distribution in scatter diagrams, a lumped method of environmental variables can be put forward. Besides, the study of simplification on fatigue estimation is limited to the tower base. More locations should be studied to prove that certain regularity or certain method can be applied to most of the locations on the FOWT. The result in this thesis is also limited to only one FOWT model. The regularity found is likely to It is uncertain if the same regularity may occur to other FOWTs. A more advanced simplified method should be able to cover more prototypes. It is recommended to study the fatigue of more models, for example, to study 10 MW, 12 MW, and 15MW models. If there is similar regularity found in the study of these models, it can be concluded that the regularity is applicable to large-scale and ultra-scale FOWTs.

As summary, the thesis makes contributions towards numerical analysis to floater hull of FOWTs and fatigue analysis regarding a large-scale FOWT. It provides insight into how to conduct fatigue analysis to the substructure of a new concept model. The study in this work can be further improved through increasing research object and scale.Also, the detailed design of floater can be made for fatigue analysis.

Bibliography

1. Henderson AR. Analysis tools for large floating offshore wind farms. University of London, University College London (United Kingdom), 2000
2. IEA. Offshore Wind Outlook 2019. 2019
3. Musial W, Spitsen P and Beiter P. Offshore Wind Market Report: 2021 Edition. Tech. rep. 2021 Aug
4. Musial W, Butterfield S and Boone A. Feasibility of floating platform systems for wind turbines. *42nd AIAA aerospace sciences meeting and exhibit.* 2004 :1007
5. DNV. Recommended practice DNV-RP-C203: Fatigue design of offshore steel structures. Det Norske Veritas 2011
6. Kvittem MI and Moan T. Time domain analysis procedures for fatigue assessment of a semi-submersible wind turbine. Marine Structures 2015; 40:38–59
7. Svendsen KF. Structural design and dynamic analysis of a tension leg platform wind turbine, considering elasticity in the hull. MA thesis. NTNU, 2016
8. Hegseth JM, Bachynski EE and Karimirad M. Comparison and validation of hydrodynamic load models for a semi-submersible floating wind turbine. *International Conference on Offshore Mechanics and Arctic Engineering.* Vol. 51319. American Society of Mechanical Engineers. 2018 :V010T09A075
9. Brevik VN. Elasticity, Wave Load Modeling and Upscaling of Spar Floating Wind Turbine. MA thesis. NTNU, 2021
10. Luan C, Gao Z and Moan T. Development and verification of a time-domain approach for determining forces and moments in structural components of floaters with an application to floating wind turbines. Marine Structures 2017; 51:87–109
11. Liu Y and Ishihara T. Numerical Study on Sectional Loads and Structural Optimization of an Elastic Semi-Submersible Floating Platform. Energies 2021; 14:182
12. Passon P and Branner K. Condensation of long-term wave climates for the fatigue design of hydrodynamically sensitive offshore wind turbine support structures. Ships and Offshore Structures 2016; 11:142–66
13. Passon P. Damage equivalent wind–wave correlations on basis of damage contour lines for the fatigue design of offshore wind turbines. Renewable Energy 2015; 81:723–36

14. Zwick D and Muskulus M. Simplified fatigue load assessment in offshore wind turbine structural analysis. Wind Energy 2016; 19:265–78
15. Velarde J and Bachynski EE. Design and fatigue analysis of monopile foundations to support the DTU 10 MW offshore wind turbine. Energy Procedia 2017; 137:3–13
16. Häfele J, Hübler C, Gebhardt CG and Rolfes R. A comprehensive fatigue load set reduction study for offshore wind turbines with jacket substructures. Renewable Energy 2018; 118:99–112
17. Stieng LES and Muskulus M. Reducing the number of load cases for fatigue damage assessment of offshore wind turbine support structures using a simple severity-based sampling method. Wind Energy Science 2018; 3:805–18
18. Stewart GM. Design Load Analysis of Two Floating Offshore Wind Turbine Concepts. 2016
19. Müller K, Dazer M and Cheng PW. Damage assessment of floating offshore wind turbines using response surface modeling. Energy Procedia 2017; 137:119–33
20. Müller K and Cheng PW. Application of a Monte Carlo procedure for probabilistic fatigue design of floating offshore wind turbines. Wind Energy Science 2018; 3:149–62
21. Kim HJ, Jang BS, Park CK and Bae YH. Fatigue analysis of floating wind turbine support structure applying modified stress transfer function by artificial neural network. Ocean Engineering 2018; 149:113–26
22. Allen C, Viselli A, Dagher H, Goupee A, Gaertner E, Abbas N, Hall M and Barter G. Definition of the UMaine VolturnUS-S Reference Platform Developed for the IEA Wind 15-Megawatt Offshore Reference Wind Turbine. Tech. rep. International Energy Agency
23. Bulder B, Van Hees MT, Henderson A, Huijsmans R, Pierik J, Snijders E, Wijnants G and Wolf M. Study to feasibility of and boundary conditions for floating offshore wind turbines. ECN, MARIN, TNO, TUD, MSC, Lagerway the Windmaster 2002; 26:70–81
24. Lee KH. Responses of floating wind turbines to wind and wave excitation. PhD thesis. Massachusetts Institute of Technology, 2005
25. Matha D, Schlipf M, Pereira R and Jonkman J. Challenges in simulation of aerodynamics, hydrodynamics, and mooring-line dynamics of floating offshore wind turbines. *The Twenty-first International Offshore and Polar Engineering Conference*. OnePetro. 2011
26. Cordle A and Jonkman J. State of the art in floating wind turbine design tools. *The twenty-first international offshore and polar engineering conference*. OnePetro. 2011
27. Lupton R. Frequency-domain modelling of floating wind turbines. PhD thesis. University of Cambridge, 2015
28. Leimeister M, Kolios A and Collu M. Development and verification of an aero-hydro-servo-elastic coupled model of dynamics for FOWT, based on the MoWiT library. Energies 2020; 13:1974

29. Jonkman JM, Buhl Jr ML et al. FAST user's guide. Golden, CO: National Renewable Energy Laboratory 2005; 365:366
30. SINTEF. SIMO 4.10. 3 User Guide. 2017
31. SINTEF. RIFLEX 4.10. 3 User Guide. 2017
32. Kvittem MI, Moan T, Gao Z and Luan C. Short-term fatigue analysis of semi-submersible wind turbine tower. *International Conference on Offshore Mechanics and Arctic Engineering*. Vol. 44342. 2011 :751–9
33. Hansen M. Aerodynamics of wind turbines. Routledge, 2015
34. Snel H and Schepers J. Joint investigation of dynamic inflow effects and implementation of an engineering method. 1995
35. Chakrabarti SK. Hydrodynamics of offshore structures. WIT press, 1987
36. Faltinsen O. Sea loads on ships and offshore structures. Vol. 1. Cambridge university press, 1993
37. Lee CH and Newman JN. Wamit user manual. WAMIT, Inc 2006
38. Lee CH. Theory Manual. WAMIT, Inc 1995
39. DNV. Recommended practice DNV-RP-C205: environmental conditions and environmental loads. DNV, Norway 2014
40. DNV. DNVGL-RP-C203: Fatigue design of offshore steel structures. DNV GL, Oslo, Norway 2016
41. Rychlik I. A new definition of the rainflow cycle counting method. International journal of fatigue 1987; 9:119–21
42. WAFO-group. WAFO - A Matlab Toolbox for Analysis of Random Waves and Loads - A Tutorial. Math. Stat., Center for Math. Sci., Lund Univ. Lund, Sweden, 2000
43. Gaertner E, Rinker J, Sethuraman L, Zahle F, Anderson B, Barter G, Abbas N, Meng F, Bortolotti P, Skrzypinski W, Scott G, Feil R, Bredmose H, Dykes K, Sheilds M, Allen C and Viselli A. Definition of the IEA 15-Megawatt Offshore Reference Wind Turbine. Tech. rep. International Energy Agency, 2020
44. Li L, Gao Z and Moan T. Joint distribution of environmental condition at five european offshore sites for design of combined wind and wave energy devices. Journal of Offshore Mechanics and Arctic Engineering 2015; 137
45. IEC. Design requirements for offshore wind turbines. IEC 61400 2006; 3
46. DNV. Sesam User Manual-GeniE. DNV GL Software 2016
47. DNV. Sesam User Manual-HydroD. DNV GL Software 2013
48. Jonkman BJ. TurbSim user's guide: Version 1.50. Tech. rep. National Renewable Energy Lab.(NREL), Golden, CO (United States), 2009
49. DNV. Recommended practice DNV-RP-C103, Column-Stabilised Units. Hovik, Norway 2012

Appendix A

Hydrodynamic Results

The main output from HydroD that is going to be used for the next-stage work includes the radiation and diffraction forces. The Figure A.1 shows the total frequency dependent added mass and radiation damping of the body.

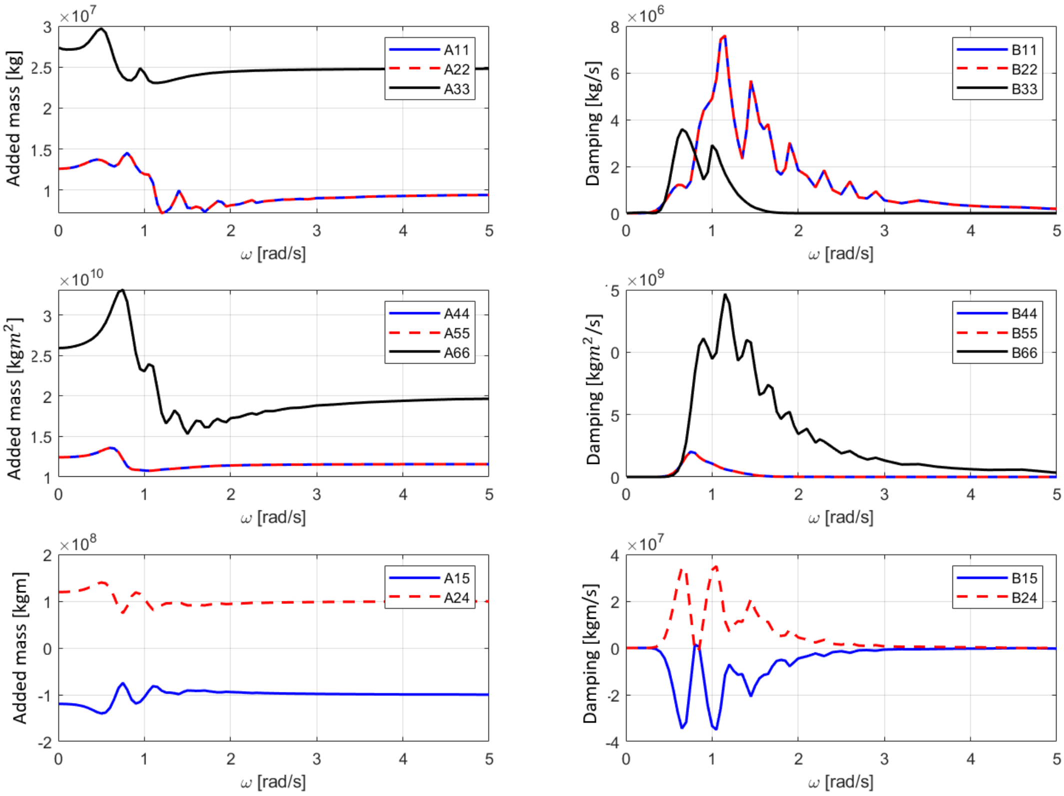

Figure A.1: Added mass and radiation damping computed from HydroD.

The Figure A.2 demonstrates the excitation force amplitude in 11 directions. The 0^o wave gives highest excitation force for surge, heave and pitch motions. It gives zero excitation for sway, roll and yaw motions. The 90^o wave provides the highest excitation for sway and roll motions. The wave in 30^o,90^o and 150^o direction generated the same amplitude of excitation force for the yaw motion. This can be expected due to the angle of 120^o between pontoons. The wave in these three directions gives the same-amplitude torque to let the body spin along the z axis.

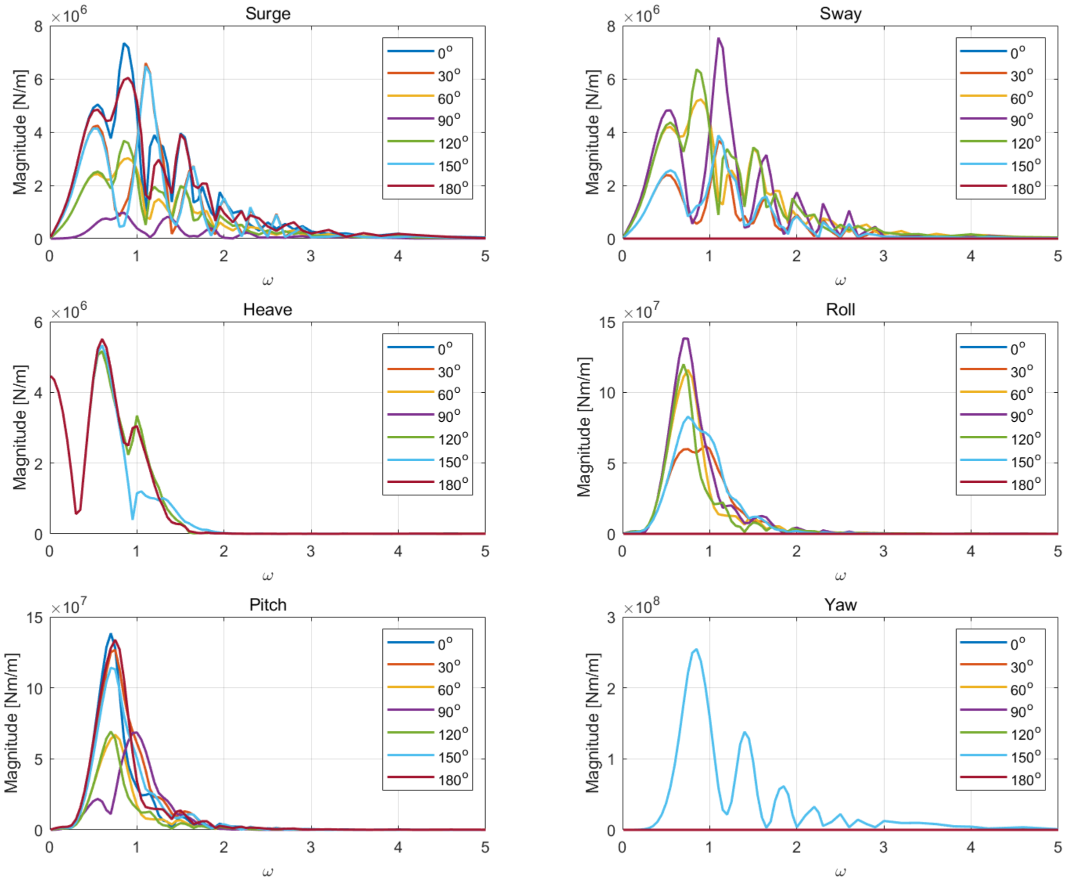

Figure A.2: Excitation force amplitude of unit wave elevation computed from HydroD.

Appendix B

Multi-body Hydrodynamic Code

The self-developed code is attached in this Appendix, which is employed to definr the sub-bodies and integrate panel pressure. The computed output includes added mass, damping coefficients and transfer functions of excitation. The main function is given as below.

```
%-----------------------
% MAIN                 !
%-----------------------
close all
clear all
clc
tic
set(0,'defaultfigurecolor','w')
format long
%% output and input
Kfile = '';
K_info = load(Kfile);

prefix = 'semi';
folder = '';
folderout='semi_out\';
            % output
mode_out = 6; % 3 for potential flow library, 6 for SIMO body way. model for output


%% Read WAMIT output
datGDF = dlmread([folder prefix '.GDF'],'',1,0);    % geometric data file
datpnl = dlmread([folder prefix '.pnl']);           % panel data file
dat1 = dlmread([folder prefix '.1']);  % added mass and damping coefficients
dat2 = dlmread([folder prefix '.2']);% exciting forces from Haskind relations
dat3 = dlmread([folder prefix '.3']); % exciting forces from diffraction potential
dat5p = dlmread([folder prefix '.5p']);% Hydrodynamic pressure on body surface

%% Define basic parameters
ULEN = datGDF(1,1);
g = datGDF(1,2);
XV = datGDF(4:end,1);
YV = datGDF(4:end,2);
ZV = datGDF(4:end,3);

```

```
Mpnl = datpnl(:,1);
Kpnl = datpnl(:,2);
XCT = datpnl(:,3);  % x coordinate of panels
YCT = datpnl(:,4);  % y coordinate of panels
ZCT = datpnl(:,5);  % z coordinate of panels
AREA = datpnl(:,6);
nx = datpnl(:,7);
ny = datpnl(:,8);
nz = datpnl(:,9);
nrx = datpnl(:,10);
nry = datpnl(:,11);
nrz = datpnl(:,12);


pers = flipud(unique(dat5p(:,1)));
Npers = length(pers);                       % number of periods
Npanels = length(Kpnl);                     % number of panels
Nbetas = length(unique(dat3(:,2)));         % number of wave headings
betas = unique(dat5p(Npanels+1:Npanels+Npanels*Nbetas,2));
omega = 2*pi./pers;
rho = 1025;
L = ULEN;

x0=0; %Position of new local coordinate system
y0=0; %Position of new local coordinate system

%% Split TLP into column, base node (lower column) and (indivdual) pontoons
heightC = 13.0;               % upper column length (under water)
heightPon = 7;
lengthP = 51.75;

radC_c = 10/2;                  % central column diameter
radC_s = 12.5/2;                % side column diameter
radBN = radC_c + 5;           % start section to cut pontoons
draft = min(ZCT);               % semi-sub draft
lengthBN = -draft-heightC;      % Base Node means BN
Zs = draft+8.5*0.5;             % spokes centerline in z, shouled be -

crd_Semi = [XCT YCT ZCT];             % all panel center coordinates Semi

pnl_C = find( sqrt(crd_Semi(:,1).^2 + crd_Semi(:,2).^2) <= radC_c & crd_Semi(:,3)>-heightC );
crd_C = crd_Semi(pnl_C,:);            % panel coordinates central column, x y z all

pnl_Cs1 = find( sqrt(crd_Semi(:,1).^2 + crd_Semi(:,2).^2) > radC_c & crd_Semi(:,3) >
-heightC & crd_Semi(:,1) > 0 );
crd_Cs1 = crd_Semi(pnl_Cs1 ,:);       % panel coordinates side column 1
pnl_Cs2 = find( sqrt(crd_Semi(:,1).^2 + crd_Semi(:,2).^2) > radC_c & crd_Semi(:,3) >
-heightC & crd_Semi(:,2) > 0 & crd_Semi(:,1) < 0 );
crd_Cs2 = crd_Semi(pnl_Cs2 ,:);       % panel coordinates side column 2
pnl_Cs3 = find( sqrt(crd_Semi(:,1).^2 + crd_Semi(:,2).^2) > radC_c & crd_Semi(:,3) >
-heightC & crd_Semi(:,2) < 0 & crd_Semi(:,1) < 0 );
crd_Cs3 = crd_Semi(pnl_Cs3 ,:);       % panel coordinates side column 3

pnl_P1 = find(  crd_Semi(:,3) <= -heightC & crd_Semi(:,1) > 4  &
sqrt(crd_Semi(:,1).^2 + crd_Semi(:,2).^2) > radBN);   % x positive,
crd_P1 = crd_Semi(pnl_P1,:);          % panel coordinates pontoon 1
pnl_P2 = find(  crd_Semi(:,3) <= -heightC & crd_Semi(:,2) > 0 &
crd_Semi(:,1) < 4  & sqrt(crd_Semi(:,1).^2 + crd_Semi(:,2).^2) > radBN);
crd_P2 = crd_Semi(pnl_P2,:);          % panel coordinates pontoon 2
pnl_P3 = find(  crd_Semi(:,3) <= -heightC & crd_Semi(:,2) < 0 &
```

```
crd_Semi(:,1) < 4  & sqrt(crd_Semi(:,1).^2 + crd_Semi(:,2).^2) > radBN);
crd_P3 = crd_Semi(pnl_P3,:);         % panel coordinates pontoon 3 % z+ r + xy

pnl_BN = find( sqrt(crd_Semi(:,1).^2 + crd_Semi(:,2).^2) <= radBN  &
crd_Semi(:,3) <= -heightC);
crd_BN = crd_Semi(pnl_BN,:);           % panel coordinates central column, x y z all
% here, all panels are included. no missing, checked, correct
n_should =[length(pnl_C);length(pnl_Cs1); length(pnl_Cs2),; length(pnl_Cs3);
length(pnl_P1); length(pnl_P2); length(pnl_P3); length(pnl_BN)];
if Npanels ==sum(n_should)
   disp('all panels are included. no missing, checked, correct');
else
    disp('Not all panels are included. no missing, checked, incorrect');
end

%% Define multi-body model
Ndl = 5;
idl = input('mode of sections divided == ');
if idl == 1
    NN = 16;
elseif idl == 2
    NN = 12;
elseif idl == 3
    NN = 8;
elseif idl == 4
    NN = 4;
elseif idl == 5
    NN = 2;
elseif idl == 6
    NN = 1;
elseif idl == 7
    NN = 3;
end

NsectionC = NN;    % number of section of Upper Column.
NsectionBN = 1;   % number of section.
NsectionP = NN;    % number of section.

d1 = heightC/NsectionC;  %length of individual section
d2 = lengthBN/NsectionBN;
%--------------------------------------------------------------------------
% columns from low to top, the boundary of each section, not the center
zC = linspace(-heightC,0,NsectionC+1)';
xC = zeros(size(zC)); % node x-locations on column
yC = zeros(size(zC)); % node y-locations on column
SecC = [xC yC zC];
% side columns  1 is along the x positive, 2 is in the 2nd qudarant. 3 is in 3rd.
zCs1 = zC ; zCs2 = zC ; zCs3 = zC ;
xCs1 = ones(size(zC))*lengthP;  xCs2 = ones(size(zC))*lengthP *(- cosd(60));
xCs3 = ones(size(zC))*lengthP *(- cosd(60));
yCs1 = zeros(size(zC));         yCs2 = ones(size(zC))*lengthP *(sind(60));
yCs3 = ones(size(zC))*lengthP *(- sind(60));
SecCs1 = [xCs1 yCs1 zCs1]; SecCs2 = [xCs2 yCs2 zCs2]; SecCs3 = [xCs3 yCs3 zCs3];
% pontoon 1 is along the x positive, 2 is in the 2nd qudarant. 3 is in 3rd.
xP1 = linspace(radBN,radC_s+lengthP,NsectionP+1)';
% from column surface to tip. mesh number is 30 (29.7).
if idl == 7
     xP1 = [10, 25, 40, 58]';
end
yP1 = zeros(size(xP1));                 % node y-locations on pontoon 1  1st
```

```
zP1 = Zs*ones(size(xP1));               % node z-locations on pontoon 1
xP2 = -cosd(60)*xP1;                    % node x-locations on pontoon 2
yP2 = cosd(30)*xP1;                     % node y-locations on pontoon 2, 2nd qudarant
zP2 = Zs*ones(size(yP2));               % node z-locations on pontoon 2
xP3 = xP2;                              % node x-locations on pontoon 3
yP3 = -yP2;                             % node y-locations on pontoon 3  3rd
zP3 = zP2;                              % node z-locations on pontoon 3
% Base node which is below central column
zBN = linspace(draft,-heightC,NsectionBN+1)';
xBN = zeros(size(zBN)); % node x-locations on column
yBN = zeros(size(zBN)); % node y-locations on column
SecP1 = [xP1 yP1 zP1]; SecP2 = [xP2 yP2 zP2]; SecP3 = [xP3 yP3 zP3];
Secs = [SecC; SecCs1; SecCs2; SecCs3; SecP1; SecP2; SecP3];
%---------objectives-----------------------
% SecC, SecCs1, SecCs2, SecCs3
% SecP1, SecP2, SecP3
% Secs
%--------------------------------------------------------------------------------
%--------------------------------------------------------------------------------
% node, middle of section
% central column
zCn = zC - 0.5*d1*ones(size(zC));
zCn = zCn(2:end);
xCn = zeros(size(zCn));
yCn = zeros(size(zCn));
nodesC = [xCn yCn zCn];
NnodesC = size(nodesC,1);
% side column
zCsn1 = zCn ; zCsn2 = zCn ; zCsn3 = zCn ;
xCsn1 = ones(size(zCn))*lengthP;
xCsn2 = ones(size(zCn))*lengthP *(- cosd(60));
xCsn3 = ones(size(zCn))*lengthP *(- cosd(60));

yCsn1 = zeros(size(zCn));
yCsn2 = ones(size(zCn))*lengthP *(sind(60));
yCsn3 = ones(size(zCn))*lengthP *(- sind(60));
nodesCs1 = [xCsn1 yCsn1 zCsn1];
nodesCs2 =[xCsn2 yCsn2 zCsn2];
nodesCs3 =[xCsn3 yCsn3 zCsn3];
nodesCs = [nodesCs1;nodesCs2;nodesCs3];
NnodesCs1 = size(nodesC,1);
NnodesCs2 = size(nodesC,1);
NnodesCs3 = size(nodesC,1);
% pontoon1
xP1n = xP1 - 0.5*(lengthP/NsectionP)*ones(size(xP1));
xP1n = xP1n(2:end);
yP1n = zeros(size(xP1n));
zP1n = Zs*ones(size(xP1n));
nodesP1 = [xP1n yP1n zP1n];   NnodesP1 = size(nodesP1,1);
% pontoon2 and 3
xP2n = -cosd(60)*xP1n;
yP2n = cosd(30)*xP1n;
zP2n = Zs*ones(size(yP2n));
xP3n = xP2n;
yP3n = -yP2n;
zP3n = zP2n;
nodesP2 = [xP2n yP2n zP2n];   NnodesP2 = size(nodesP2,1);
nodesP3 = [xP3n yP3n zP3n];   NnodesP3 = size(nodesP3,1);
% central Base Node
zBNn = zBN - 0.5*d2*ones(size(zBN));
```

```
zBNn = zBNn(2:end);
xBNn = zeros(size(zBNn));
yBNn = zeros(size(zBNn));
nodesBN =[xBNn yBNn zBNn];    NnodesBN = size(nodesBN,1);
%------------------------------------------------------------------
nodes = [nodesC; nodesCs1; nodesCs2; nodesCs3;
         nodesP1; nodesP2; nodesP3; nodesBN];
Nnodes = [length(nodes), NnodesC, NnodesCs1, NnodesCs2, NnodesCs3,
          NnodesP1, NnodesP2, NnodesP3, NnodesBN] ;
%-----------------------------------------------------------------

%---------objectives-------------------
% nodesC, nodesCs1, nodesCs2, nodesCs3
% nodesP1, nodesP2, nodesP3
% nodes
% ------------------------------------
%% Generate SIMO body input for A, B and F from radiation and diffraction pressures
% Now we defined 7 substructures, 4 columns and 3 pontoons
Nbody = 8;
AB = cell(Nbody,1);
F = cell(Nbody,1);
Buoy = cell(Nbody,1);
ZBuoy = cell(Nbody,1);
C = cell(Nbody,1);
K = cell(Nbody,1);
for i =1:Nbody
    AB{i} = zeros(Npers,Nnodes(i+1),6,6);
    F{i} = zeros(Npers,Nbetas,Nnodes(i+1),6);
    Buoy{i} = zeros(Npers,Nnodes(i+1),6);
    ZBuoy{i} = zeros(Nnodes(i+1));
    C{i} = zeros(Npers,Nnodes(i+1),6,6);
end
Lm = [L^2 L^2 L^2 L^3 L^3 L^3]; % m for force. n and k for pressure and radiation coefficient.
Lkn = [L^-3 L^-3 L^-3 L^-4 L^-4 L^-4]; % for radiation. L k-n, see 6.18 equation. correct.
count = 0;
n = zeros(Nbody,1);
for iper = 1:Npers   % number of periods , in total 60
    n = zeros(Nbody,1);
    for i =1:Nbody
        K{i} = zeros(Nnodes(i+1),6,6);
    end
    disp(['Run calculation period ' num2str(pers(iper))])
    % loop, panels and separate. 2 seciton node. 3 beta for force
    for ipnl = 1:Npanels                    % loop through panels, all panels. this is panel number
        count = count + 1;                  % extract 5p file data. see below
        norm = [nx(ipnl), ny(ipnl), nz(ipnl), nrx(ipnl), nry(ipnl), nrz(ipnl)]; % normal direction
        area = AREA(ipnl);                     % panel area
       % Classify panels into different substructures and sections
       %---------------------------------------------------------------------
        if any(pnl_C==ipnl)        % central column sequence
            [F{1}, AB{1}, Buoy{1}, ZBuoy{1}, C{1}, K{1}, n(1)] =
            Integration_Column(F{1},AB{1},Buoy{1},ZBuoy{1},C{1},K{1},K_info,Nnodes(2),
            ipnl,XCT,YCT,ZCT,zC,dat5p,norm,n(1),count,Lkn,area,g,omega,iper,Nbetas,Npanels,Lm);
        elseif any(pnl_Cs1==ipnl)  % side column 1 sequence
            [F{2}, AB{2}, Buoy{2}, ZBuoy{2}, C{2}, K{2}, n(2)] =
            Integration_Column(F{2},AB{2},Buoy{2},ZBuoy{2},C{2},K{2},K_info,Nnodes(3),
            ipnl,XCT,YCT,ZCT,zC,dat5p,norm,n(2),count,Lkn,area,g,omega,iper,Nbetas,Npanels,Lm);
        elseif any(pnl_Cs2==ipnl)  % side column 2 sequence
            [F{3}, AB{3}, Buoy{3}, ZBuoy{3}, C{3}, K{3}, n(3)] =
            Integration_Column(F{3},AB{3},Buoy{3},ZBuoy{3},C{3},K{3},K_info,Nnodes(4),
```

```
            ipnl,XCT,YCT,ZCT,zC,dat5p,norm,n(3),count,Lkn,area,g,omega,iper,Nbetas,Npanels,Lm);
        elseif any(pnl_Cs3==ipnl)  % side column 3 sequence
            [F{4}, AB{4}, Buoy{4}, ZBuoy{4}, C{4}, K{4}, n(4)] =
            Integration_Column(F{4},AB{4},Buoy{4},ZBuoy{4},C{4},K{4},K_info,Nnodes(5),
            ipnl,XCT,YCT,ZCT,zC,dat5p,norm,n(4),count,Lkn,area,g,omega,iper,Nbetas,Npanels,Lm);
        elseif any(pnl_P1==ipnl)
            [F{5}, AB{5}, Buoy{5}, ZBuoy{5}, C{5}, K{5}, n(5)] =
            Integration_Pontoon(F{5},AB{5},Buoy{5},ZBuoy{5},C{5},K{5},K_info,Nnodes(6),
            ipnl,XCT,YCT,ZCT,xP1,yP1,dat5p,norm,n(5),count,Lkn,area,g,omega,iper,Nbetas,Npanels,Lm);
        elseif any(pnl_P2==ipnl)
            [F{6}, AB{6}, Buoy{6}, ZBuoy{6}, C{6}, K{6}, n(6)] =
            Integration_Pontoon(F{6},AB{6},Buoy{6},ZBuoy{6},C{6},K{6},K_info,Nnodes(7),
            ipnl,XCT,YCT,ZCT,xP2,yP2,dat5p,norm,n(6),count,Lkn,area,g,omega,iper,Nbetas,Npanels,Lm);
        elseif any(pnl_P3==ipnl)
            [F{7}, AB{7}, Buoy{7}, ZBuoy{7}, C{7}, K{7}, n(7)] =
            Integration_Pontoon(F{7},AB{7},Buoy{7},ZBuoy{7},C{7},K{7},K_info,Nnodes(8),
            ipnl,XCT,YCT,ZCT,xP3,yP3,dat5p,norm,n(7),count,Lkn,area,g,omega,iper,Nbetas,Npanels,Lm);
        elseif any(pnl_BN==ipnl)
            [F{8}, AB{8}, Buoy{8}, ZBuoy{8}, C{8}, K{8}, n(8)] =
            Integration_BN(F{8},AB{8},Buoy{8},ZBuoy{8},C{8},K{8},K_info,Nnodes(9),
            ipnl,XCT,YCT,ZCT,zBN,dat5p,norm,n(8),count,Lkn,area,g,omega,iper,Nbetas,Npanels,Lm);
        end
       %----------------------------------------------------------------------

    end
     % each pers, have these panels
    count = count + Npanels*Nbetas;
end
if sum(n) == Npanels
    disp('all the pressure on panels are integrated');
else
    disp('there is some panel not integrated ! ! !');
end
```

This function is used for integrating the diffraction and radiation terms of the columns.

```
function [F, AB, Buoy, n] = Integration_Column(Fin, ABin, Buoyin,
                                               Nnodes, ipnl,ZCT, zC, ...
                                               dat5p, norm, n, count, ...
                                               Lkn, AREA, g, ...
                                               omega, iper, Nbetas, Npanels, Lm)

 F = Fin;
 AB = ABin;
 Buoy = Buoyin;
 heightC = 13;
 rho = 1025;
    for inode = 1:Nnodes
    % from low to up, both the upper column and lower column

       if ZCT(ipnl) > zC(inode) && ZCT(ipnl) <= zC(inode+1)
          % panel center between two node of section
          %Calculate added mass and damping matrix from radiation presssure
          %p = pressure(dat5p,count);
          p1 = dat5p(count,4)+1i*dat5p(count,5);
          p2 = dat5p(count,6)+1i*dat5p(count,7);
```

```
          p3 = dat5p(count,8)+1i*dat5p(count,9);
          p = [p1 p2 p3 0 0 0];
          clear p1 p2 p3
          rn = [0, 0, 0];                 % Set the rotational forces to 0.
          nrn = ([norm rn].*Lkn)';

          % 1. Added mass and Damping
          ABpan = nrn*p*AREA*g/(omega(iper))^2;
          AB(iper,inode,:,:) = squeeze(AB(iper,inode,:,:)) + ABpan;
          n = n+1;

          % 2. Exicatation of different wave directions
          for ibet = 1:Nbetas
              f = dat5p(count+Npanels*ibet,5) + 1i*dat5p(count+Npanels*ibet,6);
              Fpan = AREA./Lm.*[norm rn]*f;
              clear f
              F(iper,ibet,inode,1) = Fpan(1) + F(iper,ibet,inode,1);  %Fx
              F(iper,ibet,inode,2) = Fpan(2) + F(iper,ibet,inode,2);  %Fy
              F(iper,ibet,inode,3) = Fpan(3) + F(iper,ibet,inode,3);  %Fz
              F(iper,ibet,inode,4) = 0;
              F(iper,ibet,inode,5) = 0;
              F(iper,ibet,inode,6) = 0;
          end

           % 3. Buoy contributed by vertical pressure
           Buoy(iper,inode) =  Buoy(iper,inode) +
                               norm(3) * AREA * rho * g * (-ZCT(ipnl));
       end
    end
```

This function is used for integrating the diffraction and radiation terms of the pontoon.

```
function [F, AB, Buoy, n] = Integration_Pontoon(Fin, ABin, Buoyin, Nnodes,
                                ipnl, XCT, YCT, ZCT, xP, yP, ...
                               dat5p, norm, n, count, Lkn, AREA, g, ...
                               omega, iper, Nbetas, Npanels, Lm, lengthP)
 F = Fin;
 AB = ABin;
 Buoy = Buoyin;
 rho = 1025;
 radC = 5;
    for inode = 1:Nnodes
    % from low to up, both the upper column and lower column
       lim1 = sqrt(xP(inode)^2 + yP(inode)^2);
       if inode == 1
           lim1 = 0;
       end
       lim2 = sqrt(xP(inode+1)^2 + yP(inode+1)^2);
       % take the right boundary panels
       if sqrt(XCT(ipnl)^2 + YCT(ipnl)^2 ) > lim1 && ...
               sqrt(XCT(ipnl)^2 + YCT(ipnl)^2 ) <= lim2
               % panel center between two node of section
          %Calculate added mass and damping matrix from radiation presssure
          %p = pressure(dat5p,count);
          p1 = dat5p(count,4)+1i*dat5p(count,5);
          p2 = dat5p(count,6)+1i*dat5p(count,7);
```

```
          p3 = dat5p(count,8)+1i*dat5p(count,9);
          p = [p1 p2 p3 0 0 0];
          clear p1 p2 p3
          rn = [0, 0, 0];
          % Set the rotational forces to 0.
          nrn = ([norm rn].*Lkn)';

          % 1. Added mass and Damping
          ABpan = nrn*p*AREA*g/(omega(iper))^2;
          AB(iper,inode,:,:) = squeeze(AB(iper,inode,:,:)) + ABpan;
          n = n + 1;
          % 2. Exicatation of different wave directions
          for ibet = 1:Nbetas
              f = dat5p(count+Npanels*ibet,5) + 1i*dat5p(count+Npanels*ibet,6);
              Fpan = AREA./Lm.*[norm rn]*f;
              clear f
              F(iper,ibet,inode,1) = Fpan(1) + F(iper,ibet,inode,1);  %Fx
              F(iper,ibet,inode,2) = Fpan(2) + F(iper,ibet,inode,2);  %Fy
              F(iper,ibet,inode,3) = Fpan(3) + F(iper,ibet,inode,3);  %Fz
              F(iper,ibet,inode,4) = 0;
              F(iper,ibet,inode,5) = 0;
              F(iper,ibet,inode,6) = 0;

          end
          % 3. Buoy contributed by vertical pressure
          Buoy(iper,inode) =  Buoy(iper,inode) +
                              norm(3) * AREA * rho *g * (-ZCT(ipnl));
       end
       end
    end
```

Appendix C

Scatter Diagrams of Site 14

The scatter diagrams of the selected site are presented in this appendix. The cases that has probability lower than 1e-4 are neglected.

- The wind speed ranges from 4 m/s to 24 m/s, of which the bin size is 2 m/s
- The significant wave height ranges from 0 m to 9 m, of which the bin size is 0.5 m
- The wave period ranges from from 4 s to 16 s, of which the bin size is 1 s

The scatter diagrams are used to identify the cases for time domain simulations.

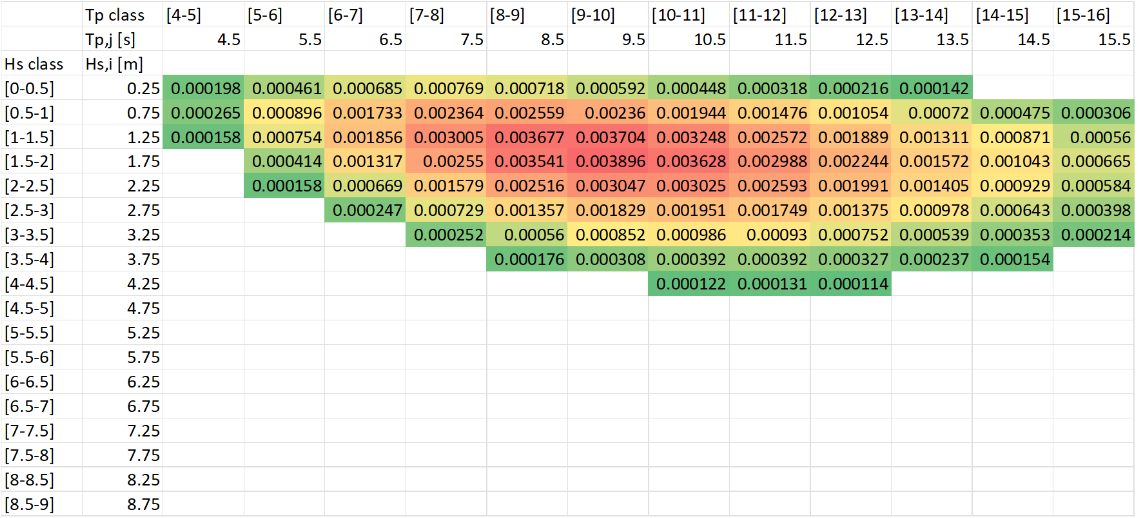

	Tp class	[4-5]	[5-6]	[6-7]	[7-8]	[8-9]	[9-10]	[10-11]	[11-12]	[12-13]	[13-14]	[14-15]	[15-16]
	Tp,j [s]	4.5	5.5	6.5	7.5	8.5	9.5	10.5	11.5	12.5	13.5	14.5	15.5
Hs class	Hs,i [m]												
[0-0.5]	0.25	0.000198	0.000461	0.000685	0.000769	0.000718	0.000592	0.000448	0.000318	0.000216	0.000142		
[0.5-1]	0.75	0.000265	0.000896	0.001733	0.002364	0.002559	0.00236	0.001944	0.001476	0.001054	0.00072	0.000475	0.000306
[1-1.5]	1.25	0.000158	0.000754	0.001856	0.003005	0.003677	0.003704	0.003248	0.002572	0.001889	0.001311	0.000871	0.00056
[1.5-2]	1.75		0.000414	0.001317	0.00255	0.003541	0.003896	0.003628	0.002988	0.002244	0.001572	0.001043	0.000665
[2-2.5]	2.25		0.000158	0.000669	0.001579	0.002516	0.003047	0.003025	0.002593	0.001991	0.001405	0.000929	0.000584
[2.5-3]	2.75			0.000247	0.000729	0.001357	0.001829	0.001951	0.001749	0.001375	0.000978	0.000643	0.000398
[3-3.5]	3.25				0.000252	0.00056	0.000852	0.000986	0.00093	0.000752	0.000539	0.000353	0.000214
[3.5-4]	3.75					0.000176	0.000308	0.000392	0.000392	0.000327	0.000237	0.000154	
[4-4.5]	4.25							0.000122	0.000131	0.000114			
[4.5-5]	4.75												
[5-5.5]	5.25												
[5.5-6]	5.75												
[6-6.5]	6.25												
[6.5-7]	6.75												
[7-7.5]	7.25												
[7.5-8]	7.75												
[8-8.5]	8.25												
[8.5-9]	8.75												

Figure C.1: Example of scatter diagram of joint probability distribution [$U_w = 4\,\mathrm{m/s}$].

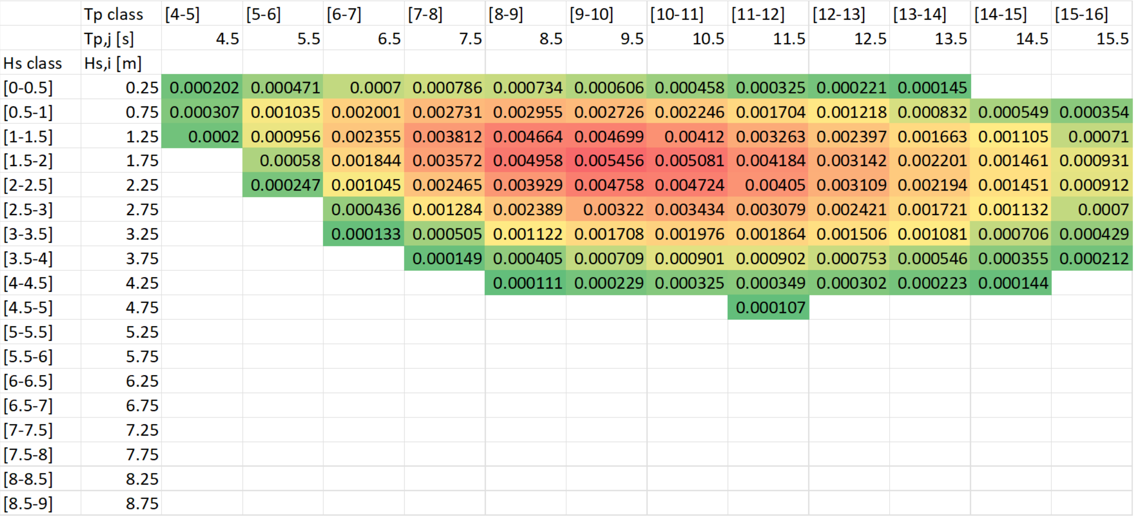

	Tp class	[4-5]	[5-6]	[6-7]	[7-8]	[8-9]	[9-10]	[10-11]	[11-12]	[12-13]	[13-14]	[14-15]	[15-16]
	Tp,j [s]	4.5	5.5	6.5	7.5	8.5	9.5	10.5	11.5	12.5	13.5	14.5	15.5
Hs class	Hs,i [m]												
[0-0.5]	0.25	0.000202	0.000471	0.0007	0.000786	0.000734	0.000606	0.000458	0.000325	0.000221	0.000145		
[0.5-1]	0.75	0.000307	0.001035	0.002001	0.002731	0.002955	0.002726	0.002246	0.001704	0.001218	0.000832	0.000549	0.000354
[1-1.5]	1.25	0.0002	0.000956	0.002355	0.003812	0.004664	0.004699	0.00412	0.003263	0.002397	0.001663	0.001105	0.00071
[1.5-2]	1.75		0.00058	0.001844	0.003572	0.004958	0.005456	0.005081	0.004184	0.003142	0.002201	0.001461	0.000931
[2-2.5]	2.25		0.000247	0.001045	0.002465	0.003929	0.004758	0.004724	0.00405	0.003109	0.002194	0.001451	0.000912
[2.5-3]	2.75			0.000436	0.001284	0.002389	0.00322	0.003434	0.003079	0.002421	0.001721	0.001132	0.0007
[3-3.5]	3.25			0.000133	0.000505	0.001122	0.001708	0.001976	0.001864	0.001506	0.001081	0.000706	0.000429
[3.5-4]	3.75				0.000149	0.000405	0.000709	0.000901	0.000902	0.000753	0.000546	0.000355	0.000212
[4-4.5]	4.25					0.000111	0.000229	0.000325	0.000349	0.000302	0.000223	0.000144	
[4.5-5]	4.75								0.000107				
[5-5.5]	5.25												
[5.5-6]	5.75												
[6-6.5]	6.25												
[6.5-7]	6.75												
[7-7.5]	7.25												
[7.5-8]	7.75												
[8-8.5]	8.25												
[8.5-9]	8.75												

Figure C.2: Example of scatter diagram of joint probability distribution [$U_w = 6\,\mathrm{m/s}$].

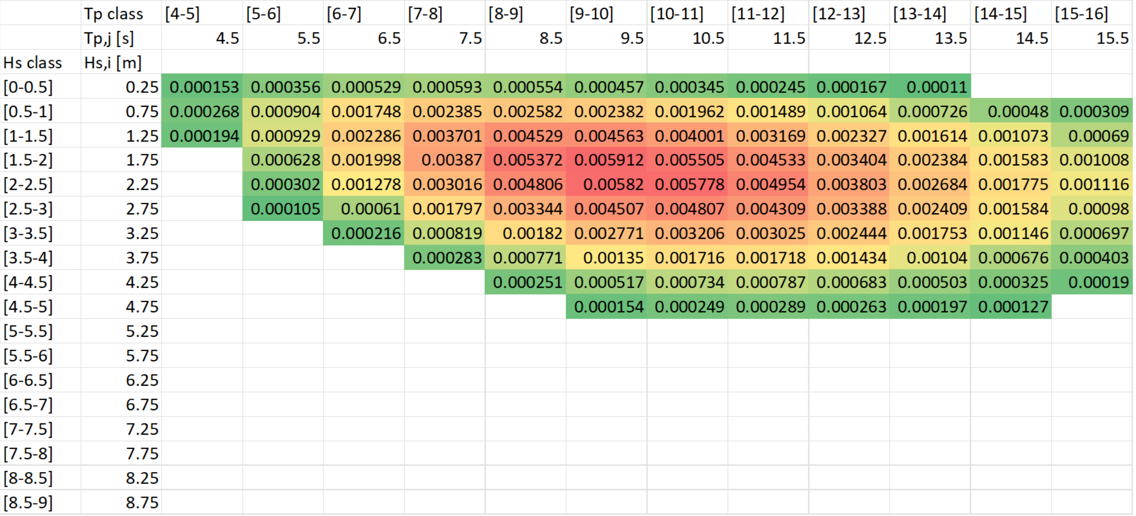

	Tp class	[4-5]	[5-6]	[6-7]	[7-8]	[8-9]	[9-10]	[10-11]	[11-12]	[12-13]	[13-14]	[14-15]	[15-16]
	Tp,j [s]	4.5	5.5	6.5	7.5	8.5	9.5	10.5	11.5	12.5	13.5	14.5	15.5
Hs class	Hs,i [m]												
[0-0.5]	0.25	0.000153	0.000356	0.000529	0.000593	0.000554	0.000457	0.000345	0.000245	0.000167	0.00011		
[0.5-1]	0.75	0.000268	0.000904	0.001748	0.002385	0.002582	0.002382	0.001962	0.001489	0.001064	0.000726	0.00048	0.000309
[1-1.5]	1.25	0.000194	0.000929	0.002286	0.003701	0.004529	0.004563	0.004001	0.003169	0.002327	0.001614	0.001073	0.00069
[1.5-2]	1.75		0.000628	0.001998	0.00387	0.005372	0.005912	0.005505	0.004533	0.003404	0.002384	0.001583	0.001008
[2-2.5]	2.25		0.000302	0.001278	0.003016	0.004806	0.00582	0.005778	0.004954	0.003803	0.002684	0.001775	0.001116
[2.5-3]	2.75		0.000105	0.00061	0.001797	0.003344	0.004507	0.004807	0.004309	0.003388	0.002409	0.001584	0.00098
[3-3.5]	3.25			0.000216	0.000819	0.00182	0.002771	0.003206	0.003025	0.002444	0.001753	0.001146	0.000697
[3.5-4]	3.75				0.000283	0.000771	0.00135	0.001716	0.001718	0.001434	0.00104	0.000676	0.000403
[4-4.5]	4.25					0.000251	0.000517	0.000734	0.000787	0.000683	0.000503	0.000325	0.00019
[4.5-5]	4.75						0.000154	0.000249	0.000289	0.000263	0.000197	0.000127	
[5-5.5]	5.25												
[5.5-6]	5.75												
[6-6.5]	6.25												
[6.5-7]	6.75												
[7-7.5]	7.25												
[7.5-8]	7.75												
[8-8.5]	8.25												
[8.5-9]	8.75												

Figure C.3: Example of scatter diagram of joint probability distribution [$U_w = 8\,\mathrm{m/s}$].

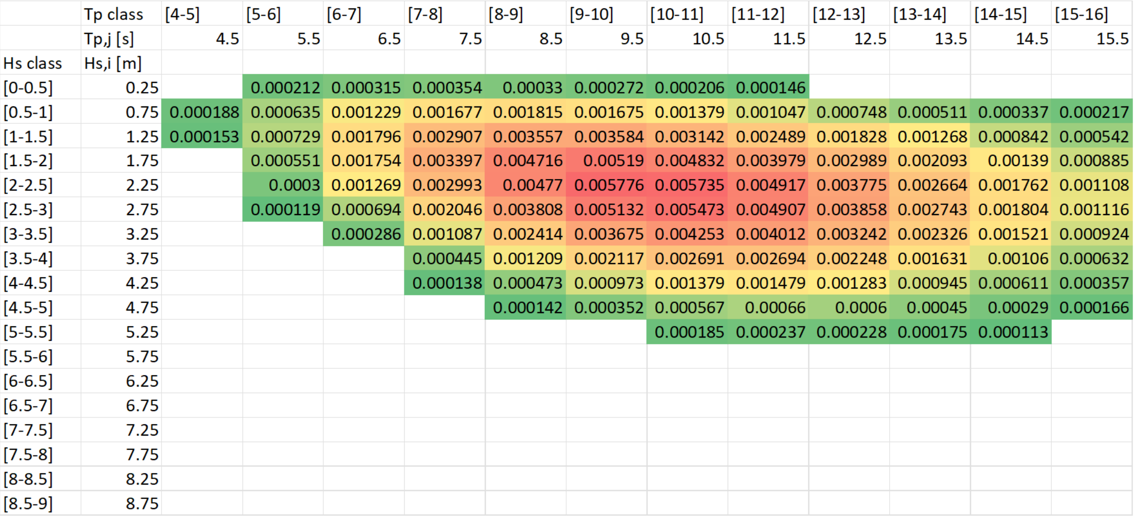

	Tp class	[4-5]	[5-6]	[6-7]	[7-8]	[8-9]	[9-10]	[10-11]	[11-12]	[12-13]	[13-14]	[14-15]	[15-16]
	Tp,j [s]	4.5	5.5	6.5	7.5	8.5	9.5	10.5	11.5	12.5	13.5	14.5	15.5
Hs class	Hs,i [m]												
[0-0.5]	0.25		0.000212	0.000315	0.000354	0.00033	0.000272	0.000206	0.000146				
[0.5-1]	0.75	0.000188	0.000635	0.001229	0.001677	0.001815	0.001675	0.001379	0.001047	0.000748	0.000511	0.000337	0.000217
[1-1.5]	1.25	0.000153	0.000729	0.001796	0.002907	0.003557	0.003584	0.003142	0.002489	0.001828	0.001268	0.000842	0.000542
[1.5-2]	1.75		0.000551	0.001754	0.003397	0.004716	0.00519	0.004832	0.003979	0.002989	0.002093	0.00139	0.000885
[2-2.5]	2.25		0.0003	0.001269	0.002993	0.00477	0.005776	0.005735	0.004917	0.003775	0.002664	0.001762	0.001108
[2.5-3]	2.75		0.000119	0.000694	0.002046	0.003808	0.005132	0.005473	0.004907	0.003858	0.002743	0.001804	0.001116
[3-3.5]	3.25			0.000286	0.001087	0.002414	0.003675	0.004253	0.004012	0.003242	0.002326	0.001521	0.000924
[3.5-4]	3.75				0.000445	0.001209	0.002117	0.002691	0.002694	0.002248	0.001631	0.00106	0.000632
[4-4.5]	4.25				0.000138	0.000473	0.000973	0.001379	0.001479	0.001283	0.000945	0.000611	0.000357
[4.5-5]	4.75					0.000142	0.000352	0.000567	0.00066	0.0006	0.00045	0.00029	0.000166
[5-5.5]	5.25							0.000185	0.000237	0.000228	0.000175	0.000113	
[5.5-6]	5.75												
[6-6.5]	6.25												
[6.5-7]	6.75												
[7-7.5]	7.25												
[7.5-8]	7.75												
[8-8.5]	8.25												
[8.5-9]	8.75												

Figure C.4: Example of scatter diagram of joint probability distribution [$U_w = 10\,\mathrm{m/s}$].

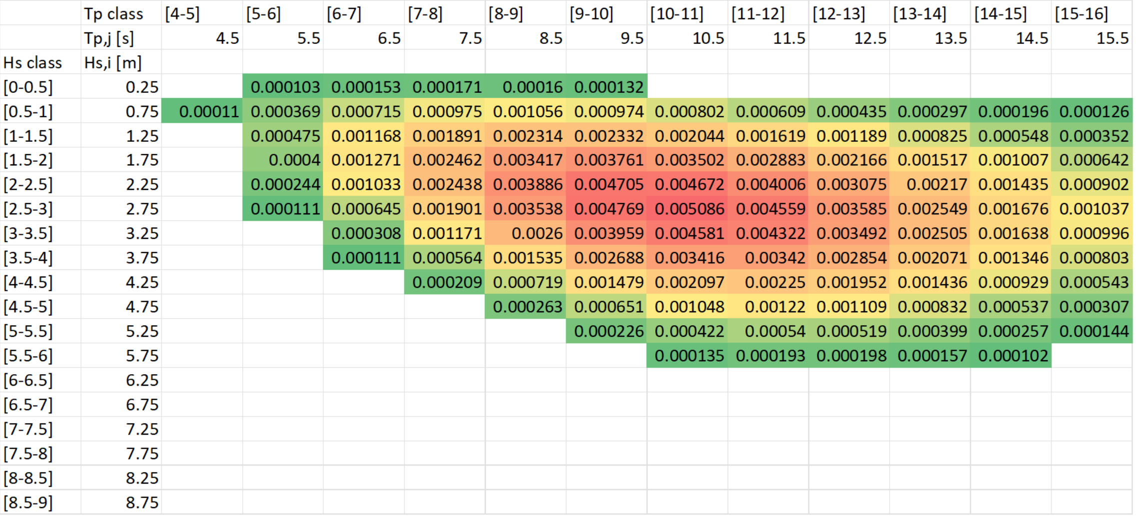

	Tp class	[4-5]	[5-6]	[6-7]	[7-8]	[8-9]	[9-10]	[10-11]	[11-12]	[12-13]	[13-14]	[14-15]	[15-16]
	Tp,j [s]	4.5	5.5	6.5	7.5	8.5	9.5	10.5	11.5	12.5	13.5	14.5	15.5
Hs class	Hs,i [m]												
[0-0.5]	0.25		0.000103	0.000153	0.000171	0.00016	0.000132						
[0.5-1]	0.75	0.00011	0.000369	0.000715	0.000975	0.001056	0.000974	0.000802	0.000609	0.000435	0.000297	0.000196	0.000126
[1-1.5]	1.25		0.000475	0.001168	0.001891	0.002314	0.002332	0.002044	0.001619	0.001189	0.000825	0.000548	0.000352
[1.5-2]	1.75		0.0004	0.001271	0.002462	0.003417	0.003761	0.003502	0.002883	0.002166	0.001517	0.001007	0.000642
[2-2.5]	2.25		0.000244	0.001033	0.002438	0.003886	0.004705	0.004672	0.004006	0.003075	0.00217	0.001435	0.000902
[2.5-3]	2.75		0.000111	0.000645	0.001901	0.003538	0.004769	0.005086	0.004559	0.003585	0.002549	0.001676	0.001037
[3-3.5]	3.25			0.000308	0.001171	0.0026	0.003959	0.004581	0.004322	0.003492	0.002505	0.001638	0.000996
[3.5-4]	3.75			0.000111	0.000564	0.001535	0.002688	0.003416	0.00342	0.002854	0.002071	0.001346	0.000803
[4-4.5]	4.25				0.000209	0.000719	0.001479	0.002097	0.00225	0.001952	0.001436	0.000929	0.000543
[4.5-5]	4.75					0.000263	0.000651	0.001048	0.00122	0.001109	0.000832	0.000537	0.000307
[5-5.5]	5.25						0.000226	0.000422	0.00054	0.000519	0.000399	0.000257	0.000144
[5.5-6]	5.75							0.000135	0.000193	0.000198	0.000157	0.000102	
[6-6.5]	6.25												
[6.5-7]	6.75												
[7-7.5]	7.25												
[7.5-8]	7.75												
[8-8.5]	8.25												
[8.5-9]	8.75												

Figure C.5: Example of scatter diagram of joint probability distribution [$U_w = 12\,\mathrm{m/s}$].

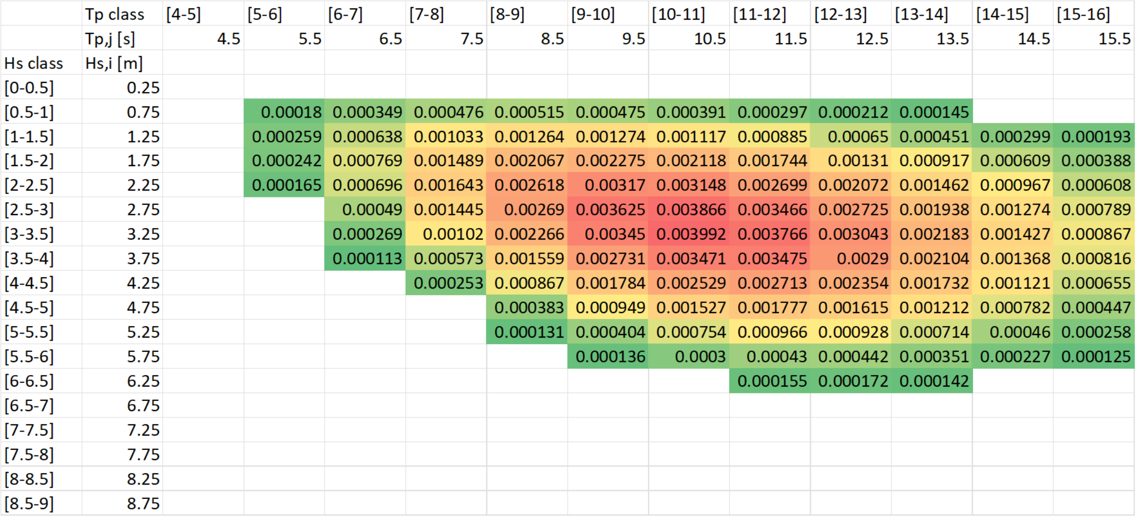

	Tp class	[4-5]	[5-6]	[6-7]	[7-8]	[8-9]	[9-10]	[10-11]	[11-12]	[12-13]	[13-14]	[14-15]	[15-16]
	Tp,j [s]	4.5	5.5	6.5	7.5	8.5	9.5	10.5	11.5	12.5	13.5	14.5	15.5
Hs class	Hs,i [m]												
[0-0.5]	0.25												
[0.5-1]	0.75		0.00018	0.000349	0.000476	0.000515	0.000475	0.000391	0.000297	0.000212	0.000145		
[1-1.5]	1.25		0.000259	0.000638	0.001033	0.001264	0.001274	0.001117	0.000885	0.00065	0.000451	0.000299	0.000193
[1.5-2]	1.75		0.000242	0.000769	0.001489	0.002067	0.002275	0.002118	0.001744	0.00131	0.000917	0.000609	0.000388
[2-2.5]	2.25		0.000165	0.000696	0.001643	0.002618	0.00317	0.003148	0.002699	0.002072	0.001462	0.000967	0.000608
[2.5-3]	2.75			0.00049	0.001445	0.00269	0.003625	0.003866	0.003466	0.002725	0.001938	0.001274	0.000789
[3-3.5]	3.25			0.000269	0.00102	0.002266	0.00345	0.003992	0.003766	0.003043	0.002183	0.001427	0.000867
[3.5-4]	3.75			0.000113	0.000573	0.001559	0.002731	0.003471	0.003475	0.0029	0.002104	0.001368	0.000816
[4-4.5]	4.25				0.000253	0.000867	0.001784	0.002529	0.002713	0.002354	0.001732	0.001121	0.000655
[4.5-5]	4.75					0.000383	0.000949	0.001527	0.001777	0.001615	0.001212	0.000782	0.000447
[5-5.5]	5.25					0.000131	0.000404	0.000754	0.000966	0.000928	0.000714	0.00046	0.000258
[5.5-6]	5.75						0.000136	0.0003	0.00043	0.000442	0.000351	0.000227	0.000125
[6-6.5]	6.25								0.000155	0.000172	0.000142		
[6.5-7]	6.75												
[7-7.5]	7.25												
[7.5-8]	7.75												
[8-8.5]	8.25												
[8.5-9]	8.75												

Figure C.6: Example of scatter diagram of joint probability distribution $[U_w = 14\,\mathrm{m/s}]$.

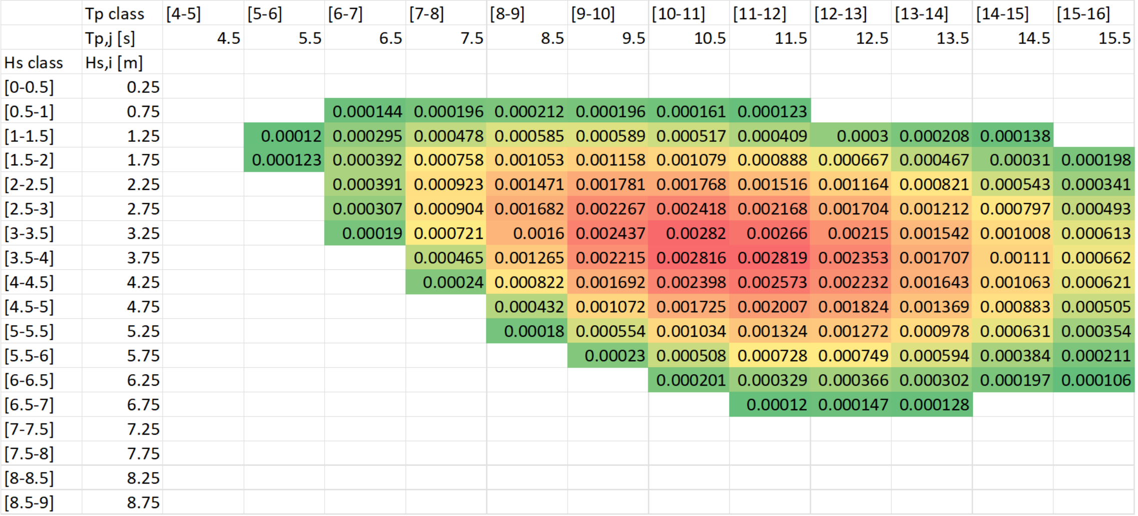

	Tp class	[4-5]	[5-6]	[6-7]	[7-8]	[8-9]	[9-10]	[10-11]	[11-12]	[12-13]	[13-14]	[14-15]	[15-16]
	Tp,j [s]	4.5	5.5	6.5	7.5	8.5	9.5	10.5	11.5	12.5	13.5	14.5	15.5
Hs class	Hs,i [m]												
[0-0.5]	0.25												
[0.5-1]	0.75			0.000144	0.000196	0.000212	0.000196	0.000161	0.000123				
[1-1.5]	1.25		0.00012	0.000295	0.000478	0.000585	0.000589	0.000517	0.000409	0.0003	0.000208	0.000138	
[1.5-2]	1.75		0.000123	0.000392	0.000758	0.001053	0.001158	0.001079	0.000888	0.000667	0.000467	0.00031	0.000198
[2-2.5]	2.25			0.000391	0.000923	0.001471	0.001781	0.001768	0.001516	0.001164	0.000821	0.000543	0.000341
[2.5-3]	2.75			0.000307	0.000904	0.001682	0.002267	0.002418	0.002168	0.001704	0.001212	0.000797	0.000493
[3-3.5]	3.25			0.00019	0.000721	0.0016	0.002437	0.00282	0.00266	0.00215	0.001542	0.001008	0.000613
[3.5-4]	3.75				0.000465	0.001265	0.002215	0.002816	0.002819	0.002353	0.001707	0.00111	0.000662
[4-4.5]	4.25				0.00024	0.000822	0.001692	0.002398	0.002573	0.002232	0.001643	0.001063	0.000621
[4.5-5]	4.75					0.000432	0.001072	0.001725	0.002007	0.001824	0.001369	0.000883	0.000505
[5-5.5]	5.25					0.00018	0.000554	0.001034	0.001324	0.001272	0.000978	0.000631	0.000354
[5.5-6]	5.75						0.00023	0.000508	0.000728	0.000749	0.000594	0.000384	0.000211
[6-6.5]	6.25							0.000201	0.000329	0.000366	0.000302	0.000197	0.000106
[6.5-7]	6.75								0.00012	0.000147	0.000128		
[7-7.5]	7.25												
[7.5-8]	7.75												
[8-8.5]	8.25												
[8.5-9]	8.75												

Figure C.7: Example of scatter diagram of joint probability distribution $[U_w = 16\,\mathrm{m/s}]$.

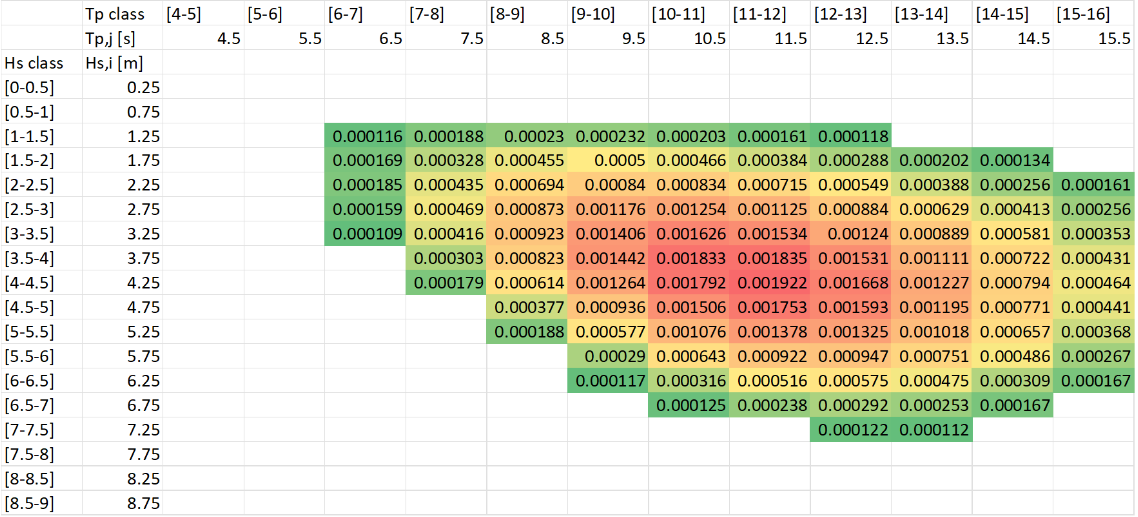

	Tp class	[4-5]	[5-6]	[6-7]	[7-8]	[8-9]	[9-10]	[10-11]	[11-12]	[12-13]	[13-14]	[14-15]	[15-16]
	Tp,j [s]	4.5	5.5	6.5	7.5	8.5	9.5	10.5	11.5	12.5	13.5	14.5	15.5
Hs class	Hs,i [m]												
[0-0.5]	0.25												
[0.5-1]	0.75												
[1-1.5]	1.25			0.000116	0.000188	0.00023	0.000232	0.000203	0.000161	0.000118			
[1.5-2]	1.75			0.000169	0.000328	0.000455	0.0005	0.000466	0.000384	0.000288	0.000202	0.000134	
[2-2.5]	2.25			0.000185	0.000435	0.000694	0.00084	0.000834	0.000715	0.000549	0.000388	0.000256	0.000161
[2.5-3]	2.75			0.000159	0.000469	0.000873	0.001176	0.001254	0.001125	0.000884	0.000629	0.000413	0.000256
[3-3.5]	3.25			0.000109	0.000416	0.000923	0.001406	0.001626	0.001534	0.00124	0.000889	0.000581	0.000353
[3.5-4]	3.75				0.000303	0.000823	0.001442	0.001833	0.001835	0.001531	0.001111	0.000722	0.000431
[4-4.5]	4.25				0.000179	0.000614	0.001264	0.001792	0.001922	0.001668	0.001227	0.000794	0.000464
[4.5-5]	4.75					0.000377	0.000936	0.001506	0.001753	0.001593	0.001195	0.000771	0.000441
[5-5.5]	5.25					0.000188	0.000577	0.001076	0.001378	0.001325	0.001018	0.000657	0.000368
[5.5-6]	5.75						0.00029	0.000643	0.000922	0.000947	0.000751	0.000486	0.000267
[6-6.5]	6.25						0.000117	0.000316	0.000516	0.000575	0.000475	0.000309	0.000167
[6.5-7]	6.75							0.000125	0.000238	0.000292	0.000253	0.000167	
[7-7.5]	7.25									0.000122	0.000112		
[7.5-8]	7.75												
[8-8.5]	8.25												
[8.5-9]	8.75												

Figure C.8: Example of scatter diagram of joint probability distribution [$U_w = 18\,\mathrm{m/s}$].

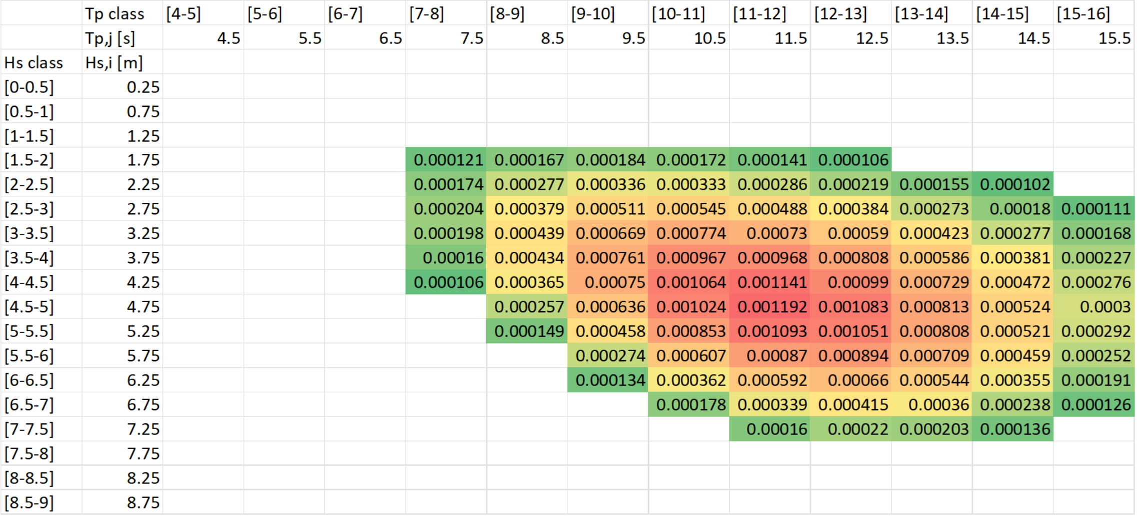

	Tp class	[4-5]	[5-6]	[6-7]	[7-8]	[8-9]	[9-10]	[10-11]	[11-12]	[12-13]	[13-14]	[14-15]	[15-16]
	Tp,j [s]	4.5	5.5	6.5	7.5	8.5	9.5	10.5	11.5	12.5	13.5	14.5	15.5
Hs class	Hs,i [m]												
[0-0.5]	0.25												
[0.5-1]	0.75												
[1-1.5]	1.25												
[1.5-2]	1.75				0.000121	0.000167	0.000184	0.000172	0.000141	0.000106			
[2-2.5]	2.25				0.000174	0.000277	0.000336	0.000333	0.000286	0.000219	0.000155	0.000102	
[2.5-3]	2.75				0.000204	0.000379	0.000511	0.000545	0.000488	0.000384	0.000273	0.00018	0.000111
[3-3.5]	3.25				0.000198	0.000439	0.000669	0.000774	0.00073	0.00059	0.000423	0.000277	0.000168
[3.5-4]	3.75				0.00016	0.000434	0.000761	0.000967	0.000968	0.000808	0.000586	0.000381	0.000227
[4-4.5]	4.25				0.000106	0.000365	0.00075	0.001064	0.001141	0.00099	0.000729	0.000472	0.000276
[4.5-5]	4.75					0.000257	0.000636	0.001024	0.001192	0.001083	0.000813	0.000524	0.0003
[5-5.5]	5.25					0.000149	0.000458	0.000853	0.001093	0.001051	0.000808	0.000521	0.000292
[5.5-6]	5.75						0.000274	0.000607	0.00087	0.000894	0.000709	0.000459	0.000252
[6-6.5]	6.25						0.000134	0.000362	0.000592	0.00066	0.000544	0.000355	0.000191
[6.5-7]	6.75							0.000178	0.000339	0.000415	0.00036	0.000238	0.000126
[7-7.5]	7.25								0.00016	0.00022	0.000203	0.000136	
[7.5-8]	7.75												
[8-8.5]	8.25												
[8.5-9]	8.75												

Figure C.9: Example of scatter diagram of joint probability distribution [$U_w = 20\,\mathrm{m/s}$].

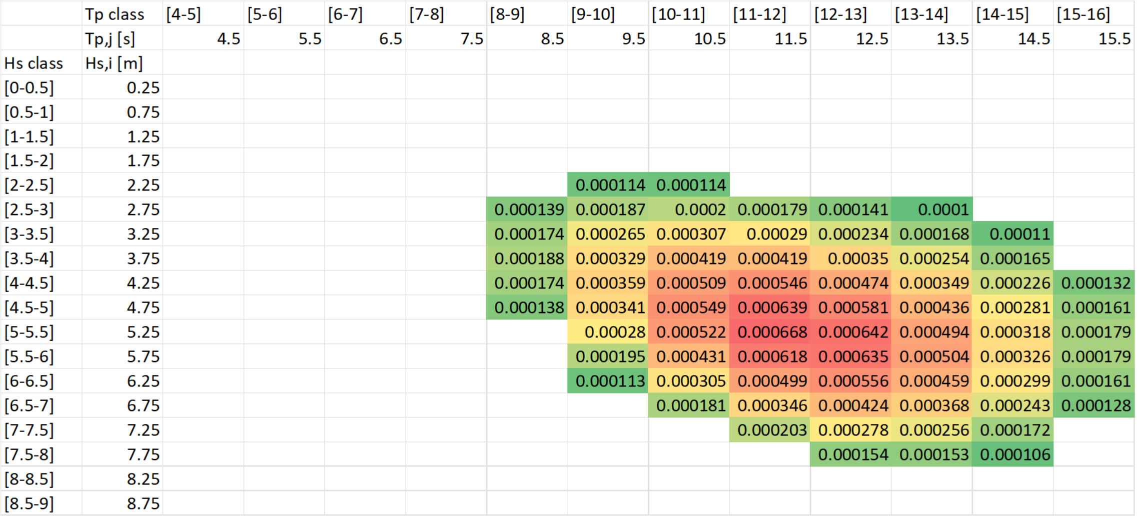

	Tp class	[4-5]	[5-6]	[6-7]	[7-8]	[8-9]	[9-10]	[10-11]	[11-12]	[12-13]	[13-14]	[14-15]	[15-16]
	Tp,j [s]	4.5	5.5	6.5	7.5	8.5	9.5	10.5	11.5	12.5	13.5	14.5	15.5
Hs class	Hs,i [m]												
[0-0.5]	0.25												
[0.5-1]	0.75												
[1-1.5]	1.25												
[1.5-2]	1.75												
[2-2.5]	2.25						0.000114	0.000114					
[2.5-3]	2.75					0.000139	0.000187	0.0002	0.000179	0.000141	0.0001		
[3-3.5]	3.25					0.000174	0.000265	0.000307	0.00029	0.000234	0.000168	0.00011	
[3.5-4]	3.75					0.000188	0.000329	0.000419	0.000419	0.00035	0.000254	0.000165	
[4-4.5]	4.25					0.000174	0.000359	0.000509	0.000546	0.000474	0.000349	0.000226	0.000132
[4.5-5]	4.75					0.000138	0.000341	0.000549	0.000639	0.000581	0.000436	0.000281	0.000161
[5-5.5]	5.25						0.00028	0.000522	0.000668	0.000642	0.000494	0.000318	0.000179
[5.5-6]	5.75						0.000195	0.000431	0.000618	0.000635	0.000504	0.000326	0.000179
[6-6.5]	6.25						0.000113	0.000305	0.000499	0.000556	0.000459	0.000299	0.000161
[6.5-7]	6.75							0.000181	0.000346	0.000424	0.000368	0.000243	0.000128
[7-7.5]	7.25								0.000203	0.000278	0.000256	0.000172	
[7.5-8]	7.75									0.000154	0.000153	0.000106	
[8-8.5]	8.25												
[8.5-9]	8.75												

Figure C.10: Example of scatter diagram of joint probability distribution $[U_w = 22\,\mathrm{m/s}]$.

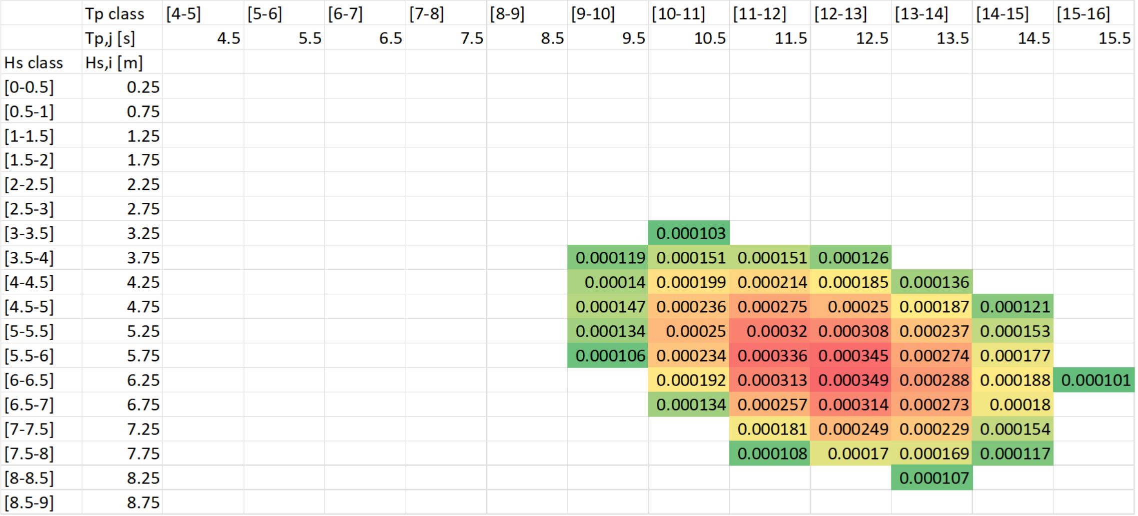

	Tp class	[4-5]	[5-6]	[6-7]	[7-8]	[8-9]	[9-10]	[10-11]	[11-12]	[12-13]	[13-14]	[14-15]	[15-16]
	Tp,j [s]	4.5	5.5	6.5	7.5	8.5	9.5	10.5	11.5	12.5	13.5	14.5	15.5
Hs class	Hs,i [m]												
[0-0.5]	0.25												
[0.5-1]	0.75												
[1-1.5]	1.25												
[1.5-2]	1.75												
[2-2.5]	2.25												
[2.5-3]	2.75												
[3-3.5]	3.25							0.000103					
[3.5-4]	3.75						0.000119	0.000151	0.000151	0.000126			
[4-4.5]	4.25						0.00014	0.000199	0.000214	0.000185	0.000136		
[4.5-5]	4.75						0.000147	0.000236	0.000275	0.00025	0.000187	0.000121	
[5-5.5]	5.25						0.000134	0.00025	0.00032	0.000308	0.000237	0.000153	
[5.5-6]	5.75						0.000106	0.000234	0.000336	0.000345	0.000274	0.000177	
[6-6.5]	6.25							0.000192	0.000313	0.000349	0.000288	0.000188	0.000101
[6.5-7]	6.75							0.000134	0.000257	0.000314	0.000273	0.00018	
[7-7.5]	7.25								0.000181	0.000249	0.000229	0.000154	
[7.5-8]	7.75								0.000108	0.00017	0.000169	0.000117	
[8-8.5]	8.25										0.000107		
[8.5-9]	8.75												

Figure C.11: Example of scatter diagram of joint probability distribution $[U_w = 24\,\mathrm{m/s}]$.

Appendix D

Alternative Methods for Multi-body Modeling

In Appendix D, two simplified methods are briefly discussed. The two methods are not applied due to the inaccuracy in describing the motions. These two methods are still introduced and discussed here in details, since there is the space for improvement.

D.1 Discussion of Modeling Method S1

RIFLEX code is universally utilized and verified in the studies of mooring system, it is also assigned with the functionality of inputting hydrodynamic force which is based on potential flow theory. The method of inputting the hydrodynamic coefficients to RIFLEX beam is utilized by Svendsen [7] who applied this method to study the elasticity of a TLP-type platform. Hegseth [8] used this method to study the response of a semi-submersible FOWT. Brevik [9] used this method to study the elasticity of two spar-type floater. In their works, the added mass, damping coefficients and transfer function of excitation integrated matches to those output directly from Wamit to a great extent, with the case of semi-submersible as an exception. This method is a simplified method which neglects the contribution of the moment caused by angular acceleration or angular velocity. It assumes that the moment caused by translational force matters much more than the moment caused by local rotations. Under each frequency, the added mass and damping are 6x6 matrix. The off-diagonal terms in the A and B matrix can be calculated using the formula in

Equation D.1.1.

$$\begin{aligned} A_{15} &= \sum_{n1}^{N_{sec}}(A_{11}^{(n)}z^{(n)} - A_{13}^{(n)}x^{(n)}),\ B_{15} = \sum_{n=1}^{N_{sec}}(B_{11}^{(n)}z^{(n)} - B_{13}^{(n)}x^{(n)}) \\ A_{24} &= \sum_{n=1}^{N_{sec}}(A_{22}^{(n)}z^{(n)} - A_{13}^{(n)}x^{(n)}),\ B_{24} = \sum_{n=1}^{N_{sec}}(B_{22}^{(n)}z^{(n)} - B_{13}^{(n)}x^{(n)}) \\ A_{26} &= \sum_{n=1}^{N_{sec}}(A_{11}^{(n)}z^{(n)} - A_{13}^{(n)}x^{(n)}),\ B_{26} = \sum_{n=1}^{N_{sec}}(B_{11}^{(n)}z^{(n)} - B_{13}^{(n)}x^{(n)}) \end{aligned} \tag{D.1.1}$$

The diagonal terms of rotational motions in the A and B matrix can be written as

$$\begin{aligned} A_{55} &= \sum_{n=1}^{N_{sec}}[A_{11}^{(n)}(z^{(n)})^2 - 2\cdot A_{13}^{(n)}z^{(n)}x^{(n)} + A_{33}^{(n)}(x^{(n)})^2] \\ B_{55} &= \sum_{n=1}^{N_{sec}}[B_{11}^{(n)}(z^{(n)})^2 - 2\cdot B_{13}^{(n)}z^{(n)}x^{(n)} + B_{33}^{(n)}(x^{(n)})^2] \\ A_{44} &= \sum_{n=1}^{N_{sec}}[A_{22}^{(n)}(z^{(n)})^2 - 2\cdot A_{32}^{(n)}y^{(n)}z^{(n)} + A_{33}^{(n)}(y^{(n)})^2] \\ B_{44} &= \sum_{n=1}^{N_{sec}}[B_{22}^{(n)}(z^{(n)})^2 - 2\cdot B_{32}^{(n)}y^{(n)}z^{(n)} + B_{33}^{(n)}(y^{(n)})^2] \\ A_{66} &= \sum_{n=1}^{N_{sec}}[A_{22}^{(n)}(x^{(n)})^2 - 2\cdot A_{12}^{(n)}y^{(n)}x^{(n)} + A_{11}^{(n)}(y^{(n)})^2] \\ B_{66} &= \sum_{n=1}^{N_{sec}}[B_{22}^{(n)}(x^{(n)})^2 - 2\cdot B_{12}^{(n)}y^{(n)}x^{(n)} + B_{11}^{(n)}(y^{(n)})^2] \end{aligned} \tag{D.1.2}$$

In the work of Brevik, Hegseth and Svendsen [7, 8, 9], the effect of increasing number of cuts can improve the accuracy of overall hydrodynamic coefficients input to RIFLEX. In the work of this thesis, the columns and pontoons of the semi-submersible platform are divided in five division modes as listed in Table D.1. The *dm* is the abbreviation of division mode.

Division Mode	dm = 1	dm = 2	dm = 3	dm = 4	dm = 5
Column x4	16	12	8	4	2
Pontoon x3	16	12	8	4	2
Total	108	84	56	28	14

Table D.1: Number of sections in different division mode.

As mentioned, the diffraction forces and radiation coefficients of each section are inserted to the corresponding RIFLEX beam element. The RIFLEX beam model in different division mode listed in Table D.1 is shown in Figure D.1. The rotational added mass and damping coefficient should be checked. When it comes to the off-diagonal terms in the A and B matrix, three off-diagonal terms are selected to have comparisons. These terms are calculated in SIMA through calculating the moment to the global original point caused by the translational forces.

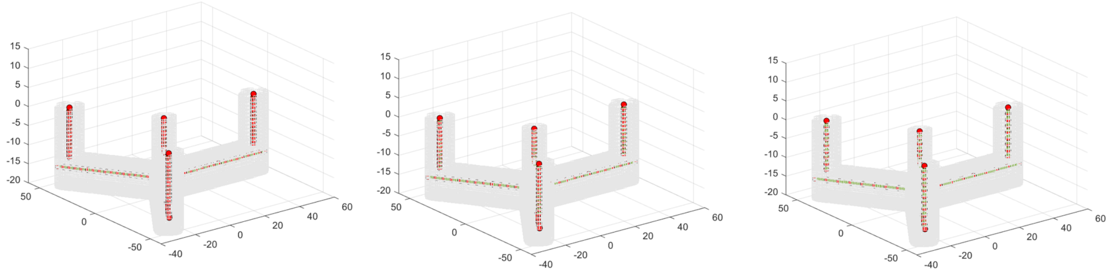

(a) dm 1, 108 sections **(b)** dm 2, 84 sections **(c)** dm 3, 56 sections

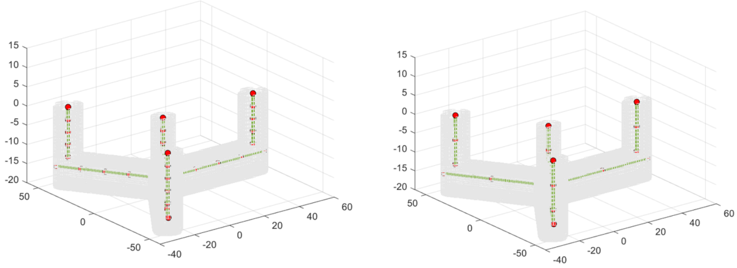

(d) dm 4, 28 sections **(e)** dm 5, 14 sections

Figure D.1: RIFLEX beam elements of the elastic floater.

The translational total added mass and damping coefficients should present perfect matches, since the local translational terms can be transferred to the global coordinate directly. This is shown in Figure D.2.

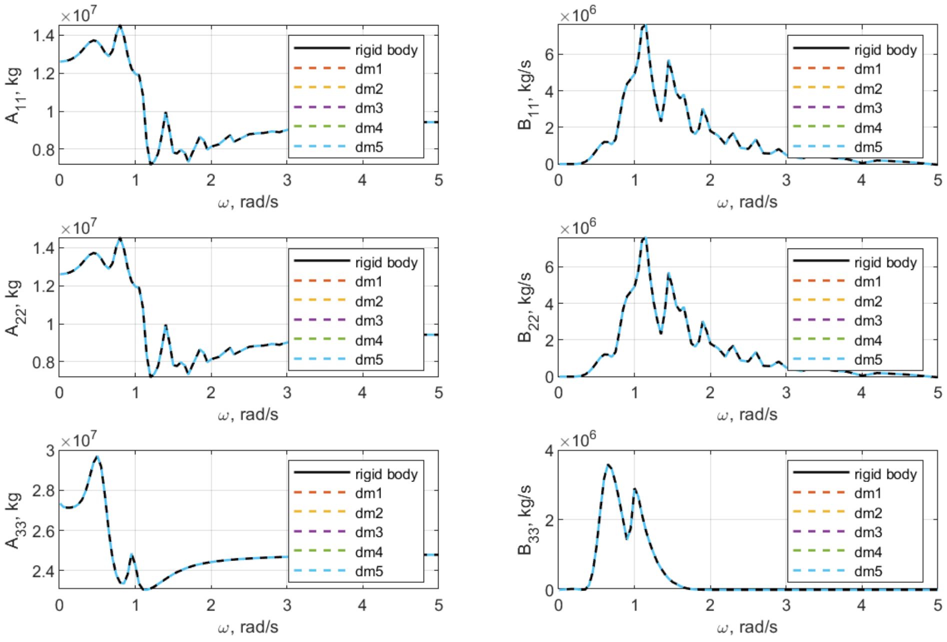

Figure D.2: Translational added mass and damping under different division modes.

The magnitude of added mass and damping coefficients in the surge-pitch coupling and sway-roll coupling motions are compared in Figure D.3. There are large variance at lower frequencies. Increasing the length of subsections can improve the accuracy to some extend, but after the structure is divided into 56 sub-bodies, there is no more further improvement. It is the same with the diagonal rotational added mass and damping. This also indicates that the moment introduced by local rotation is non-negligible for this semi-submersible floater model.

The result in Figure D.3 shows that the multi-body model in SIMA would over-estimate the added mass in roll and surge motions, and this is unavoidable even if the division of the model is finer. This method is not suitable to be used. The added mass coefficients influence the natural period of of platform motion, while the damping influences the amplitude of motions. This input cannot guarantee an acceptable similarity between models.

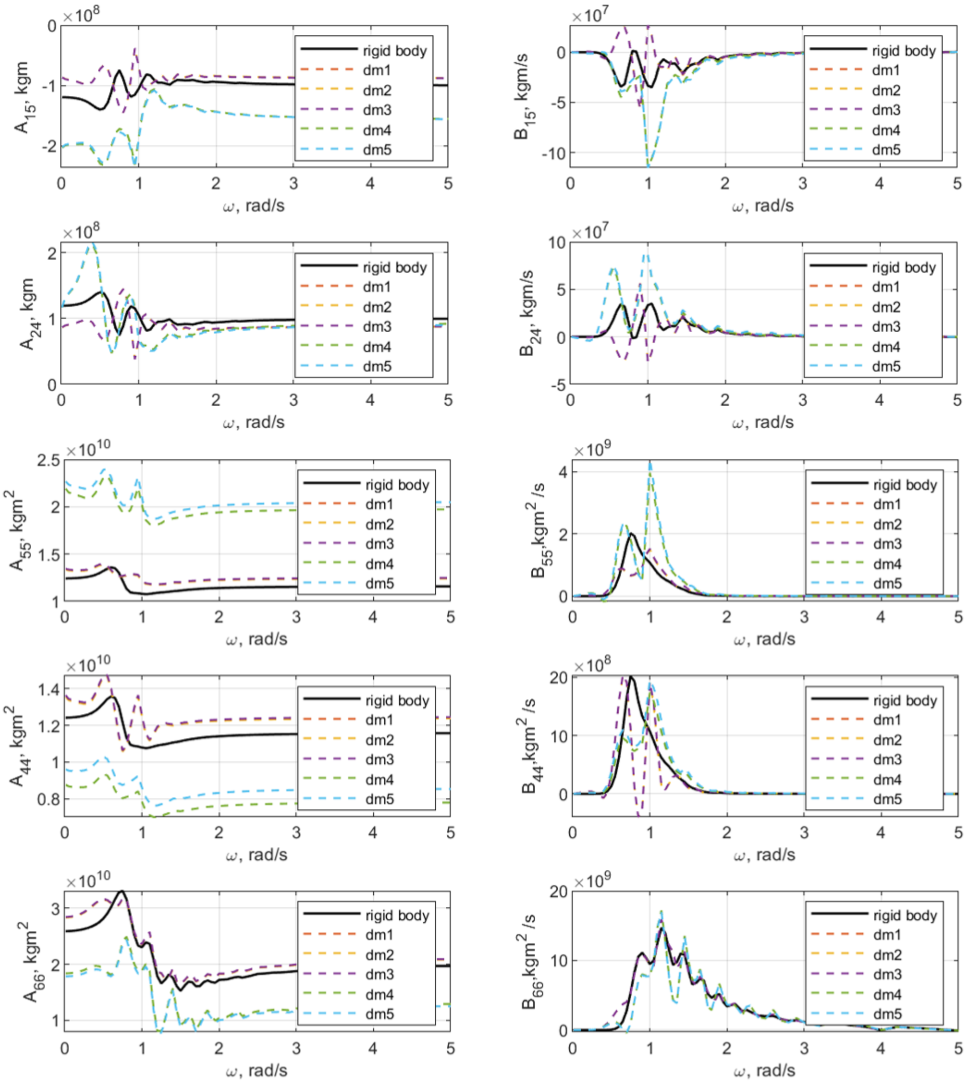

Figure D.3: Diagonal rotational added mass and damping under different division modes.

D.2 Discussion of Modeling Method S2

Due to that the numerical model built in RIFLEX with integrated WAMIT result input to each beam element cannot map the overall hydrodynamic coefficients into sub-bodies perfectly, SIMO bodies are employed to fill in the gap. The SIMO body is added to nodes on RIFLEX beams in order to render kinetic characteristics reasonably. This method enables the insertion of added mass and damping coefficients as well as transfer functions of excitation force in 6 DOF. The sectional added mass and damping matrix can be sum up to be compared with the total added mass and damping produced in WAMIT. The Figure D.4, Figure D.5 and Figure D.6 shows that the added mass and damping coefficients distributed to the multi-body model match the input to rigid-body model. This method can rationally depict the motion of the platform.

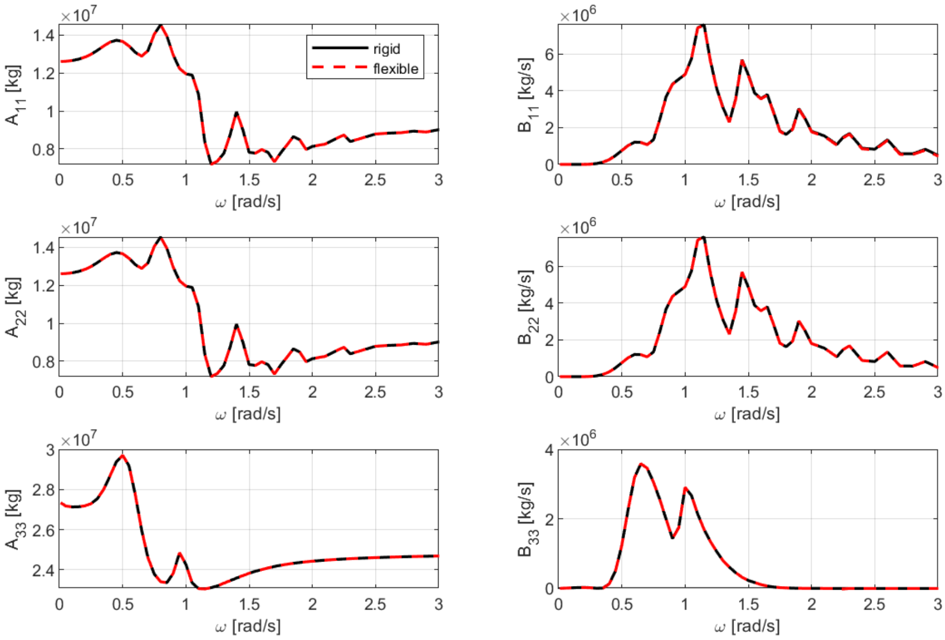

Figure D.4: Comparison of translational added mass and damping components (the red curves represent the summation of sectional added mass and damping, while the black curves represents the output of total added mass and damping from Wamit).

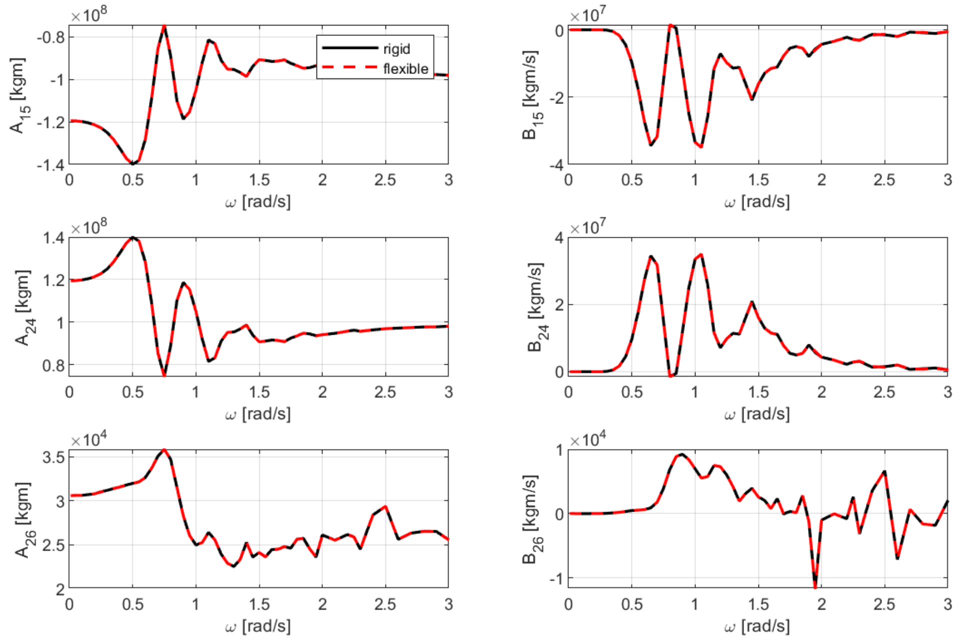

Figure D.5: Comparison of of selected off-diagonal added mass and damping coefficients (the red curves represent the summation of sectional added mass and damping, while the black curves represents the output of total added mass and damping from Wamit).

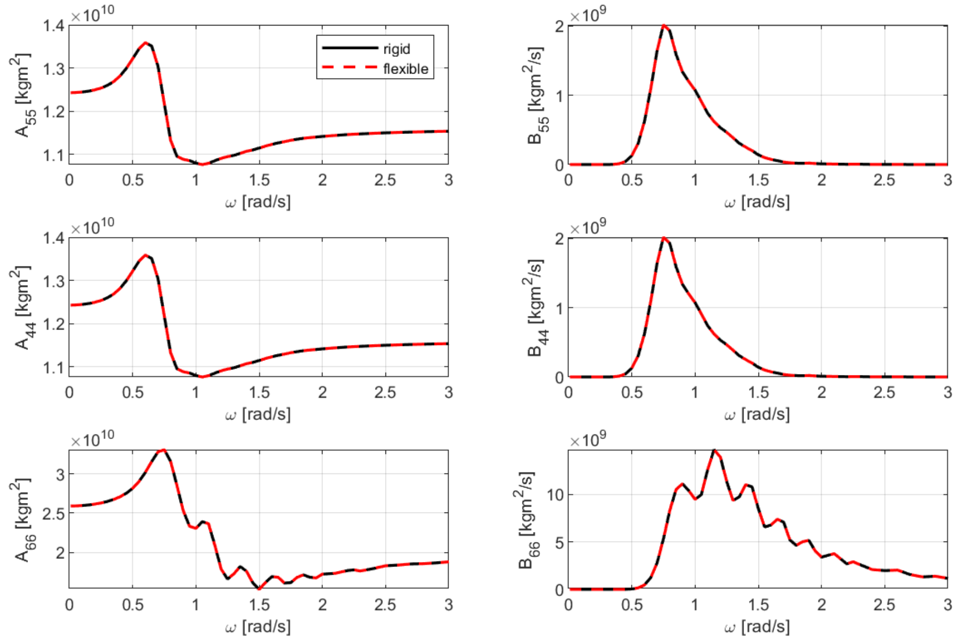

Figure D.6: Comparison of diagonal added mass and damping components (the red curves represent the summation of sectional added mass and damping, while the black curves represents the output of total added mass and damping from Wamit).

The module and phase angle of transfer function of excitation with wave from 0 degree direction is plotted in Figure D.7. The transfer function of excitation force matches each other completely, while the phase angles have minor bias, which roots in the data accuracy when the information travels through different computer program.

The added mass, damping coefficients and transfer functions are calculated through integrating the distributed dynamic pressure of panels over sections. These are input as kinetic properties of SIMO bodies. Other kinetic properties principally includes restoring stiffness, inertia and buoyancy are described by RIFLEX. The mass and inertia are calculated by RIFLEX when the cross-sectional mass is input as properties of beams. The buoyancy is computed based on the volume defined by the cross-sectional area. And the restoring stiffness is calculated in RIFLEX based on the moment caused by buoyancy and gravity. This means that the method used in this subsection has strict control over added mass, damping coefficients and transfer functions, while the other terms in the equilibrium depends on the RIFLEX program. The design of this approach aims at higher accuracy of motion description and less additional complexity in computation. The visualization of the floater model in SIMO/RIFLEX is shown in Figure D.8.

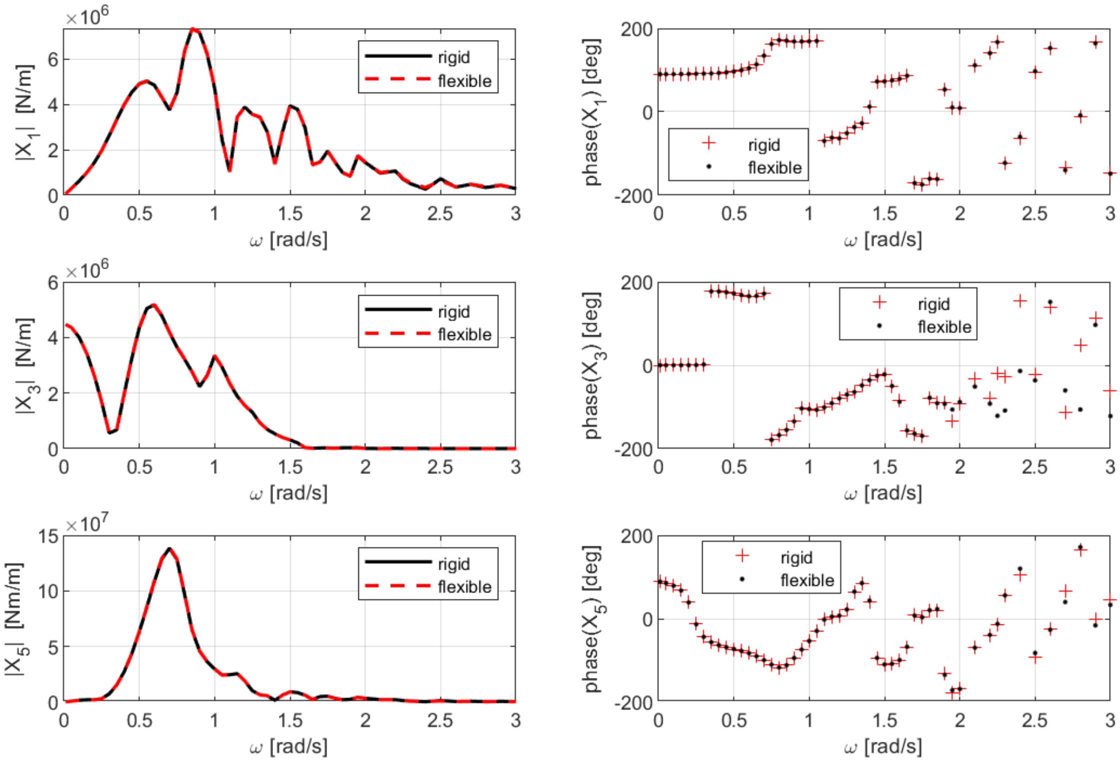

Figure D.7: Comparison of transfer functions of 0-degree wave (the red curves represent the module of summation of sectional excitation transfer function, while the black curves represents the module of excitation transfer function from Wamit; the red scatters represent the phase of summation of sectional excitation transfer function, while the black scatters represent the phase of excitation transfer function from Wamit).

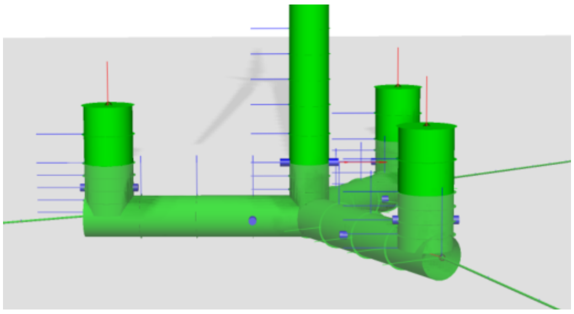

Figure D.8: Elastic floater modeled with beam elements, inputted with A, B & F_{exc} from Wamit).

To further examine the kinetic characteristics of the flexible multi-body model, of which the inertia and restoring stiffness is calculated in RIFLEX code, 6-DOF decay test is proceeded and plotted in Figure D.9. The decay test result indicates the drawback of this method that the natural frequency of pitch and roll is lengthened, as can be seen from the mismatch of peaks of oscillation. This mismatch results from the bias in both inertia and restoring stiffness. In the method S2, the rotational inertia of the platform is estimated by the mass of cylinder-type beams, while the hydro-stiffness is calculated based on the mass of displaced water of cylinder-type beams, which equals to the buoyancy. Under the condition that the cross-sectional area and mass are given correctly, there is still slight bias due to the simplicity of calculating inertia and restoring force. This model cannot be applied directly, since the change of pitch and roll natural frequency may significantly influence the dynamic response. Kinetic consistency is one of the important preconditions that the result calculated is convincing, based on the confidence in the rigid-floater model. The exploration with method S2 gives the insight that the focus should be the inertia and restoring stiffness, in order to build a more successful multi-body model. This insight leads to the updated method C1 in the main text.

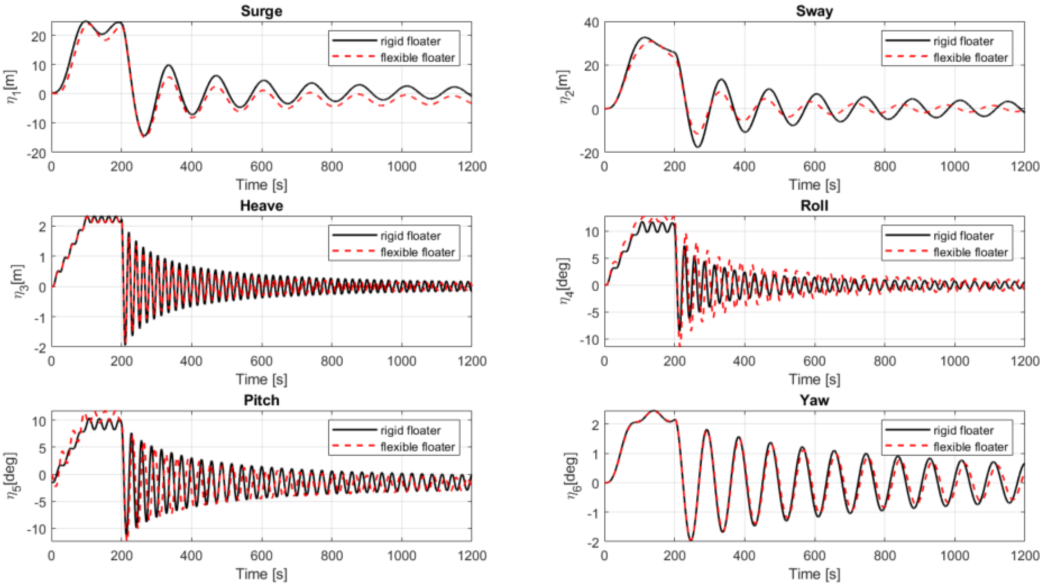

Figure D.9: Decay test of flexible multi-body model compared with rigid-body model.